

**Magneto-Optical Trapping
of
Radioactive Atoms**

**Inaugural Dissertation
zur
Erlangung des Doktorgrades
der Naturwissenschaften
der Justus-Liebig Universität Giessen
(Fachbereich Physik)**

vorgelegt von

Ralf Guckert

aus

Butzbach-Ostheim

Giessen, Hessen

April 1998

© 1998 by Ralf Guckert
All rights reserved.

Dekan: Prof. Dr. C.-D. Kohl

1. Berichterstatter: Prof. Dr. H. Wollnik

2. Berichterstatter: Prof. Dr. C.-D. Kohl

Tag der mündlichen Prüfung: 8. Mai 1998

Zusammenfassung

Vier Jahrzehnte sind vergangen seit der Veröffentlichung der ersten Thesen von Lee und Yang [1], die die Möglichkeit der Paritätsverletzung in der Schwachen Wechselwirkung vorschlugen. Der experimentelle Nachweis durch Wu *et al.* erfolgte innerhalb weniger Jahre in einem $\bar{\nu}$ -Zerfall Experiment [2] welches die Winkelverteilung der Elektronen untersuchte, die von ausgerichteten ^{60}Co -Kernen emittiert wurden. Das Ergebnis zeigte, daß die Elektronen nicht wie erwartet isotrop emittiert werden, sondern daß die Zählrate der Elektronen im Detektor von der Orientierung des Kernspins des emittierenden Co-Atoms abhängt. Mit diesem Experiment war zum erstenmal eine physikalische Erscheinung gefunden die nicht spiegelinvariant ist.

Die beobachtete Winkelverteilung der Elektronen folgt der Form $1 + A \cos \mu$ und die gemessene Genauigkeit des Parameter “A” in Wu’s Experiment liegt bei $\gg 10\%$. Eine erneute Messung mit einer verbesserten Quellengeometrie erlaubte die Bestimmung von “A” mit einer Genauigkeit von $\gg 2\%$ [3]. Das *Standart Model der Elektroschwachen Wechselwirkung* beschreibt die Winkelverteilung der emittierten Elektronen im $\bar{\nu}$ -Zerfall und die Aufgabe moderner Experimente ist die präzise Bestimmung der unterschiedlichen Parameter (in unserem Falle die des Parameters A) mit dem Ziel die Helizität der Wechselwirkung zwischen Quarks und Leptonen zu bestimmen.

Die Grenzen der Genauigkeit mit der “A” in modernen $\bar{\nu}$ -Zerfall Experimenten gemessen werden kann liegen zur Zeit bei $\gg 1\%$ [4]. Dies ist begründet in

der unzureichenden Präzision, mit der der Kernspin des Präparates ausgerichtet und bestimmt werden kann. Desweiteren führen energieabhängige Korrekturterme zu Verfälschungen, die die Vorhersage von “A” erschweren.

Mit der Erfindung der Atomfallen erscheint es möglich ein Präparat zu formen, welches in beiden Bereichen wesentliche Verbesserungen verspricht. Der Kernspin der Atome in einer Atomfalle kann zu nahezu 100% (abhängig von der gewählten Geometrie der Falle) ausgerichtet und Mittels optischer Methoden mit extremer Genauigkeit bestimmt werden ($<0.1\%$). Desweiteren erlauben polarisierte Atome in einer geeigneten Atomfalle die Bestimmung der energieabhängige Korrekturterme und damit die Bestimmung des Parameters “A” mit einer Genauigkeit von $\gg 0.1\%$. Die Atome in einer solchen Falle repräsentieren ein nahezu ideales “Labor” für die präzise Messung der paritätsverletzenden schwachen Wechselwirkung, auf Grund der im wesentlichen masselosen, punktförmigen und polarisierten Struktur der gespeicherten Atome.

Allerdings erfordert ein solches β^- -Zerfall Experiment die Speicherung einer hinreichend grossen Anzahl radioaktiver Atome in der Atomfalle. 1994 erfolgte die erstmalige Speicherung von radioaktiven Atomen in einer optischen Atomfalle. Die Forschergruppe aus Berkeley konnte 4000 ^{21}Na Atome erfolgreich in die Atomfalle laden und für 5 Sekunden speichern [5]. Kürzlich veröffentlichte die Arbeitsgruppe eine verbesserte Version die nun $\gg 40000$ Atome speichert [6]. Stimuliert durch diesen Erfolg arbeiten heute sechs Gruppen weltweit an dieser Aufgabe.

Die hier vorliegende Arbeit beschreibt die Produktion eines Ionenstrahls hoher Intensität ($\gg 10^8$ ^{82}Rb Ionen pro Sekunde), den Aufbau eines Massenseparators, die Kopplung einer optischen Atomfalle mit dem Massenseparator und die erfolgreiche Speicherung radioaktiver ^{82}Rb Atome in der Atomfalle. Die prinzipiellen Schwierigkeiten, verglichen mit Atomfallen für nichtradioaktive Präparate, konnten in unserem Labor überwunden werden [7, 8]. Erstmals wurde eine große Anzahl (6 Millionen) radioaktive ^{82}Rb Atome in einer optischen Atomfalle über einen Zeitraum von 90 Sekunden gespeichert. Dies entspricht einer mehr als 100 fachen Verbesserung verglichen mit den besten veröffentlichten Ergebnissen aus Berkeley und erlaubt somit die Durchführung eines präzisen β^- -Zerfall Experimentes in einer Atomfalle.

Abstract

Four decades have past since the first suggestion by Lee and Yang that parity could be violated in weak interactions [1], and the subsequent discovery by Wu *et al.* of parity violation in the β^- -decay of polarized ^{60}Co [2]. More recent measurements have led to a second generation result with about 2% precision [3] in the parity-violating electron-spin asymmetry (A). Modern experiments to study fundamental symmetries in nuclear β^- -decay of the free neutron have reached a sensitivity of $\gg 1\%$ in measuring the electron-spin correlation [4], although the experiments disagree beyond the quoted level of accuracy.

With the appearance of optical traps for neutral atoms in 1987 [9], it is now possible to envision a new generation of nuclear β^- -decay experiments that could reach sensitivities of $\gg 0.1\%$ on measuring A by taking advantage of the desirable properties of the atoms in such traps.

This thesis demonstrates the successful trapping of $\gg 6 \times 10^6$ radioactive ^{82}Rb atoms for the purpose of a nuclear β^- -decay measurement. The achievement of trapping a large number of atoms in such a trap opens the door to a new generation of very precise nuclear β^- -decay measurements that exploit the essentially massless, point-like, and highly polarized character of such a confined cloud of atoms.

A description of the production of an intense beam of radioactive ^{82}Rb ions ($\gg 10^8$ ions/sec), the development of a high-transmission mass separator, the efficient coupling of an optical trap to a mass separator, and the successful trapping of $\gg 6 \times 10^6$ ^{82}Rb atoms in a Magneto-Optical Trap (MOT) is presented. The trapping of such a large number of radioactive atoms represents a two order of magnitude improvement over previous radioactive atom trapping work, and enables us to pursue the development of a next generation nuclear β^- -decay measurement in an atomic system.

Acknowledgments

Thanks are due to a large number of people for their continuing support throughout the years. In particular, I am indebted to both of my supervisors, Prof. Dr. Hermann Wollnik of the *II. Physikalisches Institut der Universität Giessen*, and Dr. David J. Vieira of the *Los Alamos National Laboratory*, for teaching me the art of experimental physics and their continuous personal support and understanding.

Also, I wish to thank Dr. Andrew Hime for many fruitful discussions, his personal involvement, and encouragement that more than once was desperately needed. I would like to thank Dr. Xinxin Zhao, Dr. Dale Tupa and Dr. Vern Sandberg, as well as my fellow graduate student Scott G. Crane, for frequent discussions and help that has led to this thesis.

In general, the support personnel involved in this work, especially Wayne Taylor of CST-11, the members of the CST shop crew, as well as McIlwaine III Archer of the LANL Glass Shop, deserve credit for their continuous effort to fulfill my requests with outstanding craftsmanship.

Last, but certainly not least, I wish to thank my wife Sylvia, and my parents Renate and Kurt for their love and undying support.

Contents

List of Figures	xii
List of Tables	xiv
1 Introduction	1
1.1 The History of Trapping Radioactive Atoms	1
1.2 Preview of this Thesis	3
1.2.1 Introduction to Laser Cooling	3
1.2.2 Doppler Cooling	4
1.2.3 Trapping of Radioactive Atoms	6
2 Cooling and Trapping of Neutral Atoms	8
2.1 Light-Atom Interaction	10
2.1.1 Basic Considerations	10
2.1.2 The Optical Bloch Equations	11
2.1.3 Light Forces	13
2.1.4 Deceleration of an Atomic Beam	15
2.1.5 Deflection and Collimation of an Atomic Beam	17
2.2 Optical Traps for Neutral Atoms	19
2.2.1 Dipole Force Traps	20
2.2.2 Radiation Pressure Traps	21
2.3 Applications of Laser Cooling and Trapping	24
2.3.1 Bose-Einstein Condensation	24
2.3.2 Atomic Parity Non-Conservation	26
2.3.3 Nuclear β^- -decay Measurements	28
3 The Making of a Radioactive Ion Beam	33
3.1 The Sample Preparation	34
3.2 Thermal Ion Sources - Theory of Operation	36
3.2.1 The Surface Ionization Source	38
3.2.2 The Hot Cavity Ion Source	40
3.3 The Ion Source - Experiment	43

3.3.1	Ion Source Diagnostics	51
3.4	Mass Separation of Isotopes	52
3.4.1	The Mass Separator	53
3.4.2	Ion Beam Diagnostics	58
3.4.3	Typical Performance of the Ion Source and the Mass Separator . . .	59
3.5	Foil Studies	62
4	A Laser Trap for Radioactive Atoms	69
4.1	The MOT	70
4.2	Trapping Efficiency Considerations	71
4.2.1	A MOT for the Study of Trapping Efficiency	74
4.3	The Coupling of a MOT and a Mass Separator	84
4.4	The Laser Setup	85
4.5	Light Detection Devices	91
4.5.1	The CCD-Camera	91
4.5.2	Calibrated Photodiode	93
4.5.3	Photomultiplier Tube	93
4.6	Detection Schemes	94
4.6.1	Phase-Sensitive Detection	96
4.6.2	Photon Counting	97
5	Trapped Radioactive Rubidium Atoms	99
5.1	Laser Setup for ^{82}Rb	100
5.2	Modes for Trapping from the Mass Separator	100
5.2.1	Trapped Radioactive ^{82}Rb Atoms	102
5.2.2	Efficiency Considerations	105
5.3	Measurements on the Trapped Atoms	108
6	High-Precision Measurements using Trapped Atoms	112
6.1	The Layout of the π -Asymmetry Experiment	112
6.2	Transferring Atoms	114
6.2.1	The Double MOT System	115
6.2.2	Magnetic Guidance	117
6.2.3	Pushing the Atoms	118
6.3	Magnetic Trapping	120
6.3.1	The Magnetic Trapping Principle	121
6.3.2	Field Geometries	122
6.4	The Detector Chamber	123
6.4.1	Vacuum Considerations	125
6.4.2	The Time-Orbiting Potential Trap	125
7	Summary	129
	Bibliography	131
	A Symbols	146

B Ion Optical Calculations	148
C Foil Heating	151

List of Figures

2.1	The basic principle of atomic beam deceleration	16
2.2	Atomic beam detection and collimation	18
2.3	Dipole force trap	19
2.4	The Magneto-Optical Trap (MOT)	23
3.1	The layout of the mass separator.	35
3.2	The ionization efficiency of a surface ionizer	39
3.3	The ionization efficiency of a hot cavity ionizer	41
3.4	The ion source body	46
3.5	A picture of the ion source	48
3.6	The $^{82,85}\text{Sr}$ decay scheme	51
3.7	The resolving power of the mass separator	56
3.8	The ion optics of the mass separator	57
3.9	Typical performance of the mass separator	61
3.10	The LC resonant circuit	62
3.11	A cell to test the foil release	64
3.12	Measured release from the yttrium foil	66
4.1	The efficient Cs-MOT	76
4.2	Cs level diagramm	78
4.3	Trapped Cs atoms	79
4.4	Measurements on the trapped Cs cloud	80
4.5	The trapping efficiency measurement	82
4.6	Coupling a MOT to a mass separator	86
4.7	The laser setup	87
4.8	The laser locking scheme	89
4.9	Image of trapped ^{82}Rb atoms	92
4.10	Calibration of the detector	94
4.11	The blue photon detection scheme	97
5.1	The energy levels of $^{82,85}\text{Rb}$	101
5.2	Trapped ^{82}Rb atoms	103

5.3	The location of the trapping transition	109
5.4	Detuning measurement of the trapped atoms	110
6.1	The overview of the π -asymmetry experiment	113
6.2	The double MOT system	116
6.3	Magnetic guidance	118
6.4	The TOP trap.	127

List of Tables

3.1	The ion source parameters	49
3.2	The mass separator parameters	55
3.3	Release from the catcher foil	68
4.1	MOT capture rate dependencies	72
4.2	Characteristics of dry...lm coatings	75

Chapter 1

Introduction

1.1 The History of Trapping Radioactive Atoms

The techniques to manipulate atoms with laser light developed in the mid and late 1980's [10, 11, 12, 13], and especially the appearance of optical traps in 1987 [9], have promising applications in several areas of science and technology. The atoms in such traps are cooled to temperatures of less than a millikelvin and thus allow the study of a variety of cold atom phenomena. In fact, the realization of Bose-Einstein Condensation (BEC) in a dilute vapor achieved in 1995 [14, 15, 16] relies heavily on the existence of such traps to serve as a "production source" for pre-cooled atoms.

Shortly after the first optical traps were realized, it became obvious that the cooled atoms in optical traps could be used in high-precision measurements with importance to atomic, nuclear and particle physics. Over the years, a variety of proposals have been published to use the trapped atoms in atomic parity-nonconservation (PNC) and nuclear β^- -decay measurements. For example, measurements in a series of Cs isotopes of the mix-

ing between opposite-parity atomic levels were recognized as a method for reducing the systematic uncertainty in the Weinberg angle at low momentum transfer [17, 18].

Unfortunately, the trapping of short-lived atoms has proven to be extremely challenging despite a 5+ year effort by several groups. Nevertheless, with the vision of a new generation of exciting fundamental physics experiments on the horizon, successful trapping of short-lived isotopes was demonstrated at Berkeley and shortly thereafter at Stony Brook in 1994 [5, 19].

At Berkeley, approximately 4000 ^{21}Na atoms had been trapped for the purpose of testing the V-A structure of the electroweak interaction by performing a precise nuclear β^- -decay measurement [5]. Similarly, $\gg 80$ ^{79}Rb atoms had been trapped at Stony Brook in a proof-of-principle experiment, aimed at the trapping of ^{210}Fr for a possible atomic PNC measurement [19]. Fr is expected to be a superb candidate for a atomic parity non-conservation measurement since the parity-violating amplitude is predicted to be 18 times larger than in Cs. After the demonstrated trapping of ^{79}Rb , it took two more years to demonstrate the successful trapping of ^{210}Fr at Stony Brook with $\gg 1000$ atoms in an optical trap [20].

In 1997, a third group successfully trapped radioactive atoms. At TRIUMF, a neutral atom trap was connected to the ISOL beam line for the trapping of ^{37}K and $^{38}\text{K}^m$ [21]. The very short half-life ($t_{1/2} \gg 1\text{s}$) of these isotopes make it even more challenging to trap sufficiently large numbers for the use in a nuclear β^- -decay measurement. To date, 2000 and 6000 atoms of ^{37}K and $^{38}\text{K}^m$, respectively, have been trapped.

Herein we report on the successful trapping of $\gg 6 \times 10^6$ ^{82}Rb atoms for the use in a

nuclear β -decay measurement. Accomplished in October 1997 this number of trapped atoms is 100 times larger¹ than in any other experiment. The achievement of a large number of trapped radioactive atoms represents a fundamental breakthrough since, for the first-time-ever, the number of trapped atoms is now sufficiently large to make a proof-of-principle electron-nuclear spin correlation (A) measurement realistically possible with a statistical precision of 1% and the potential to extend this sensitivity to the 0.1% level.

1.2 Preview of this Thesis

This thesis describes the magneto-optical trapping experiment performed at the Los Alamos National Laboratory. The experiment is designed to optically trap a large number of radioactive atoms and to prepare the trapped atoms for a high-precision nuclear β -decay measurement. The careful investigations and improvements of all the components used in the experiment to efficiently trap radioactive ^{82}Rb atoms in a magneto-optical trap are presented.

1.2.1 Introduction to Laser Cooling

Laser light provides a perfect tool to prepare, manipulate, and detect atoms. While the theory of light-atom interactions is described in some detail in the next chapter, we will present here only the basics of atomic cooling and trapping.

Atoms consist of a rather heavy nucleus formed of neutrons and protons surrounded by a cloud of much lighter electrons that move in orbitals of well defined energy. Normally, the electrons occupy the orbits with the lowest possible energy. Upon irradiation by light,

¹compared to the improved trap at Berkeley that now traps 40000 atoms [6]

the electron can absorb a photon and be promoted from a lower orbit of energy E_1 to a higher orbit of energy E_2 . Simultaneously, the light intensity is decreased since one photon has been absorbed. Since this process has to fulfill energy conservation, the difference in energy $E_2 - E_1$ has to equal the photon energy $h\nu$,

$$E_2 - E_1 = h\nu \quad (1.1)$$

Furthermore, conservation of momentum implies that when absorbing a photon of momentum h/λ , the atom must gain a momentum,

$$Mv = M\Delta v = h/\lambda \quad (1.2)$$

where M is the mass of the atom, and λ is the wavelength of the laser light. In other words, the atom undergoes a velocity “kick” of $h/M\lambda$ along the direction of photon absorption. Upon de-excitation, the atom will experience an additional kick in the direction opposite to the photon emission direction.

1.2.2 Doppler Cooling

Now consider an atom initially at rest, that is illuminated with two counter-propagating laser beams, one from the right and the other one from the left. When the frequency ν of the light is chosen in such a way that the corresponding energy $h\nu$ is less than the energy difference $E_2 - E_1$ of the two electronic levels, one expects nothing to happen since there is insufficient energy to excite the transition. Suppose now that instead of the atom being at rest, the atom is moving at some velocity \vec{v} towards one of the laser beams and away from the other. To the atom, the frequency of the laser beam that it is moving toward appears slightly higher in energy, the light is shifted to the “blue”. Conversely, the

frequency of the laser beam the atom is moving away from is shifted to the “red”, having a lower energy. This is called the Doppler effect, which we are all familiar with from listening to police car sirens passing by on the street.

As a consequence of the Doppler effect it is now much more likely for a fast-moving atom to absorb a photon which has been blue shifted onto the transition. The process described here is coupled to the direction of the atoms velocity vector. On the other hand, the spontaneous de-excitation of the atom by fluorescent photon emission is strictly random with respect to direction. As a result, the repeated absorption of re-detuned photons and fluorescence of the atom will slow the atom down (i.e. cool the atoms). The same argument can be made if the atom initially moves in the opposite direction, except that the roles of the two lasers are reversed. Thus, no matter which direction the atom moves, it will be slowed down and cooled as a result of its interaction with the laser beams. This extremely simple mechanism is called Doppler or optical Molasses cooling [22] and works very effectively, but because there is no position dependence in this mechanism it does not confine the atoms in space. In fact, it turns out to be impossible to completely stop the atom with this mechanisms, because eventually one reaches the single photon recoil limit. The lowest temperature achievable with Doppler cooling is found to be a few millikelvin for Rb atoms.

A scheme to confine atoms in space is realized in the so called Magneto-Optical Trap (MOT) [9] which is explained in detail in the second chapter. Briefly, a magnetic field gradient is used to cause Zeeman splitting of the atomic energy levels into magnetic sub-states which, in combination with circular-polarized laser beams, gives rise to a position

dependent force that pushes the atoms back to the magnetic field minimum at the center of the trap. The MOT traps atoms from the low velocity tail of the Maxwell-Boltzmann distribution. Thus, one can define a capture velocity which is a measure of the efficiency of the trapping process. A detailed investigation of the trapping efficiency of the MOT and how to improve it is given in Chapter 4. The various studies of the trapping efficiency have led to a more efficient version of the MOT which we use to cool and confine the radioactive atoms in our experiment.

1.2.3 Trapping of Radioactive Atoms

A basic requirement when pursuing a trapping experiment with radioactive atoms is the development of an efficient way of introducing the atoms into the MOT. We have chosen a scheme, that ionizes the atoms in an ion source, separates them in a mass separator and implants the mass-separated ions into a catcher foil located within the vacuum chamber of the MOT. Finally, the implanted ions are released as neutral atoms upon heating of the catcher foil into the MOT where they are trapped. This scheme requires the development of an efficient ion source, a high-transmission mass separator, and a coupling scheme for the mass separator compatible with the requirements of the MOT. Its realization can be found in Chapter 3 together with a detailed description of the laser setup.

In Chapter 5, we describe our results that show the successful trapping of $\gg 6 \times 10^6$ radioactive ^{82}Rb atoms in a magneto-optical trap, a dramatic improvement over previous trapping experiments.

In order to obtain high trapping efficiency, high sample polarizations, and efficient γ -detection, a double MOT system is advanced. The first MOT is optimized for efficient

trapping and the second for long trap lifetimes, high polarizations and σ^+ -detection. Using a laser push beam, magnetic guide approach the atoms in the first MOT are efficiently transferred to a second MOT / σ^+ -detection chamber. Upon retrapping of the atoms in the second MOT, but prior to loading the atoms into the magnetic moment trap, we need to optically pump the atoms into the “weak-field seeking” $|F = 3/2; m_F = 3/2\rangle$ stretched magnetic sub-state, which spin aligns the nuclei. A description of the process used to transfer the atoms into the second MOT, as well as the preliminary design of the magnetic moment trap is given in Chapter 6.

Chapter 2

Cooling and Trapping of Neutral Atoms

Einstein's discovery of the "momenta of light quanta" in 1917 [23] introduced the idea of manipulating the external degrees of freedom of an atom by the absorption and emission of light quanta. Following Einstein's pioneering work, Frisch first observed the deflection of an atomic beam by light pressure in 1933 [24]. However, since the effect of the thermal light source on the atomic beam is very small, it did not seem to be feasible to pursue this idea any further.

The situation changed dramatically with the invention of the laser [25]. In 1975, Hänsch and Schawlow suggested that atoms could be cooled by counter-propagating laser beams detuned to the "red" of the atomic transition [26]. Ten years later Chu et al. applied this technique to create a gas of cold sodium atoms which they named "optical molasses" [27, 22]. Atoms in the optical molasses are cooled to low temperatures but not confined

in space. Dalibard proposed a scheme to simultaneously cool and confine those atoms by using polarized light fields and adding a magnetic field gradient (in closing remarks of [9]) in such a way, that the atomic transition of atom which is moving away from the magnetic field minimum, is shifted into resonance and therefore, the atom experiences a force, that pushes the atom back to the center of the trap. This configuration was first realized by Raab et al. in 1987 [9] and is now well known as the “Magneto-Optical Trap (MOT)”.

The early theoretical discussions were based on the two-level atom and therefore quoted the lowest attainable temperatures T in an optical trap to be $kT \gg \frac{1}{2}\hbar\gamma$, where k is Boltzmann’s constant [28, 29, 30]. It was surprising that lower temperatures were observed by Phillips et al. [31]. Since then, considerable theoretical and experimental effort has focussed on understanding “new” cooling mechanisms which led to much lower temperatures [32]. It is known that the temperature limit for the so-called sub-Doppler cooling is proportional to the recoil energy $kT \gg \hbar^2 k^2 / m$. But even the limit of one photon recoil was underscored with techniques based on “dark resonances” [33] or “Raman cooling” mechanisms [34].

The importance of laser cooling and trapping was acknowledged in 1997 when the Nobel Prize in Physics was awarded to Steven Chu, Claude Cohen-Tannoudji, and William Phillips for extraordinary work in the area of laser cooling and trapping [35, 36, 37].

In this chapter, we will derive the basic formulas that lead to the trapping force and, in addition, give some details on the possible trapping configurations. Concluding, the reader finds a brief selection of possible applications of atomic traps and some of the interesting physics experiments that can be performed with the help of optical traps.

2.1 Light-Atom Interaction

2.1.1 Basic Considerations

Laser cooling of free atoms is based on the principles of light-matter interaction, well described by QED. The numerous degrees of freedom present in the complex cooling schemes do not allow theory to present a complete and detailed description of optical cooling and trapping. Especially a 3-D model of the commonly used MOT still needs to be developed. Nevertheless, theory has succeeded in describing the basic cooling scheme by using clever assumptions and simplifications. A brief description of the mean force model is given here, while a more detailed treatment can be found in [38].

Following the notation used in [39], the total Hamiltonian of the combined system can be written as

$$H = H_{\text{atom}} + H_{\text{field}} + H_{\text{int}} ; \quad (2.1)$$

where H_{atom} , H_{field} , and H_{int} are the atom, field, and interaction Hamiltonian. In the weak field assumption the vacuum field and the atom-vacuum interaction can be neglected.

The Hamiltonian for a two-level atom is

$$H_{\text{atom}} = \frac{p^2}{2m} + \hbar \omega_0 b^\dagger b ; \quad (2.2)$$

where p is the atomic momentum, m is the mass of the atom, ω_0 is the transition frequency between the ground and the excited states $|g\rangle$ and $|e\rangle$, while $b^\dagger = |e\rangle\langle g|$ and $b = |g\rangle\langle e|$ are the atomic raising and lowering operators. If the photon momentum is small compared to the atomic momentum, the kinetic energy term in (2.2) remains approximately constant and might be neglected, which is known as the Raman-Nath approximation [39].

The Hamiltonian of a light field with a single laser mode L is given by

$$H_{\text{field}} = \hbar \omega_L a_L^\dagger a_L ; \quad (2.3)$$

with a_L^\dagger and a_L being the creation and annihilation operators for a photon with energy $\hbar \omega_L$.

Finally, in the electric dipole approximation [39]

$$H_{\text{int}} = -\mathbf{d} \cdot \mathbf{E}_L(\mathbf{r}) ; \quad (2.4)$$

where $\mathbf{d} = d_{ge} \mathbf{e}_z (b + b^\dagger)$ is the electric dipole moment of the atom and \mathbf{e}_z defines the alignment of the dipole.

2.1.2 The Optical Bloch Equations

The dynamics of the atom is described by the Liouville equation for the reduced density matrix ρ_A . In the interaction picture this can be written as

$$\dot{\rho}_A = -\frac{i}{\hbar} [H; \rho_A] ; \quad (2.5)$$

If the light field is treated semi-classically, which requires the modification of the light field to be small by individual absorption and emission processes, the light field Hamiltonian may be neglected. In the case of an atom interacting with a free propagating laser, this is a good assumption since the number of photons in the light field is large compared to the number of absorbed and emitted photons. Using the Raman-Nath approximation the resulting Hamiltonian can be written as

$$H = \hbar \omega_L b^\dagger b - \mathbf{d} \cdot \mathbf{E}_0(\mathbf{r}) \cos[\omega_L t + \mathbf{A}_L(\mathbf{r})] ; \quad (2.6)$$

The density operator for the atomic state ρ_A is given by the trace over the field states \mathcal{F} of the density operator for the combined system $\rho_{\mathcal{F}}$;

$$\rho_{jj} = \text{Tr}_F(\rho_{jj}); \quad (2.7)$$

or in matrix form

$$\rho_{ij} = \langle i | \rho_{jj} | j \rangle = \sum_L \langle i | L \rangle \langle j | L \rangle \rho_{LL} = \sum_L \rho_{LL} \langle i | L \rangle \langle j | L \rangle; \quad (2.8)$$

The time dependence in (2.6) is eliminated by transforming into a rotating frame by substituting;

$$\rho_{ge} = \rho_{ge} e^{-i\omega_L t}; \quad \rho_{eg} = \rho_{eg} e^{i\omega_L t}; \quad \rho_{gg} = \rho_{gg}; \quad \rho_{ee} = \rho_{ee}; \quad (2.9)$$

Spontaneous emission is included by adding damping terms to (2.5). Since the population of the excited state ρ_{ee} decays at a rate γ_1 (where $\tau_1 = 1/\gamma_1$ is the spontaneous life-time) and the coherences ρ_{eg} and ρ_{ge} decay at a rate γ_2 , the damping terms have the following form:

$$\mu \frac{d}{dt} \rho_{ee} = -\gamma_1 \rho_{ee}; \quad (2.10a)$$

$$\mu \frac{d}{dt} \rho_{gg} = -\gamma_1 \rho_{gg}; \quad (2.10b)$$

$$\mu \frac{d}{dt} \rho_{eg} = -\gamma_2 \rho_{eg}; \quad (2.10c)$$

$$\mu \frac{d}{dt} \rho_{ge} = -\gamma_2 \rho_{ge}; \quad (2.10d)$$

Another change of variables;

$$u = \frac{1}{2}(\rho_{ge} + \rho_{eg}); \quad v = \frac{1}{2}(\rho_{ge} - \rho_{eg}); \quad \text{and } w = \frac{1}{2}(\rho_{ee} - \rho_{gg}) \quad (2.11)$$

leads to the optical Bloch equations;

$$\dot{u} = -\gamma_2 u + \Omega v; \quad (2.12a)$$

$$\dot{v} = -\frac{1}{2} \Omega u - w \quad (2.12b)$$

$$\dot{w} = -v - \frac{1}{2} \Omega u \quad (2.12c)$$

The steady state solution of the optical Bloch equations is

$$\begin{aligned} u_{st} &= \frac{\Omega}{\gamma} \frac{S}{(1+S)}; \\ v_{st} &= \frac{1}{2} \frac{S}{(1+S)}; \\ w_{st} &= -\frac{1}{2} \frac{1}{(1+S)}; \end{aligned} \quad (2.13)$$

where $S = \frac{1}{2} \Omega^2 / \gamma^2 = (\frac{1}{2} \Omega^2 + \frac{1}{4} \gamma^2)$ is known as the saturation parameter and γ is the on-resonance Rabi frequency.

2.1.3 Light Forces

These general results are now used to determine the mean force on an atom in a light field. The force on an atom due to a perturbation H_{int} is given by Ehrenfest's theorem,

$$\mathbf{F} = \hbar \langle \mathbf{p} | [H_{int}, \mathbf{p}] | \mathbf{p} \rangle = \hbar \langle \mathbf{p} | \mathbf{r} | H_{int} | \mathbf{p} \rangle = \hbar d \langle \mathbf{r} | \mathbf{E}_0 \cos(\mathbf{k}_L \cdot \mathbf{r} + \mathbf{A}_L) | \mathbf{p} \rangle \quad (2.14)$$

We find by using equation (2.3) that the time-averaged force is

$$\langle \mathbf{F} \rangle = d_{ge} (u_{st} \mathbf{r} \cdot \mathbf{E}_0 + v_{st} \mathbf{E}_0 \cdot \mathbf{A}_L) \quad (2.15)$$

where u_{st} and v_{st} are the steady state in-phase and quadrature components of the atomic dipole moment. The force has two components. The first term

$$\mathbf{F}_{dip} = \frac{1}{2} d_{ge} u_{st} \mathbf{r} \cdot \mathbf{E}_0 \quad (2.16)$$

is proportional to the gradient of the field and is known as the gradient force or dipole force.

The dipole force arises from the redistribution of photons in the light field by absorption

and stimulated emission cycles. The second term,

$$F_{\text{spont}} = \hbar k_L v_{\text{st}} E_0 r \hat{A}_L ; \quad (2.17)$$

is proportional to the gradient of the phase and is known as the radiation pressure force or spontaneous force because it arises from absorption and spontaneous emission cycles.

The physical meaning of F_{spont} is particularly clear for a plane wave, where the gradient of the phase is equal to the k -vector. With the definition of the Rabi frequency $\Omega(r) = \hbar^{-1} \mathbf{e}_z \cdot \mathbf{d}_{ge}(r) E_0(r)$ and the steady state solution of the optical Bloch equations, the steady-state spontaneous force becomes

$$F_{\text{spont}}^{\text{st}} = \hbar k_L \frac{1}{2} \frac{\Omega^2}{\Omega^2 + \frac{\Gamma^2}{4} + \Delta^2} ; \quad (2.18)$$

or (with the Rabi frequency re-written in terms of laser intensity, $\Omega = \sqrt{\frac{I}{I_s}}$)

$$F_{\text{spont}}^{\text{st}} = \hbar k_L \frac{1}{2} \frac{I}{I + I_s(1 + 4\Delta^2)} ; \quad (2.19)$$

where $I_s = \hbar c \epsilon_0 \omega^3$ is the saturation intensity. This form now clearly shows the dependence of $F_{\text{spont}}^{\text{st}}$ on the various parameters. At low intensity the spontaneous force is proportional to the intensity. At high intensity, the force saturates at $\hbar k_L \frac{1}{2}$. Even though the photon momentum $\hbar k_L$ is small, the radiation pressure force can be substantial ($\gg 10^5$ times the earth's gravitational force) because of the scattering rate Γ (typically 10^8 s^{-1}) being large. We notice that the velocity dependence appears through the detuning resulting from the Doppler shift, $\Delta = \omega_L - \omega_0 \approx k_L v$, where v is the velocity of the atom. The velocity dependence allows laser cooling and trapping.

The dipole force $F_{\text{dip}}^{\text{st}}$ arises from a coherent redistribution of photons within the

light field. This becomes clear if one uses the expression (2.13) for u_{st} and re-writes

$$F_{dip}^{st} = i \frac{\hbar \Phi}{2} \frac{-\mathbf{r} \cdot \nabla}{\Phi^2 + i \frac{\Gamma}{2} + \frac{\Gamma^2}{4}} : \quad (2.20)$$

For a plane wave, the amplitude and the polarization of the laser field are independent of \mathbf{r} so that $\mathbf{r} \cdot \nabla$ vanishes. It follows that $F_{dip}^{st} = 0$ for a plane wave. The dipole force can only appear if the laser field is a superposition of several plane waves. On the other hand, since the dipole force is associated with the reactive response of the atom, it cannot involve a net absorption of energy. Therefore F_{dip}^{st} is associated with the redistribution of photons between the various plane waves that form the laser field.

We also notice that, unlike the spontaneous force, the dipole force does not saturate. For $I_L < I_0$ the atom is attracted towards regions of high intensity and for $I_L > I_0$ the atom is repelled.

Finally, note that the dipole force derives from a potential U since we can write

$$F_{dip}^{st} = -\mathbf{r} \cdot \nabla U ; \quad (2.21)$$

where

$$U(\mathbf{r}) = \frac{\hbar \Phi}{2} \ln \left(1 + \frac{\Gamma^2}{\Phi^2 + i \frac{\Gamma}{2}} \right) : \quad (2.22)$$

2.1.4 Deceleration of an Atomic Beam

Atomic beam deceleration was the first experimental investigation of laser cooling and trapping in the mid 1980s [10, 11] and stimulated the following steps of atom manipulation. The basic scheme (see Figure [2.1]) uses the spontaneous force to reduce the velocity of a thermal atomic beam with a counter-propagating laser beam. A fixed-frequency laser,

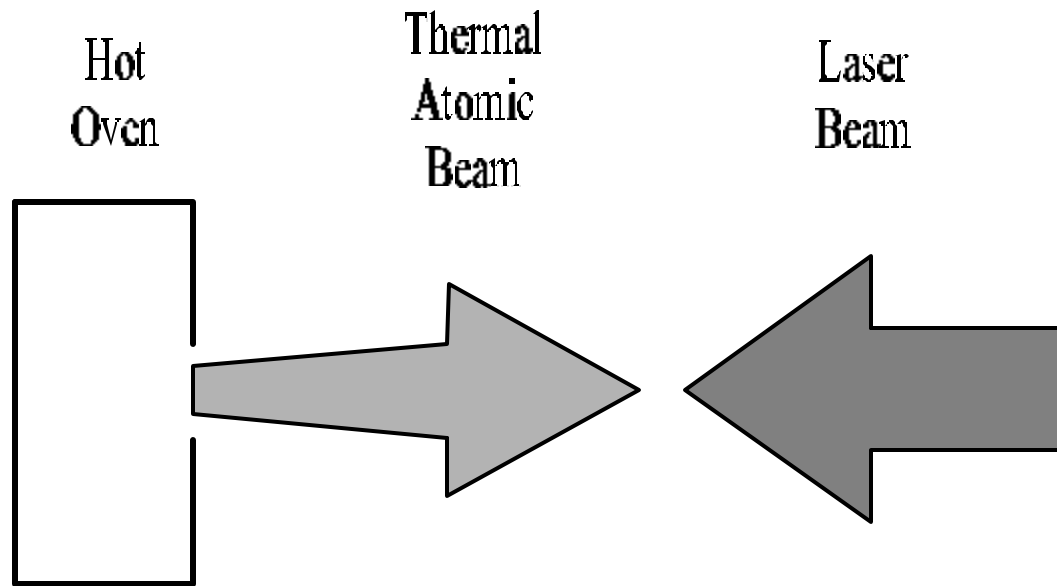


Figure 2.1: The basic principle of atomic beam deceleration is shown. A sample of atoms is evaporated from a hot oven and creates an atom beam. Since the hot atoms travel with velocities of several hundreds of meters per second, one needs to decelerate the atomic beam prior to loading them into a trap. A counter-propagating, near resonant laser beam slows the atoms down, thus increasing the efficiency of the loading process.

however, is only resonant with a narrow velocity group, leaving the velocity of most of the atoms in the atomic beam unchanged [40, 41, 42]. To overcome this limitation several techniques were developed, the most important ones are known as “chirped slowing” [11] and “Zeeman slowing” [10]. In case of chirped slowing, the laser frequency is swept in time to compensate for the changing Doppler shift and so that the atoms stay in resonance and keep absorbing photons. Zeeman slowing modifies the atomic transition in space by adding an inhomogeneous magnetic field which shifts the energy level of the atom by using the Zeeman effect to keep the atoms in resonance.

The chirp method has a pulsed nature since, at the end of the sweep, the laser frequency is set back to the start frequency to restart the next sweep. As a consequence,

the spatial distribution of the atomic velocities at the end of each sweep tends to be rather complicated, a consequence of the different stopping distances of different initial velocity classes and the different drift periods during individual sweeps. The advantage of this method is of course the simplicity of the implementation, since ramping the laser frequency generally is easily accomplished.

Zeeman slowing, on the other hand, requires a well-designed magnet, especially since the fringing field at the end of the magnet is critical for the width of the final velocity distribution. A sharp rise in the magnetic field strength at the end of the magnet reduces the width of the velocity distribution, but results in a higher peak temperature than chirp slowing, while a smaller slope in the magnetic field amplitude increases the width of the velocity distribution.

Nevertheless, chirped slowing and Zeeman slowing both have been used to load atoms from an atomic beam into optical traps with reasonable efficiencies.

2.1.5 Deflection and Collimation of an Atomic Beam

Deflection of an atomic beam with resonant laser light can be compared to the mass separation of ions commonly used to enhance isotopic purity. The mass separation device for ions, typically a magnetic sector field, is replaced with a laser beam in the case of neutrals, since the laser light affects only the atoms that feature an atomic transition in resonance with the laser light field. Thus, atoms which are in resonance with the laser light are deflected from their original beam path, while atoms that do not feature a transition in resonance with the light field are not affected at all (Figure [2.2]).

The need for collimation of an atomic beam arises whenever one has to increase

the phase space density of the atoms. The idea here is to compress the spatial and velocity distributions of the atoms by using resonant laser light. Typically, an atomic beam is produced by heating a sample of atoms in a hot oven which leads to a thermal beam of atoms that leave the oven through the exit hole. Since this beam is rather divergent, one often uses a collimator to cut down the divergence of the beam but at the price of losing a large fraction of the intensity. The availability of high power lasers enables the collimation of the atomic beam by using the light pressure without losing large amounts of the atoms.

Detailed studies on the collimation of atoms with laser light have been published [43, 44] and have led to large improvements in loading rates of cold atoms into optical traps. However, with the development of optical traps loaded with atoms directly from the alkali vapor in the trapping cell [45], beam deceleration and collimation of atomic beams have lost some of their importance.

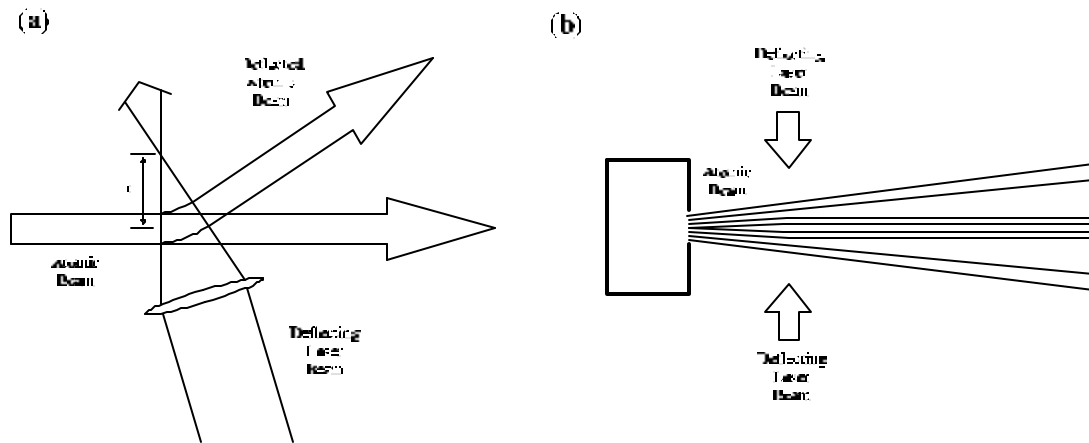


Figure 2.2: Basic atom-light manipulation schemes are shown. Atomic beam deflection with laser light (a) and atomic beam collimation (b) have been investigated in great detail and are commonly used to manipulate the phase space density of the atomic beam.

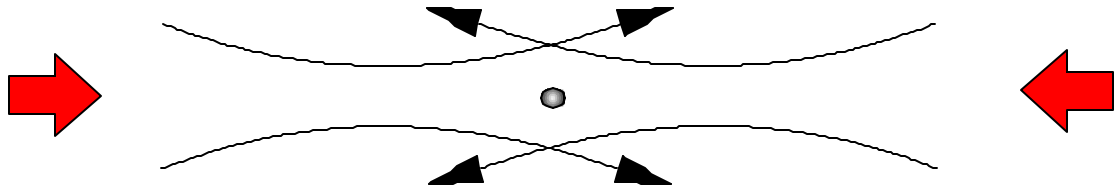


Figure 2.3: Focussed laser beam configuration used in a dipole force laser trap [52].

2.2 Optical Traps for Neutral Atoms

The confinement of free particles has been an experimental goal for a long time. The experimental realization of ion traps by Paul et al. [46] in the 1950s soon raised the question for neutral atom traps. The concept of magnetostatic trapping of neutral particles was first proposed and realized for the neutron by Paul [47] using a geometry suggested by Heer [48]. The first magnetostatic trap for neutral atoms was a magnetostatic spherical quadrupole trap for Na, demonstrated at NIST [49], while the first magnetodynamic (ac) trap was demonstrated at JILA [50]. The “second generation” version of this ac trap finally led to Bose-Einstein condensation. A comprehensive overview of magnetostatic trapping configuration for neutral species can be found in [51].

While magnetostatic and magnetodynamic traps have been the cornerstones for trapping neutral atoms, optical traps are usually simpler to implement and offer a deeper trapping potential. However, in some cases (e.g. BEC and γ -asymmetry measurements), the atoms are cooled in optical traps, but need to be further cooled and stored in magnetic traps and therefore, a combination of optical and magnetic traps is required.

2.2.1 Dipole Force Traps

A second kind of trap widely used in atomic physics experiments is the dipole trap. In this type of trap the dipole or gradient force is combined with the radiation pressure force. The design of such a trap is shown in Figure [2.3]. Two slightly focussed counter-propagating laser beams with Gaussian intensity profiles are used in such a way that their foci are slightly separated. The frequency of the laser light is below resonance, so the dipole force confines the atoms (the ground state light shift is negative so atoms are drawn towards the axis where the intensity is highest). In addition, the scattering force produces axial confinement because atoms moving away from the equilibrium point midway between the two foci experience an increased intensity in one beam compared to the other. The intensity imbalance results in a net scattering force that pushes the atoms back towards the equilibrium point.

Unfortunately, such a trap both cools and heats the atoms. Doppler cooling reduces the kinetic energy of the trapped atoms, but two associated heating mechanisms destabilize such traps. The first effect is the heating arising from the random direction of both absorption and spontaneous emission of light which causes fluctuations in the scattering force. More important at high intensity is the heating associated with fluctuations in the dipole force which is best explained in the dressed atom picture [27]. Briefly, fluorescent decay from an excited state may leave the atom in a state where the optical forces have opposite signs. Thus the atom experiences fluctuating forces that are not correlated to the atoms motion and therefore heats the atoms. These fluctuations do not saturate with intensity and hence cannot be compensated by increasing the trap depth. The result is that

atoms are continuously boiled out of such traps.

Detailed studies of such traps have been performed by Gordon and Ashkin [28]. The first reported optical trap used an alternating (on the micro-second time scale) dipole force trap that confined and heated the atoms and an optical molasses setup that cooled the atoms before they could escape. This version had the simplest possible configuration, a single tightly focussed laser beam whose bright focal spot attracted the atoms and an optical molasses setup to cool. Typical experiments performed in such traps are studies of cold atom collisions.

2.2.2 Radiation Pressure Traps

Trapping of neutral atoms requires a position-dependent force directed towards the center of the trap. Configurations with the laser beams directed to a common center with the laser frequency tuned to the resonance of an optical two-level transition of the atom are excluded by the “optical Earnshaw” theorem. The optical Earnshaw theorem states that the gradient of the scattering force is zero, $\nabla F_{\text{scat}} = 0$, analogous to the force on a charged particle in an electric field where $\nabla F = q \nabla E = 0$. If $\nabla F = 0$ inside some sphere then it is not possible for F to have inward components everywhere on the surface of that sphere. Therefore, it is not possible for F to confine particles in all three dimensions. A very detailed discussion with exact proofs of several “no-trapping” theorems is given by Chu in [36].

Several ideas to “overcome” the optical Earnshaw theorem by employing fields with alternating gradients (similar to the rf traps for charged particles) were investigated without being very successful due to the very shallow trap depths associated with the alternating

...eld gradients. The important idea which led to the magneto-optical trap (MOT) came from Pritchard et al. [53] who realized that the spontaneous force needs not to be proportional to the intensity if an additional magnetic ...eld shifts the atomic levels of the atom and at least four levels of the atom are considered.

The basic principle of a MOT is easily understood in a simplified 1-D configuration. The mechanism to defeat the optical Earnshaw theorem is shown in Figure [2.4]. The key idea is that a magnetic ...eld in the z-direction shifts the energy levels of the excited states with the magnetic sub-states $m = +1$ and $m = -1$ in opposite directions, thereby shifting the peak of the cross-sections for the absorption of σ^+ and σ^- circularly polarized light to opposite sides of the resonance frequency (the circular polarization is needed to take advantage of the selection rule $\Delta m = \pm 1$). If the laser light is slightly detuned to the red of the transition an atom located at $z > 0$ will experience a net force toward the center of the trap since the cross-section for absorbing σ^- polarized light is much larger than the cross section for absorbing σ^+ polarized light due to the shift of the resonance frequency by the magnetic ...eld. The situation is reversed for an atom at $z < 0$ since the magnetic ...eld reverses sign at the origin, therefore reversing the sign of the net force on the atom. Since the red detuning provides optical cooling this configuration represents a one-dimensional optical trap.

The MOT was first demonstrated by Raab et al. in 1986 [9] and has seen several modifications over the years. There is no general theory of the 3-D MOT in a realistic configuration. Consequently, we do not understand why the MOT, as indicated by several observations, seems to function even when some of the polarizations differ from the con-figu-

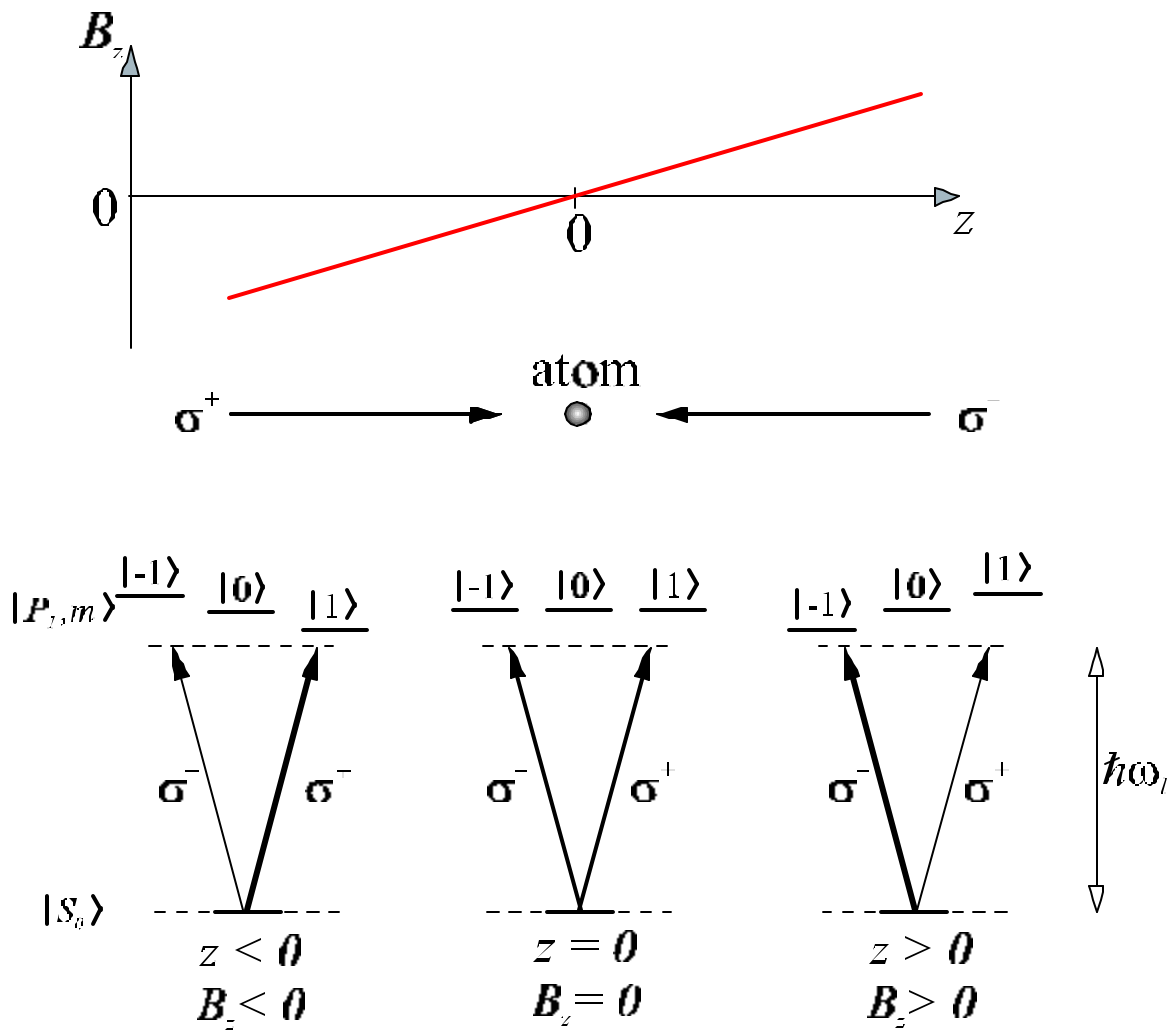


Figure 2.4: An atom in a inhomogeneous field $B_z(z) = bz$ is illuminated by circularly polarized $\frac{1}{2}\lambda$ light propagating in the $\pm z$ direction. The atom has a S_0 ground state and a P_1 excited state. At $z = 0$, in the presence of no magnetic field, the atoms absorb equal quantities of $\frac{1}{2}\lambda^-$ and $\frac{1}{2}\lambda^+$ polarized light. When the magnetic field is greater than zero the atom absorbs more $\frac{1}{2}\lambda^-$ than $\frac{1}{2}\lambda^+$ photons, thus the atom experiences a net force toward the origin. Similarly, at a position where the magnetic field is less than zero the atoms absorb more $\frac{1}{2}\lambda^+$ than $\frac{1}{2}\lambda^-$ photons, again resulting in a net force towards the center. The laser frequency ω_l is red detuned to provide optical damping as in optical molasses.

ration described in the 1-D model. In addition it has been shown that a slight misalignment of some of the laser beams cause the atoms to be somewhat polarized [54].

2.3 Applications of Laser Cooling and Trapping

In the early years of optical cooling and trapping, the focus of the work with traps was the cooling process of the trap itself and related measurements [55, 45, 56, 57]. Those measurements led to the discovery of sub-Doppler temperatures in the trap and a variety of cold-collision measurements with trapped atoms. Only in recent years the neutral atom trap became recognized as a tool to produce cold, relatively dense and well localized samples for high-precision measurements in the area of atomic and nuclear physics. Here, a brief summary of interesting proposed and already realized experiments is given which use an optical trap as a tool rather than studying the trapping process itself.

2.3.1 Bose-Einstein Condensation

The arguably most exciting discovery in the area of atomic physics in recent years is the realization of Bose-Einstein condensation (BEC) in a dilute alkali vapor. About 70 years ago the stage was set by Einstein [58] when he predicted, based on work by Bose [59], that at extremely low temperatures a phase transition would occur. Researchers across the globe tried for decades to achieve this goal, mostly by cooling hydrogen atoms to extremely low temperatures. It took the development of a new technology, optical cooling and trapping, to achieve temperatures low enough to make BEC in a dilute vapor seem feasible. In 1995, researchers at the University of Colorado in Boulder cooled a dilute gas of

Rb atoms to temperatures of about 180 nK and densities of 2.5×10^{12} atoms per cm^3 [15]. Shortly thereafter, a group at the Massachusetts Institute of Technology reached equivalent temperatures and densities for a sample of Na atoms [16].

In both cases, the atoms are first loaded from the vapor into a MOT in which temperatures of a few μK , and densities of $\gg 10^{10}$ atoms per cm^3 can be achieved. The density of the trapped atom cloud in a MOT is limited due to re-radiated photons absorbed by the atoms in the trap itself. Thus, at this point a different type of trap has to be used which does not need the presence of laser light to confine the atoms. Various kinds of magnetic traps have been developed to confine neutral atoms [51]. In the absence of the laser light, the trapping potential is created by the interaction of the magnetic field with the magnetic moment of the atom. Hence, atoms can be stored and further cooled. Unfortunately, magnetic traps with a vanishing magnetic field at the center, e.g. magnetic quadrupole traps, allow Majorana spin-flip transitions to occur in the zero magnetic field region which allow the cold atoms to leak out of the trap. While traps with a non-zero magnetic field at the center have been used for several years, these kind of traps suffer from a less tight confinement potential than quadrupole traps. As a result the density of the atom cloud decreases which hinders the presence of the condensate. At the University of Colorado, Eric Cornell and co-workers developed a magnetic trap which avoids losses due to Majorana spin-flips and features a very tight confinement potential [60]. This new type of magnetic trap uses a quadrupole potential which guarantees tight confinement of the atoms, whereas a rotating bias field plugs the leak typical for quadrupole traps. The trap has been called TOP (Time Orbiting Potential) trap and it represents not only a very elegant solution

to achieve extremely long life-times in a magnetic trap but shows very desirable features for high-precision measurements as well. With this new tool in hand to keep atoms trapped for hundreds of seconds, further cooling processes can be used to lower the temperature of the trapped atoms. The use of a technique called “evaporative cooling” [61] has proven to be a very efficient way to cool the ensemble of atoms to much lower temperatures and increase the density dramatically, while losing only a small percentage of the trapped atom cloud.

At the temperatures and densities mentioned above, a sharp deviation from the typical Gaussian velocity distribution appears, indicating the creation of a BEC. Atoms in a BEC form a new state of matter which now can be studied. As a result of those achievements many groups around the world now use BEC’s to study fundamental quantum mechanical behavior such as two BEC interferometry, the atom laser, and the properties of the BEC (i.e. the speed of sound and collective excitations of the BEC).

2.3.2 Atomic Parity Non-Conservation

Atomic Parity Non-Conservation (PNC) experiments probe the Standard Model of electroweak interaction by measuring the parity violating effects that arise from the exchange of a Z^0 particle [62, 63]. Historically, atomic PNC experiments are divided into two categories: Stark interference experiments and optical rotation experiments. Detailed descriptions on both types of experiments can be found in the literature [64, 65, 66, 67].

Recently, an extremely impressive experiment was published that measures PNC at a precision of 0.35% using the Stark interference approach to measure the $6S \rightarrow 7S$ excitation rates in atomic Cs [68]. This measurement represents the most accurate measurement of atomic PNC to date, and provides a unique, high-precision test of the Standard

Model. The experiment uses a spin-polarized atomic beam to perform the measurement and, in general, pushes the limits in a variety of techniques used in laser technology. Also, it has taken some 7 years to improve the previous measurement in atomic Cs by a factor of 7. The experimental accuracy is higher than the model dependent theoretical predictions due to uncertainties in the atomic structure (namely the uncertainty in calculating the σ_5 matrix element) [63]. It remains to be seen if theory can match the phenomenal accuracy achieved in atomic Cs.

A possible solution to this unsatisfying situation could be the implementation of ratio measurements of atomic PNC amplitude in a series of Cs isotopes to minimize the uncertainties in the atomic structure [18]. However, these measurements would involve radioactive atoms, and consequently would have to be performed in a trap to compensate for the much smaller sample size. Nevertheless, the realization of an efficient trap for radioactives, as outlined in this thesis, and the availability of a the Cs isotopes of interest could lead to sizable improvement in the measured accuracy, as well as a significant simplification in the theoretical calculations of the atomic structure effects.

Also, one might envision a PNC measurement in Fr since the atomic PNC amplitude is predicted to be enhanced by a factor of 18 due to the larger atomic number ($\propto Z^3$). In Fr, however, the situation is more complicated due to the lack of stable isotopes and one is dealing with the limitations imposed by the necessity of working with radioactives. Nonetheless, our setup could be used for trapping radioactive ^{221}Fr atoms, because of the existence of a strong ^{229}Th source (which feeds ^{221}Fr through the $A = 4n + 1$ alpha-decay chain [69]) and is compatible with our existing setup.

2.3.3 Nuclear β^- -decay Measurements

The reason that nuclear physicists are excited about optical traps is based on the fact that atoms in such a trap provide a nearly ideal system for the study of electroweak interactions. Four decades have past since the first suggestion by Lee and Yang that parity could be violated in the weak interaction [1]. Shortly thereafter, parity violation was discovered in the β^- -decay of ^{60}Co by Wu et al. [2] who measured the electron-spin correlation function (A) with a precision of about 10%. An improved version of the same measurement has now reached a precision of about 2% [3].

Today, maximal violation of parity, and also of charge conjugation symmetry is described by the standard model, vector - axial vector (V-A) interaction between leptons and quarks. Nonetheless, the nature of these helicity couplings is derived from empirical measurements and the standard model offers no fundamental understanding of the origin of these symmetries and how they become broken at energy scales probed by modern experiments. Modern gauge theories imply that spontaneously broken symmetries (such as parity) are restored at higher energy scales. Low energy physics experiments that exploit nuclear β^- -decay continue to offer a means to probe the fundamental origin of parity violation and, more generally, the helicity structure of the weak interaction.

Precision measurements to study parity violation in nuclear β^- -decay rely on the potential deviations from the standard model that would occur beyond the simple V-A structure coupling of quarks and leptons. Consequently, these experiments provide a general probe of the helicity structure of the weak interaction. Parity violation is observed in nuclear β^- -decay as an asymmetry in the angular correlation of the emitted β^- -particles relative to the

nuclear spin orientation of the parent nucleus. Measurements of this electron spin correlation (A) have been made in a host of nuclei over the past forty years [70]. Modern experiments typically achieve a sensitivity to deviations from the standard model predictions at the level of $\gg 1\%$ [4]. Hence, it has taken four decades to improve the sensitivity of such measurements by an order of magnitude. Therefore, the design of a new generation of experiments with a sensitivity of 0.1% is extremely challenging.

To date, there is no clear evidence for deviations from the standard V-A structure described by the standard model. Nonetheless, it is widely believed, that the standard model is incomplete and represents only a low-energy approximation to a more fundamental grand unified theory of the forces of nature. Consequently, new physics beyond the standard model can be found by pushing the sensitivity of modern experiments further. So far, modern experiments study these couplings in purely leptonic (such as in the case of muon decay) or purely hadronic interactions (probed mainly at high energy hadron accelerators). These experiments are complementary with studies of semileptonic interactions, such as in the case of nuclear β -decay. A family of such experiments is ultimately required to understand the helicity structure of the weak interactions between quarks and leptons.

The natural candidate for studying fundamental symmetries in nuclear β -decay is the free neutron, mainly due to its simplicity and the lack of complications related to the nuclear structure effects inherent in heavy nucleus systems. To date, four modern experiments have claimed a sensitivity of about 1% in measuring A in neutron β -decay, although experiments disagree among themselves by as much as 5%. Clearly, the resolution of this discrepancy can only be achieved in new experiments with sensitivities well beyond

the 1% level. It is also clear, that if we are to establish definite evidence for new physics in such experiments, then it will be essential to verify any findings in experiments independent of, but complementary to, experiments exploiting the free neutron.

It is well known, that pure Gamov-Teller (GT) transitions are well suited to study parity violation in nuclear β -decay. The pure GT transitions proceed solely through the axial-vector coupling responsible for parity violation. The nuclear form factors and matrix elements that govern the transition rates cancel in a prescription for the correlation coefficients of interest. Historically, studies of the pure GT transitions have been limited by the lack of good candidates, namely reasonably long-lived species appropriate for α -line sources and the fact that many of the pure GT candidates are hindered transitions. In nuclear orientation experiments, such as ^{60}Co , we find that these experiments are limited at the 2% level of precision due to the fact that implanted samples have limited nuclear polarization and β scattering effects when exiting the solid source. In addition, nuclear recoil effects in heavier atoms limit the ultimate precision of such experiments where one relies on theoretical calculations of the size of these effects (typically on the scale of $\gg 1\%$). It is now possible, to envision a new generation of pure GT experiments with the potential to reach the 0.1% level by exploiting magneto-optical traps for radioactive atoms.

The successful trapping of large numbers of ^{82}Rb atoms in a magneto-optical trap as reported in this thesis is the forerunner of this new generation of fundamental symmetry experiments. ^{82}Rb , a pure and allowed GT β -decaying nucleus, has the appropriate atomic structure and lifetime ($t_{1/2} = 75\text{ s}$) to be investigated in a trap. We are proposing to mount an experiment to measure the electron-spin asymmetry (**A**) from polarized ^{82}Rb in

a magnetic TOP (Time-Orbiting-Potential) trap [60]. In this case, an essentially massless source of highly polarized atoms can be envisioned that is confined to a trapped cloud size of about 1 mm in diameter. An important feature of the TOP trap is that the nuclear spin vector rotates in the equatorial plane following the magnetic bias field as it rotates. Consequently, we intent to explore both the point-like geometry of such a massless source and the “rotating” nuclear polarization vector to measure the electron-spin correlation as a continuous function of electron energy and angle relative to the nuclear spin orientation in a single and fixed electron detector.

This simple geometry has important advantages in controlling and limiting systematic errors. Also, β -scattering effects associated with the finite sample size are effectively reduced. A β -nuclear spin asymmetry function can be defined;

$$\hat{A}(E; \epsilon) = A P^-(E) \cos \epsilon \quad (2.23)$$

where E is the electron energy, $^-(E)$ is the electron velocity relative to the speed of light, ϵ is the angle between the electron momentum vector and the nuclear spin vector, and P is the polarization of the parent nucleus.

In the case of ^{82}Rb with its two β -decay branches ($1^+ \rightarrow 0^+$; and $1^+ \rightarrow 2^+$) the standard model predicted values for A are $+1$ and $-\frac{1}{2}$, respectively. Also, the spin-polarization of the trapped sample is extremely high, since only the weak field seeking spin-states are trapped while the strong field seeking spin-states are repelled. It is also been shown that the population of the atomic spin states can be measured using optical pumping techniques to high precision [68]. Consequently, the global polarization P depends mostly on the properties of the magnetic bias field. In a TOP trap, the global polarization at any

given instant in time is well above 95% and known through measurements to better than 0.1%. Thus, the asymmetry function is maximized for the $1^+ \rightarrow 0^+$ transition and still large, but with the opposite sign for the $1^+ \rightarrow 2^+$ transition. The analysis of the spectrum of these two transitions will enable a good cross check for our measurement.

Secondly, the large number of atoms trapped will produce a high count rate in the γ -detector. Following simple statistical arguments, one would require about 150,000 detected γ -decay events in order to determine the electron spin correlation function to a precision of 1%. Given a realistic detection geometry, these counting statistics could be achieved in one hour with one million trapped atoms. In a multi-day experiment, a 0.1% measurement could be obtained.

And last, but certainly not least, by taking advantage of the TOP-trap, the asymmetry function (2.23) can be mapped out in a continuous fashion by recording the electron energy on an event-by-event basis and reconstructing the angle based on knowledge of the spin-orientation (or magnetic field configuration) at a particular instant in time. Not only will the continuous measure of the asymmetry function enable good systematic cross checks of the measurement, but our hope is to simultaneously extract the recoil order contribution through their higher order (such as $\cos^2 \mu$ dependence) angular correlation contributions to the distribution.

In conclusion, with the successful trapping of a large number of ^{82}Rb atoms, and the design stage of the nuclear γ -decay experiment completed, we are well positioned to implement the magnetic TOP trap for a new generation of high-precision γ -spin correlation experiments.

Chapter 3

The Making of a Radioactive Ion Beam

The detailed investigation of radioactive isotopes has the potential to answer a variety of questions in the area of nuclear and particle physics, ranging from nuclear structure investigations to the search of not yet discovered elementary particles. Radioactive isotopes are produced at accelerator and/or nuclear reactor sites, using a variety of reactions. Due to relatively low accelerator beam currents and/or small production cross sections, only a limited number of radioactive atoms are created, thus efficient ionization, mass separation and transportation to the experimental setup is essential to achieve large quantities of the species of interest. Additional complications arise for the production of short-lived ($t_{1/2} < 100$ ms) isotopes, in which cases the target has to be part of the mass separation device. However, because of the interesting physics results obtainable, a large number of Isotope Separators On-Line (ISOL) have been built to serve as production facilities for

radioactive isotopes despite the technical difficulties involved.

While most of those experiments are mounted at radioactive beam facilities, e.g. ISOLDE and now REX-ISOLDE at CERN, FRS at GSI, TISOL at TRIUMF, and many others, we have designed and built a single stage mass separator at Los Alamos, which has the potential to serve as a production source for a variety of isotopes with a sufficient long half-life or a long lived parent. Such isotopes as ^{82}Rb , ^{221}Fr , and $^{135,137}\text{Cs}$ which can be trapped optically and are interesting candidates for a variety of fundamental electroweak interaction measurements such as nuclear β^- -decay, atomic parity nonconservation, and electric dipole moment measurements.

Here, I will report on the development of the single-stage mass separator, the design and optimization of the thermal ion source, and the release studies performed on several catcher foils, mounted internal to the Magneto-Optical Trap. The layout of the mass separator is shown in Figure [3.1].

3.1 The Sample Preparation

The experiment described here does not require an on-line setup, since the radioisotope of interest can be obtained from the decay of the long-lived parent. Our choice for the β^- -decay experiment is ^{82}Rb (β^- -decay) with a half-life of 75 s. Its main decay channel $1^+ \rightarrow 0^+$ (86%), as well as the $1^+ \rightarrow 2^+$ (13%) decay to ^{82}K are both pure Gamov-Teller transitions. Also, the $1^+ \rightarrow 2^+$ decay is followed by the emission of a 776 keV γ -ray which allows, by analyzing the angular distribution, for a cross-check of the polarization of the trapped atom cloud. The relatively long half-life of ^{82}Rb is well suited for an optical trap

Figure 3.1: The layout of the mass separator is shown. While the mass separator is drawn to scale, the ion source region is magnified by a factor 10. The cut out shows the cubic trapping cell in more detail. At the entrance of the trapping cell, a collimator is mounted which allows the beam current to be monitored. High transmission is verified by minimizing the ion beam current on the collimator and maximizing the beam current measured at the catcher foil.

based experiment, and the availability of the long-lived parent ^{82}Sr ($t_{1/2} = 25$ d) simplifies the experimental setup considerably. ^{82}Sr is produced at several accelerator facilities worldwide and is commonly used in medical γ -ray imaging procedures. We obtain the ^{82}Sr activity from the Los Alamos Medical Radioisotope Production Program. ^{82}Sr is produced for the manufacture of $^{82}\text{Sr} / ^{82}\text{Rb}$ medical generators. In detail, molybdenum targets are irradiated with 800 MeV protons at the Los Alamos Neutron Science Center (LANSCE). After receiving an integrated current of up to one ampere-hour the targets are dissolved in hydrogen peroxide and processed using ion-exchange techniques to recover curie quantities of strontium radioisotopes. Typically equal quantities of ^{82}Sr and ^{85}Sr are produced in an irradiation. Prior to loading the activity into the ion source of the mass separator the strontium is converted to the carbonate by precipitation using ammonium carbonate. The strontium carbonate is washed with ethyl alcohol and transferred to a pipette tip. After being dried it is vibrated into the crucible using a commercially available engraving tool. Because significant quantities of activity are handled in this procedure, all operations are performed in one of the Los Alamos Hot Cells.

3.2 Thermal Ion Sources - Theory of Operation

Any hot enclosure is a thermoionizing device regardless of shape or material. Thus, thermal ion sources are in principle very simple devices. Nevertheless continuous improvements both in the theoretical understanding and the experimental operation of these devices have been made since the early 20s.

Around 1920 Saha derived equation (3.1) for the understanding of stellar atmo-

spheres [71], especially to interpret the spectroscopic data available from the solar chromosphere. He found that the ionization efficiency α is given by

$$\alpha = \frac{\mu_i \cdot \frac{n_i}{n_0}}{1 + \mu_i \cdot \frac{n_i}{n_0}} \quad (3.1)$$

$$\begin{aligned} \text{where } \mu_i &= 2 \frac{\frac{3}{4}_i}{\frac{3}{4}_0} \cdot \frac{1}{2} \frac{m}{h^2} \frac{1}{P} (kT)^{\frac{5}{2}} \exp(-W_i/kT) \\ &= 6.67 \times 10^{-4} \frac{\mu_i}{\frac{3}{4}_0} \frac{1}{P_{[\text{mbar}]}} T_{[\text{K}]}^{\frac{5}{2}} \exp\left[-\frac{W_i}{11605 T_{[\text{K}]}}\right] \end{aligned} \quad (3.2)$$

where $\frac{3}{4}_i$ is the ratio of the statistical weights of the ionized and neutral particles respectively, P is the pressure in mbar, T is the temperature in Kelvin, and W_i is the first ionization energy of the sample. Five years later Langmuir and Kingdon [72] applied Saha's equation to the ionization of cesium vapor at a tungsten surface of 1200 K. Instead of the predicted 0.1% ionization efficiency from Saha's equation the measured ionization efficiency was roughly 100%. The authors immediately found the reason for the discrepancy. The assumption of quasi-neutrality $n_e = n_i$, which leads to Saha's equation is not correct in this case. Instead, the electron density is determined by Richardson's law. As a result Langmuir and Kingdon found the ionization efficiency α of a hot surface to be given by

$$\alpha = \frac{R}{1 + R} \quad (3.3)$$

$$\text{where } R = \frac{\mu_i}{\frac{3}{4}_0} \exp\left[-\frac{(\phi_i + W_i)}{kT}\right] \quad (3.4)$$

where ϕ is the work-function of the surface ionizer. Equation (3.3) was exclusively used for the next 50 years to determine the ionization efficiency of hot surface ionizers. In the

early 70s however, groups in Livermore [73] and Dubna [74] investigated high temperature cavities for the ionization of lanthanide elements. Again, much higher ionization efficiencies were found than expected, but this time higher than predicted by the Langmuir equation (3.3) and well described by the Saha equation. The breakthrough came in 1975 when Latuszynski and Raiko [75] found a dependence of the ionization efficiency upon the value of the extracted ion current, which was believed to be explainable by a thermal plasma generated by the flow of thermionic electrons and surface ionized ions into the volume of the ionization chamber. Finally, in 1978 Kirchner and Piotrowski proved the equation derived in Reference [75] to be identical to Saha's equation (apart from a factor of 1.47) [76].

As a result of the historical developments and despite the same basic ionization process, thermoionizer will be classified here in two categories, depending on temperature and configuration due to significant differences in the achievable ionization efficiencies.

3.2.1 The Surface Ionization Source

The first category discussed here is the surface ionization source. Successfully used as a source for on-line separators [77, 78] it has proven to be very reliable due to its simplicity. The ion source consists of a high-temperature ionizer made of a high-work function material such as tantalum, tungsten, or rhenium for the production of positive alkali ions ($W_i \approx 5 \text{ eV}$). A version with a LaB_6 ($W_i = 2.6 \text{ eV}$) pellet is used for the production of negative ions following the same principle for instance at ISOLDE or OSTIS [78, 79, 80, 81].

The general behavior of surface ionization sources is plotted in Figure [3.2]. High

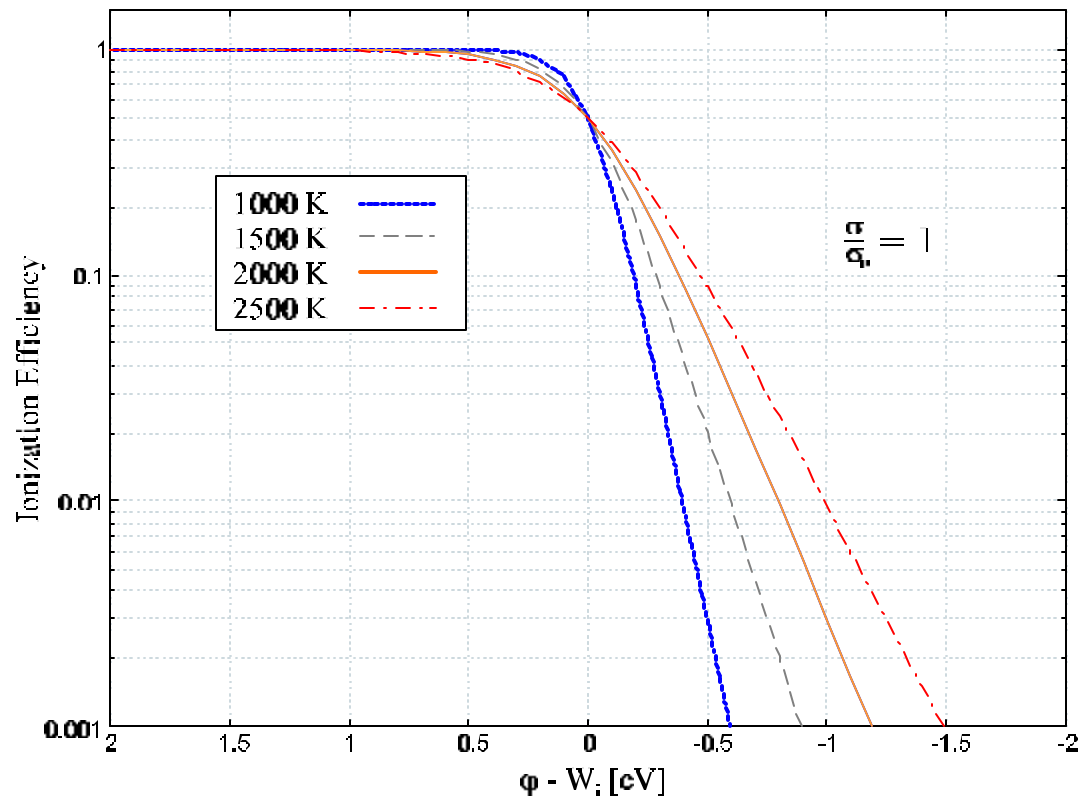


Figure 3.2: The theoretical ionization efficiency of a hot surface is plotted versus the difference in the work-function of the ionizer material and the ionization potential of the element of interest for a temperature range of 1000 - 2500 K

and relatively independent ionization efficiencies for $W_i < \phi$ and a strong dependency on both the temperature and the ionization potential for $W_i > \phi$ are well understood and often used for selective ionization [82].

Despite the fact that the ionization efficiency decreases with higher temperature, the ionizer must be hot enough to evaporate the element of interest. On the other hand, the diffusion process and the surface coverage must stay small enough to preserve the characteristics of the ionizer material. Thus, the control of these processes is the main task when designing a surface ionization ion source. Lifetimes of ion sources in continuous

operation can be more than 2000 h, strongly depending on the ion source design and the characteristics of the sample to be ionized.

3.2.2 The Hot Cavity Ion Source

The hot cavity ion source has proven to be extremely suitable for the on-line separation of ultra small amounts of radioactive isotopes. Such ion sources feature high-ionization efficiencies for most of the elements in the periodic table. Evenly important, due to the small volume of the ionization chamber and the extremely high temperatures of the ionizing surfaces, a hot cavity ion source features very short hold-up times of the ions within the cavity. The latter is extremely important for the on-line separation of short-lived radioactive isotopes [83, 84, 85].

The superiority of the hot cavity ion source is illustrated in Figure [3.3]. Setting arbitrarily a lower limit of 1% for a minimum ionization efficiency, one finds that surface ionization gives access to elements with an ionization potential $W_i \leq 6.3 \text{ eV}$, including 25 elements of the periodic table. Since the hot cavity ionizer is more efficient, as illustrated in Figure [3.3], one achieves an ionization efficiency of 1% for elements up to $W_i \leq 8.1 \text{ eV}$; which puts 34 additional elements within reach.

The higher ionization efficiency of the hot cavity ion source was vaguely attributed to “volume ionization” caused by a “thermal equilibrium plasma” within the cavity [75]. Despite the lack of any experimental evidence of such a phenomenon, it was tacitly accepted to dominate the surface ionization within the cavity by orders of magnitude. This assumption can be associated with a law in Reference [75]. Years later, it was shown that the assumption of a “thermal equilibrium plasma” within the hot cavity is at least very

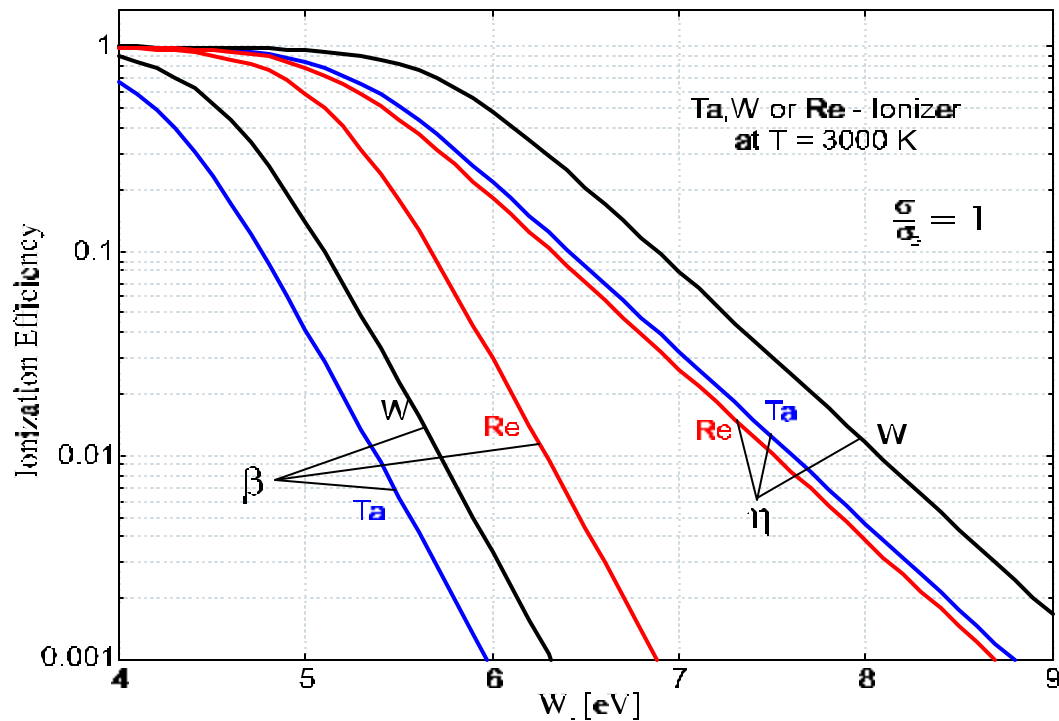


Figure 3.3: Theoretical ionization efficiencies for elements with ionization potentials between 4 and 9 eV due to surface ionization (β) and a "thermal equilibrium plasma" (η). The ionization efficiencies are calculated for $\frac{\gamma_i}{\gamma_0} = 1$, but are applicable for any value of $\frac{\gamma_i}{\gamma_0}$; if W_i is replaced by $W_i^0 = W_i - 0.26 \text{ eV} \approx \ln(\frac{\gamma_i}{\gamma_0})$: The material dependence is due to the different work functions of the cavity materials for surface ionization, whereas in the case of "thermal equilibrium plasma" the different vapor pressures of the cavity materials cause different ionization efficiencies. Plot taken from Ref. [86].

doubtful [76]. In the case of the standard tungsten cavity, in fact, it was proven that the assumption of a thermal equilibrium is simply incorrect [86]. If one abandons the picture of a plasma, which is responsible for "volume ionization", the only ionization effect of relevance is surface ionization. This now leaves us with the puzzling situation that tungsten ions are created at the surface of the tungsten cavity with an efficiency of $\beta = 3 \times 10^{-6}$ but extracted from the volume with an efficiency of $\eta \approx 1\%$: The explanation for such an obvious discrepancy is given in Reference [87].

Briefly, an atom suffers during its time inside the cavity a mean number of wall collisions \bar{N} ; which is given by the ratio of inner surface of the cavity to the orifice area. The ionization probability for each collision with the wall is given by Langmuir's equation. Whenever an atom gets ionized, it has a relatively large "trapping" probability β (typical values for β have been measured to be between 0.1 and 1) inside the plasma formed at high temperatures (2800 K), which is negatively charged due to a larger emission of glow electrons compared to positive ions, resulting in a negative charged ion trap from which positive ions can be extracted with high efficiencies. This can be expressed by the following equation

$$\beta = 1 - \frac{1}{N} \quad (3.5)$$

Thus, the product βN acts as an effective "enhancement factor" to the normal surface ionization efficiency given by Langmuir's equation (3.3). A similar description in the case of the "thermal equilibrium plasma", however, leads to an amplification factor N_{TE} . As a general rule one finds $N_{TE} \gg \beta N$ for any hot cavity ion source, which effectively proves the assumption of a thermal equilibrium plasma to be incorrect.

More detailed descriptions of thermal ion sources can be found in Reference [88, 89]. As a summary, the following recommendations are made in the literature. Despite the fact that the theoretical ionization efficiencies of hot cavity ion sources do not depend on the work function of the ionizer material, rhenium ionizer have proven to be superior to versions made of tungsten or tantalum. This effect is due to the finite number of wall collisions of the atoms that govern the "true amplification factor" βN . The good agreement between measured ionization efficiencies and the predicted ionization efficiencies by the "thermal

equilibrium plasma” to be accidental.

- * Since the trapping probability Γ shows a strong dependency on the temperature of the cavity and the density of neutral particles within, the introduction of neutral atoms into the cavity in the form of noble gases has proven to be advantageous.
- * The required high temperatures of 2800 K and beyond call for a compact design, except in the case of true ISOL sources where a decoupling of the ionizer and the window/catcher region is necessary due to the mechanical properties of electrical isolators and windows at temperatures above $\gg 2000$ K.

3.3 The Ion Source - Experiment

Based on the theory and the experimental results described above, we have designed and built a hot cavity thermal ion source, used to ionize the desired Rb isotope. At a temperature of $\gg 2200$ K the ion source operates strictly in “surface ionization” mode, thus using the large difference in the work-function of Rb and Sr to predominantly ionize Rb, while the Sr at best leaves the ion source in the form of neutral atoms. In addition, to suppress the loss of Sr, the use of the carbonate allows a chemical separation to occur, since SrCO_3 releases CO_2 above a temperature of 1610 K, hence after the initial “bake-out” the carbonate is converted to the oxide (SrO), which is extremely refractory [90]. After this conversion process and the decay of ^{82}Sr , the remaining rubidium oxide is thermally not stable, thus releasing the radioactive ^{82}Rb easily. Despite the exclusive operation as a surface ionizer it is obvious, that the ion source has high ionization efficiencies for a large variety of elements when operating in hot cavity mode.

Extremely high temperatures typical for a hot cavity ion source, require the design to be optimized for the reliable operation in a very hostile environment. Even though the crucible is the only part heated to temperatures in excess of 3000 K, radiative heating causes the ion source body to reach temperatures well above the melting point of stainless steel. Hence, materials with extremely high melting points need to be used throughout the source. Possible candidates for the ion source body are tungsten, rhenium and tantalum.

The use of tungsten is very desirable, especially since tungsten features an extremely low vapor pressure at high temperatures. Unfortunately, its mechanical properties are not suitable for ordinary machining processes. Large expenses are unavoidable when rather complicated shapes need to be machined. Rhenium, while featuring very desirable properties, very low vapor pressure at high temperatures and reasonably good machinability, is extremely expensive, hence should only be used where its physical properties can not be matched by other elements. Tantalum has a higher vapor pressure than tungsten, but still withstands high temperatures well. The material is rather inexpensive and can be machined using ordinary tools. We decided to design the ion source body using stackable tantalum blocks. The use of several blocks instead of one solid piece allows easy access to the filaments, which is rather important when handling radioactive isotopes to minimize personnel exposure.

A drawing of the crucible and the ion source is shown in Figure [3.4]. A technical detail should be mentioned. Many ion source designs use a two piece crucible to simplify the loading procedure. As a result, one suffers from losses due to sample evaporation through the joint of the crucible. The design described here, eliminates those losses altogether by

laser welding the two pieces of the crucible together before the activity is loaded. Despite using a noble gas atmosphere during the welding process, an oxide layer is formed. However, it is been shown that baking crucibles under UHV conditions at temperatures exceeding 2500 K removes any oxide layer that might be present. We extensively bake the crucible within the ion source prior to loading the activity for 24 hours. We found that, this bake not only removes the oxide layer, but other contaminants, mostly potassium and sodium, are clearly detectable at the focal point during this initial bake-out.

In case of Rb we use a crucible made of tantalum, for elements with higher ionization energies the tantalum crucible may be replaced by a tungsten or rhenium crucible to boost the ionization efficiency. The crucible is heated by electron bombardment from two filaments. The basic principle of the hot cavity ion source was successfully demonstrated at Dubna [74] for the separation of rare-earth isotopes. This ion source design provided high ionization efficiencies, very stable operation conditions and a very small energy spread of ≈ 0.2 eV, and consequently is well suited to mass separators.

Key features of the ion source when operating in the hot cavity mode are

1. For $v < W_i$ the ionization efficiency increases with increasing temperature of the ionizer. Therefore the highest possible temperature of the ionizer is preferable.
2. The sample evaporation should not depend on the ionizer temperature, thus a second filament is used to control the vaporization of the sample.
3. In order to increase the ionization efficiency of the ion source, the crucible should allow multiple bounces of the atom within the cavity to increase the ionization probability of the atom.

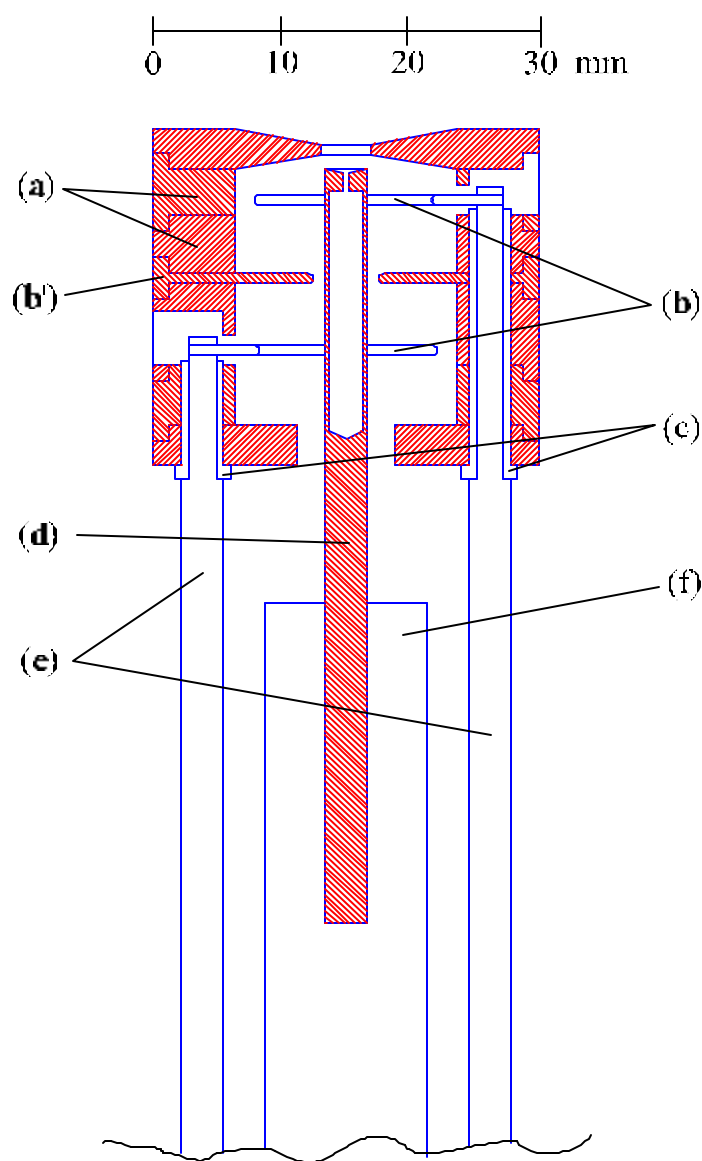


Figure 3.4: A cross sectional view of the ion source body and the crucible is shown. (a) Stacked tantalum "washer" form the ion source body and act as a heat shield; (b) dual filament arrangement, the tantalum collimator (b') between the two filaments minimizes cross talk between the filaments; (c) boron nitrate is used as a high-temperature isolator between the ion source body and the current carrying tantalum conductor (d) tantalum crucible, note the large surface area of the cavity compared to the small orifice; (e) tantalum conductors; (f) stainless steel holder with K-type thermocouple.

All three aspects are fulfilled in the ion source described here. The ion source, a picture is shown in Figure [3.5], is designed to fit the existing separator and it additionally allows the adjustment of a variety of important ion source parameters. Most importantly, the temperature of the tip of the crucible is monitored directly by an optical pyrometer, whereas the temperature of the sample is estimated by measuring the temperature of the crucible holder with a K-type thermocouple.

The ion source design features a x-y-axis manipulator, which allows the exact positioning of the crucible with respect to the theoretical beam line. A translation stage in the base of the ion source provides an additional z-axis adjustment of the crucible, minimizing losses in the extractor region by adjusting the spacing between the front of the crucible and the ion source can, which also serves as a first extractor lens.

Geometrical details as well as typical operation conditions of the ion source are listed in Table [3.1]. After loading the radioactive sample into the crucible and installing the crucible into the ion source, we perform the following tune-up procedure (a small amount of Rb_2CO_3 is added for this start-up procedure).

The ionizer filament power is raised to $\gg 30$ W which illuminates the tip of the crucible. After the crucible becomes visible (for this procedure a telescope replaces the optical pyrometer and thus allows the in situ adjustment of the ion source/crucible location relative to the extractor), we first adjust the location of the ion source with respect to the extractor opening. This is done, by adjusting the x-y translation stage built into the ion source. After this adjustment, the crucible and the ion source opening is centered onto the theoretical axis of the beam path.

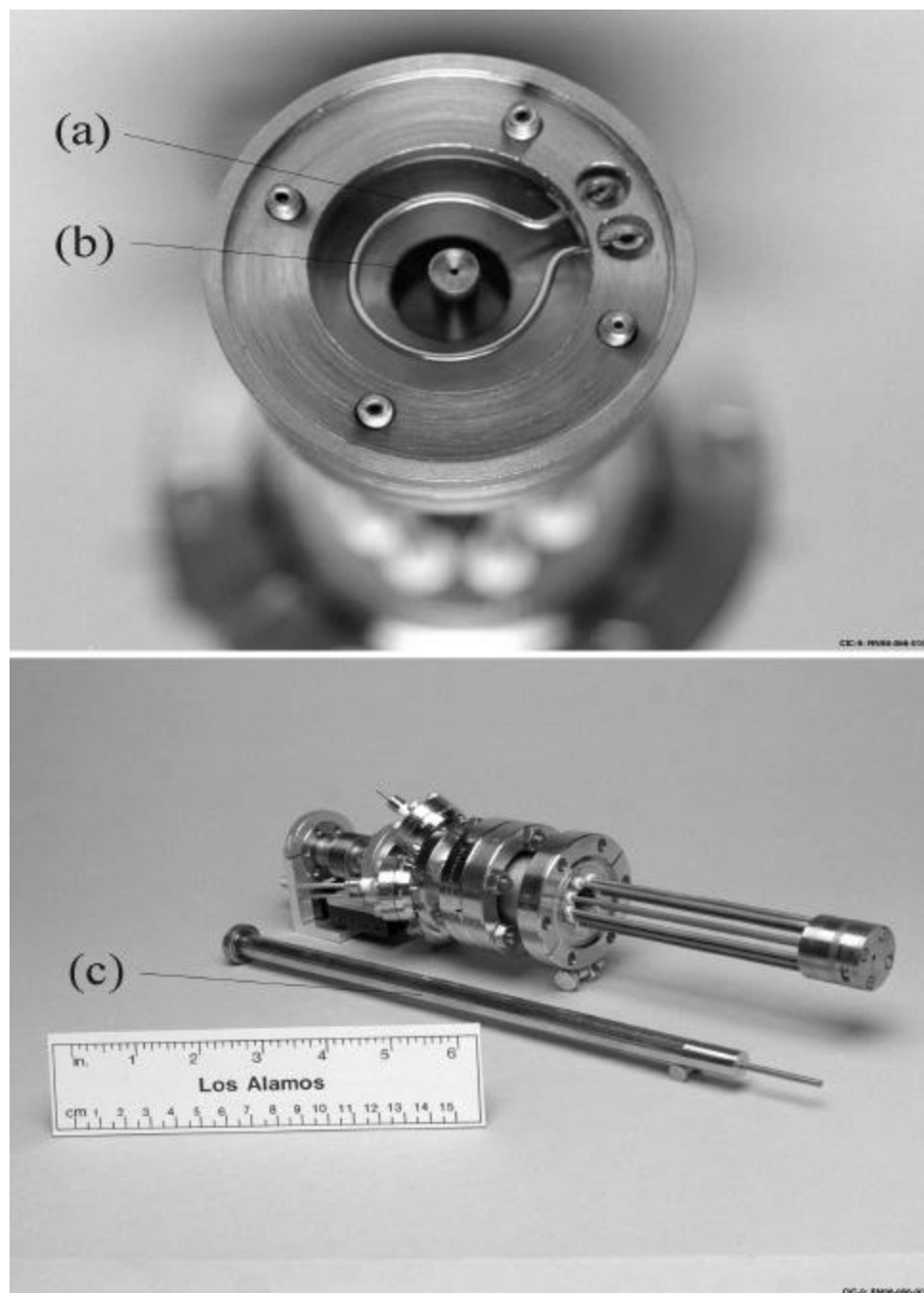


Figure 3.5: In the upper picture, the first filament ("ionizer (a)"), and the tantalum crucible (b) is shown. The crucible is heated by two independent filaments to allow the bombardment of the front and the back of the crucible with little cross talk. Ideally, the filament in the front (a) only heats the tip of the crucible, thus controlling the ionization efficiency, while the filament in the back controls the vaporization rate of the sample; The lower picture shows the hot cavity ion source. The crucible is mounted into a stainless steel holder (c) which is inserted from the back of the ion source.

Characteristics of the Hot Cavity Ion Source

Ion Source Dimensions

Extraction hole diameter	3 mm
Spacing (crucible - extraction hole)	3 mm
Crucible diameter	3 mm
Orifice diameter	0.5 mm
Cavity depth	19 mm
Cavity volume	135 mm ³
Cavity surface area	193 mm ²

Filament Dimensions

Filament	0.75 mm diameter, Ta wire
Filament geometry	single turn, 10 mm diameter
Filament resistance	0.3 -
Filament spacing (ionizer - vaporizer)	12 mm

Ion Source Operation Conditions

EB acceleration voltage	2500 V
Ionizer current	25 A
Vaporizer current	20 A
Ionizer power	58 W
Vaporizer power	55 W
Resulting bias power	45 W

Temperatures

Tip temperature (measured with optical pyrometer)	2200 K
Base temperature (measured with K-type thermocouple installed in stainless steel base)	850 K

Table 3.1: The ion source parameters are shown. Note: The spacing between the crucible and the extraction hole is listed as 3 mm. However, this value can be varied and needs to be optimized prior to performing the experiment.

In a second step, we turn off the quadrupole triplet, apply the desired acceleration voltage, and insert a CsI coated screen into the beam path (mounted at the entrance of the magnetic dipole). Now, the ionizer power is slowly increased until the ion beam becomes visible at the screen. The voltage between the ion source and the extractor lens (extraction voltage) is adjusted to create a focus at the location of the screen. In case of a perfect alignment of the ion source, the focus is centered at the screen. If any misalignment of the ion beam is noticeable, the acceleration voltage is turned off and the location is appropriately adjusted.

After the successful alignment of the ion source, the extraction voltage is adjusted to form a circular ion beam with a diameter of $\approx 1.5 - 2$ cm at the entrance of the magnet. The screen is removed, the magnetic dipole is adjusted to the appropriate setting, and a second CsI coated screen is inserted at the focal plane. Now, the quadrupole triplet is turned back on and the ion optical solution is verified by adjusting the quadrupole triplet appropriately.

Following this step, the screen is removed, the second quadrupole triplet is turned on, and the ion beam is measured at the collimator and the catcher foil. The correct ion optical solution is verified by minimizing the ion beam current at the collimator and maximizing the ion beam current at the catcher foil. At this position, the fresh sample in the crucible is degassed over a period of ≈ 2 h, by slowly increasing the ionizer and vaporizer power.

3.3.1 Ion Source Diagnostics

The hot cavity ion source contains ^{82}Sr and ^{85}Sr due to the isotropic insensitivity of the chemical separation process. The decay properties of those two isotopes can provide a powerful tool to track the radioactive ions throughout the separator. The decay schemes for ^{82}Sr and ^{85}Sr are shown in Figure [3.6].

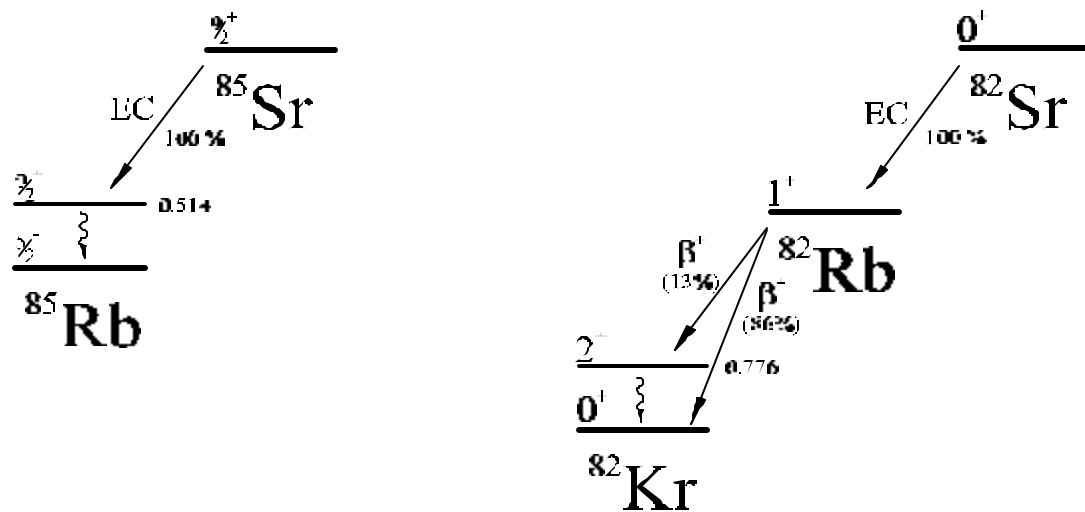


Figure 3.6: The decay scheme of the two Sr isotopes contained in the sample is shown. The ^{82}Sr -decay chain contributes both 511 and 776 keV γ -lines to the γ -spectrum, whereas only one γ -line at 514 keV results from ^{85}Sr decay.

The first isotope, ^{82}Sr , decays by electron capture to ^{82}Rb , which is a β^+ -emitter with two main branches. 13.7% of the atoms decay to the first excited state in ^{82}Kr , which decays to the ground state by emitting a 776 keV γ -ray. The majority of the atoms, 85.8% to be exact, decay directly to the ground state in ^{82}Kr . The endpoint for the two β^+ -decays are 2.57 MeV and 3.35 MeV, respectively. A very small fraction (0.5%) of the atoms decays by emitting a β^+ -particle with an endpoint of 1.88 MeV, which is neglected in the following discussion of the obtained γ -spectrum. All β^+ -particles will annihilate and two 511 keV

γ -rays per π^+ will be observed. The decay scheme for ^{85}Sr is very similar. ^{85}Sr also decays by electron capture, but it decays to an excited state in ^{85}Rb which in turn, decays to the ground state by emitting a 514 keV γ -ray.

In summary, one expects to find three peaks in the γ -spectrum. Due to the relatively poor energy resolution of NaI-detectors used here, the 511 keV γ -ray from the annihilation of the π^+ -particles and the 514 keV γ -ray from the ^{85}Rb decay will not be resolved. Since the goal is to track the ^{82}Rb ions in the separator, the γ -detector only needs to be able to resolve the 776 keV γ -ray from the 511-514 keV γ -rays.

A collimated NaI detector is located at the ion source region, perpendicular to the crucible, to monitor the release of activity due to ionization and vaporization from the ion source. A second detector is located near the trapping cell, perpendicular to the ion beam, monitoring the accumulation of ^{82}Rb in the catcher foil. Typical spectra are shown in Figure [3.9] and [3.12].

3.4 Mass Separation of Isotopes

Mass separation of isotopes goes back to the early 30s when the first mass spectrograph successfully separated the different potassium isotopes [91]. Many separator designs have proven to be capable of fulfilling the requirements of isotope separation [92, 93, 94, 95, 96, 97]. In particular the solution, which consists of an intense ion source and an electrostatic lens forming a parallel beam into a magnetic sector field, has proven to be very successful [98].

Over the years improvements have been made in maximizing the transmission and

the mass resolving power of the particular separator. While the mass resolving power in the case of the simple, single stage mass separator usually is limited to $M/\Delta M \approx 2000$ (at the most 5000), double stage separators feature minimal image aberrations and achieve a mass resolution large enough to separate elements within one isobar [94]. These separators, however, require the use of small apertures within the beam path, effectively limiting the achievable transmission of the separator to 20% or less.

3.4.1 The Mass Separator

The layout of the separator is shown in Figure [3.1]. Ions are electrostatically extracted by an extractor lens with an opening diameter of 6 mm, mounted 8 mm in front of the ion source. The potential of the extractor is adjusted to achieve a beam diameter of 15-20 mm at the entrance of the magnetic dipole, thus determining the maximum inclination to $\alpha_0 = 0.008$ ($\alpha_0 \approx \tan^{-1} \theta_0$). Following the extractor and acceleration region, a pair of x-y steering units is installed to correct for any misalignment of the ion beam which can not be corrected by aligning the ion source. Under normal operation conditions, however, these steering units are turned off. The ion beam enters an electrostatic quadrupole triplet with an effective length of 153 mm per electrode, a spacing of 25 mm, and an aperture of 60 mm. The last quadrupole lens in the triplet can be used for steering purposes as well. After the ion beam leaves the quadrupole, it is passed on to a 90° magnetic sector field with a gap of 10 cm, a bending radius $\rho = 1.6$ m and normal entry and exit angles [99].

Maximizing the transmission rather than extremely high mass resolution was the goal when designing the "first stage" of the mass separator, since the mass difference of ^{82}Sr and ^{82}Rb can not be resolved with a single stage mass separator without dramatic

losses in the transmission capabilities of the device [94]. As a result of those requirements, high transmission and a moderate acceleration voltage (around 20 kV were used), the ion optics features a vertical beam cross over at the exit of the magnetic sector field. Thus, the quadrupole triplet was tuned to not only create the correct virtual image of the ion source but also to y-focus the ion beam as well. The ion optical calculations are performed with GIOS [100], a software package developed for the simulation and design work of ion optical devices. The predicted values of the quadrupole voltages and the magnetic dipole settings are within 10% of the experimentally optimized values¹ listed in Table [3.2].

Two possible ion optical solutions are calculated. The first maximizes the mass resolving power. It features a x-focus at the focal plane with a mass line being about 1.5 mm wide and 10 mm tall with a y-focus at the exit of the magnetic dipole. This solution was verified by detector arrangements in the focal plane (see Figure [3.7]).

The second solution creates a circular spot of about 3 mm diameter without a y-focus in the beam path. Both solutions feature high transmission through the first stage of the mass separator, but maximum mass resolution is achieved when the x-focus is created at the focal plane and a mass resolution $M/\Delta M = 1700$ amu has been calculated (Figure [3.8]) and experimentally verified.

The “second stage” of the separator simply refocuses the ion beam onto the final target, in our case a metal catcher foil (6 mm diameter) located inside the glass cell where the atoms are optically trapped. We are using a second quadrupole triplet of the same type as used before the magnet, which is positioned close enough to the focal plane to collect all the mass-selected ions and far enough away from the catcher foil to deliver a re-

¹A GIOS file can be found in the Appendix.

Chracteristics of the Single-Stage Mass Separator

Ion Source Settings	
Acceleration voltage	20012 V
EB acceleration voltage	2473 V
Ionizer current	18.9 A
Vaporizer current	23.3 A
Ionizer power	55 W
Vaporizer power	57 W
Resulting bias power	48 W
Extractor voltage	844 V
First Quadrupole Settings	
Electrode I	140 V
Electrode II	208 V
Electrode III	
x-axis pos.	211 V
x-axis neg.	123 V
y-axis pos.	129 V
y-axis neg.	205 V
Second Quadrupole Settings	
Electrode I	360 V
Electrode II	748 V
Electrode III	
x-axis pos.	458 V
x-axis neg.	385 V
y-axis pos.	363 V
y-axis neg.	473 V

Table 3.2: The mass separator parameters are shown. Note: The third electrode in each quadrupole triplet can be used for beam steering purposes. This value can be varied and need to be optimized in the tune-up process.

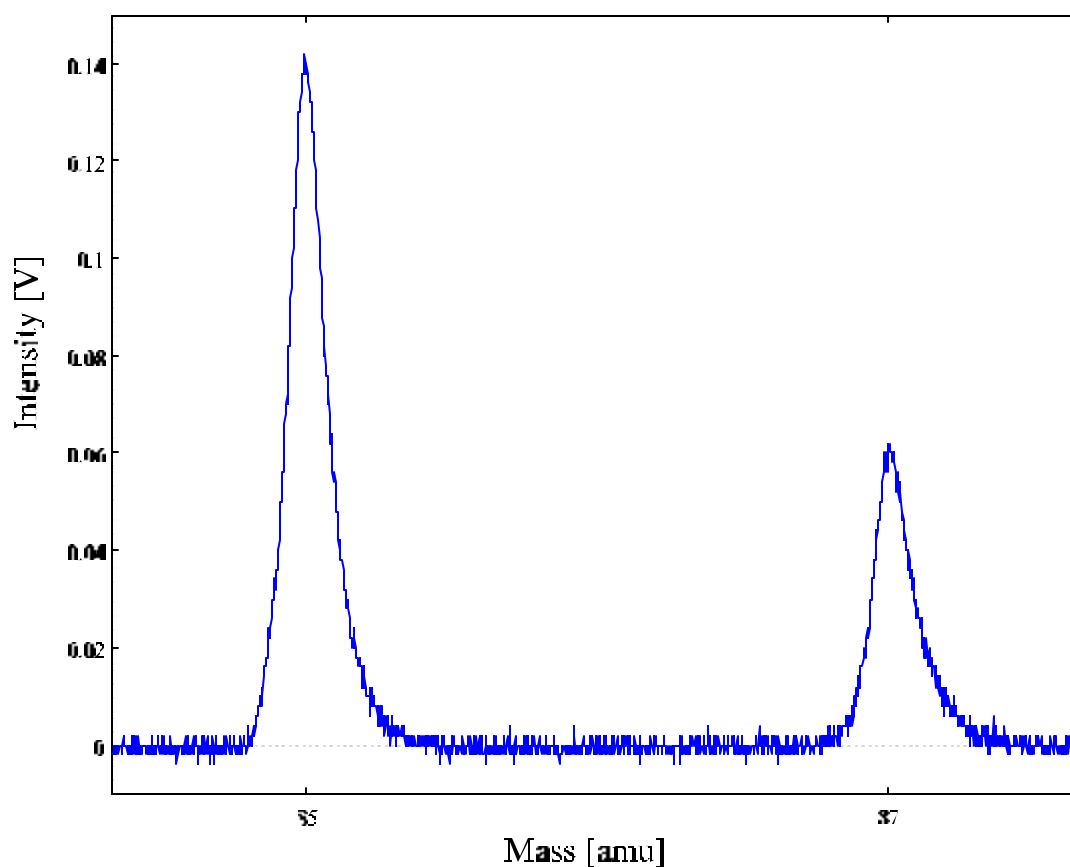


Figure 3.7: A typical mass spectrum of the single stage separator. Shown are the peaks for ^{85}Rb and ^{87}Rb taken directly from the scanning wire detector when operating in the standard mode, that optimizes the transmission of the mass separator. The mass resolution in this scan is determined to be $\gg 600$ amu, but scans that show a mass resolutions of up to 1700 amu have been experimentally observed.

focused beam through the entrance opening of the glass cell. In a typical ^{82}Rb experiment, we measure an ion beam current of $\gg 20$ pA at the catcher foil and a residual ion beam current of $\gg 3$ pA at the collimator. However, when collecting the ^{82}Rb beam entirely on the stainless steel collimator, we measure a total ion beam current of $\gg 120$ pA. We believe that the difference is caused by the different secondary electron emission coefficients of yttrium and stainless steel. This hypothesis is strengthened by the fact, that we can not

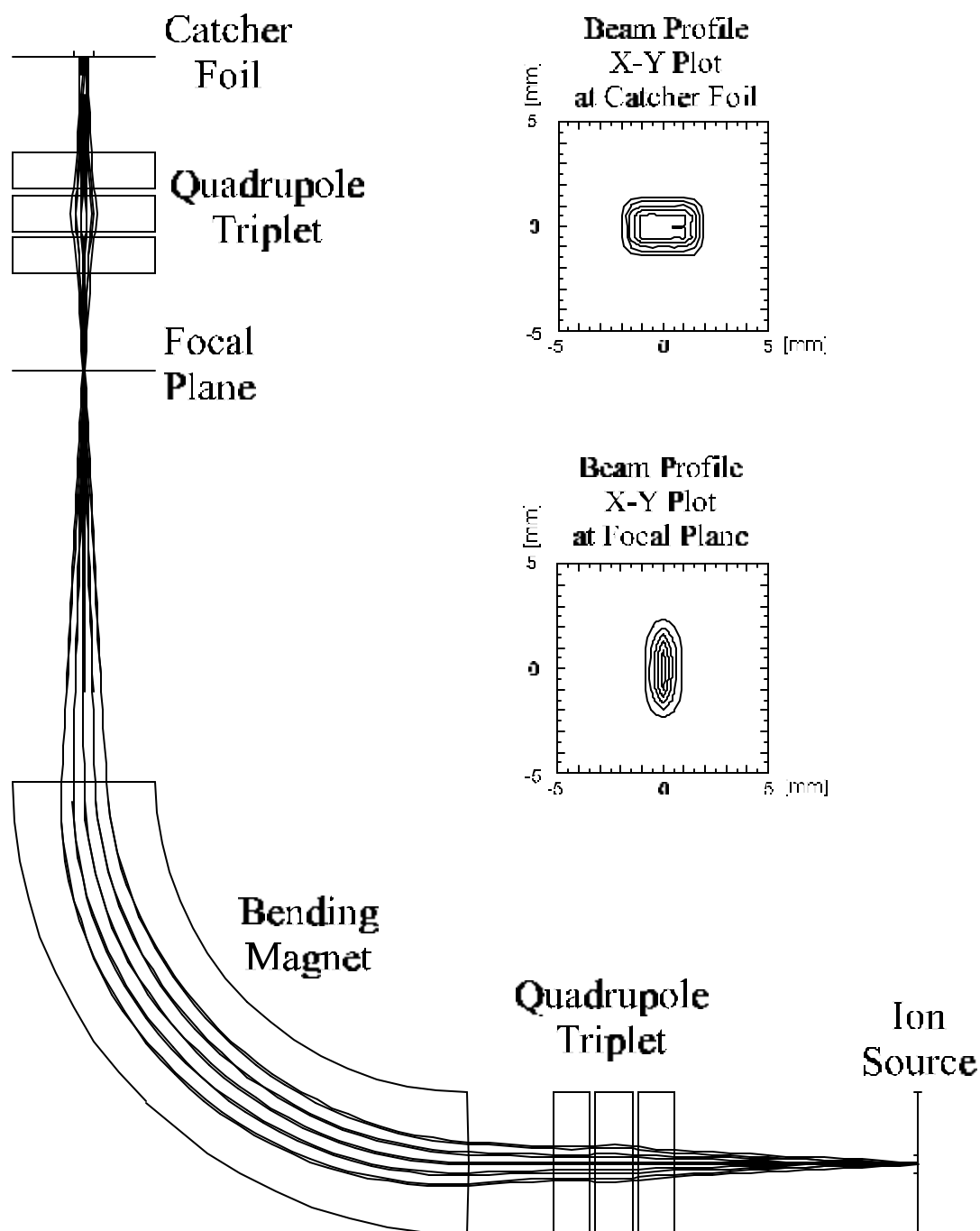


Figure 3.8: The ion optical solution for high transmission throughout the mass separator is shown and ion optical coordinates are used. These coordinates are defined so that the z-axis follows the ion beam resulting in z-x defining the horizontal plane while z-y defines the vertical plane of the mass separator.

locate significant amounts of activity at the collimator or the surrounding vacuum chamber by using γ -counting techniques.

A detailed discussion of the trapping cell geometry, the mounting of the catcher foil, and the laser beam characteristics is given in Chapter 4.

3.4.2 Ion Beam Diagnostics

Reliable high transmission operation of the mass separator is a very important issue for the experiment, since a high flux of ^{82}Rb ions onto the catcher foil is most desirable. Proper operation of the separator is assured by using a variety of diagnostic tools installed within the separator to allow a simple, quick test of the quality of the ion optical properties of the ion beam. We are using Faraday cups, scanning wire detectors and CsI coated screens to visualize the beam shape at several locations inside the mass separator. The first set of diagnostics is installed in between the pair of steering plates right after the acceleration column.

At this location we have the following diagnostics:

1. A Faraday cup measures the total beam current;
2. An x-y scanning wire detector measures the beam profile;
3. And a CsI coated screen allows the visualization of the beam shape at this location.

A second screen located at the entrance of the magnetic dipole allows, in combination with the screen between the steering plates, the determination of the angular divergence of the beam. The divergence of the ion beam is typically set to mrad.

Traditionally most of the diagnostics tools are located in the scattering chamber at the focal plane of the magnet. Here we use a double shielded Faraday cup, a scanning wire detector, a CsI coated screen and locating pins to assure proper operation of the separator. The presence of a strong ion beam (the intensity of ^{85}Rb ion beam is typically a factor-of 1000 higher than the ^{82}Rb beam intensity) in nearby the Faraday cup requires the use of a double shielding, to avoid fluctuations in the ground potential due to the presence of scattered secondary electrons. These secondary electrons are caused by residual gas scattering of the strong ion beam and can hit the ground plate of the Faraday cup, resulting in a false current reading. The locating pins are used to measure the ion beam current in the wings of each side of the mass resolved peak, thus measuring identical currents if the ion beam is centered between the locating pins. The current from each pin creates an error signal that can be used as a feedback signal to stabilize the power supply of the magnet. Since the sample contains ^{85}Sr as well, the beam intensity of the ^{85}Rb beam can be used to monitor the ion beam current in a non-destructive measurement of the ion source parameters.

Finally, at the entrance of the trapping cell a stainless steel collimator with a 5 mm opening is mounted to measure the ion beam current with a picoammeter. The transmission of the second quadrupole triplet is optimized by minimizing the ion beam current measured at the collimator and maximizing the current and the $^{\circ}$ -count rate at the catcher foil.

3.4.3 Typical Performance of the Ion Source and the Mass Separator

There are several parameter that must be monitored and optimized to achieve a high overall efficiency of the mass separator. Starting at the ion source, one wants a

high vaporization rate as well as a high ionization efficiency of the crucible. We use a collimated NaI γ -detector to monitor the count rate of the activity loaded into the crucible. By monitoring the 776 keV γ -line from the ^{82}Kr ($2^+ \rightarrow 0^+$) excited state decay, we can measure the vaporization rate of the ion source crucible. Figure [3.9] shows the γ -spectrum while the crucible is heated (red curve) and not heated (blue curve), respectively. After the measurement the electron bombardment of the crucible was stopped and the γ -spectrum was recorded after the crucible has cooled down to room temperature. The spectrum shows good agreement with the spectrum taken before the measurement, thus the loss of ^{82}Sr and ^{85}Sr due to vaporization is negligibly small. The comparison of the number of counts in the 776 keV γ -line measures the loss of ^{82}Rb due to vaporization. One finds that 42% of the produced ^{82}Rb atoms leave the ion source crucible.

The ionization efficiency could be measured by monitoring the beam current shortly after the ions leave the ion source crucible. However, the geometry of the ion source and the small distance between the crucible and the extractor makes it very difficult to measure the ion beam current precisely. Hence, we decided to take advantage of the high transmission feature of the mass separator ($\gg 100\%$ as indicated by the ion optical calculations) and simply measure the sum of the transmission of the mass separator and the ionization efficiency of the ion source by measuring the amount of ^{82}Rb implanted onto the catcher foil by monitoring the activity levels of ^{82}Rb at the ion source and simultaneously at the catcher foil. Again, this measurement is done using a collimated NaI γ -counter to observe only the activity deposited onto the catcher foil. The detector is calibrated with a well-characterized $^{82:85}\text{Sr}$ sample, and gates are set to only monitor the counts in the 776

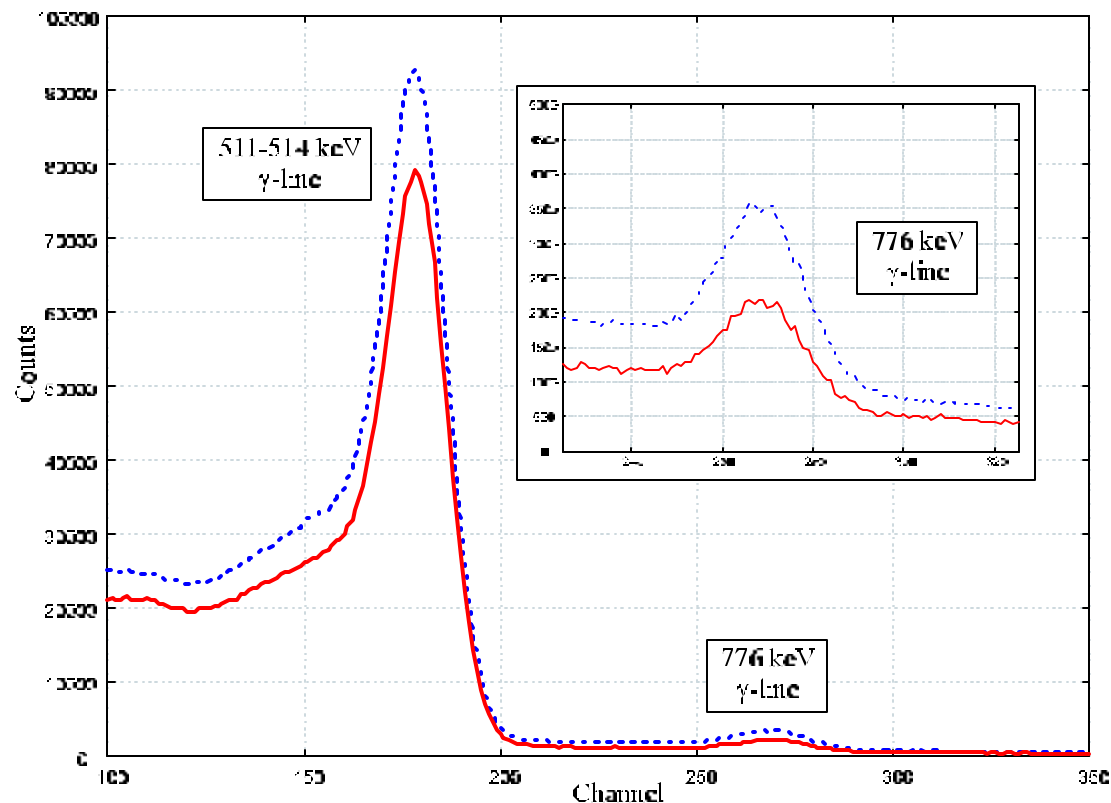


Figure 3.9: The γ -spectrum of a typical $^{82:85}\text{Sr}$ sample within crucible of the ion source. The blue, dotted line shows the spectrum with the crucible at room temperature (the ion source is turned on), while the red plot shows the same sample at a crucible temperature of ≈ 2000 K. Due to the limited energy resolution of the NaI detector the 511 keV from the annihilation radiation overlaps with the 514 keV γ -line from the ^{85}Sr decay. The inset figure shows the magnified 776 keV γ -line, which is used to determine the vaporization rate of the ion source for ^{82}Rb .

keV γ -line that is strictly due to the $^{82}\text{Rb} \rightarrow ^{82}\text{Kr}$ -decay.

The ion source operation is completely computerized which allows for a PID control loop to stabilize the ion source settings. Also, all the high voltage carrying ion optical components as well as the vacuum valves and ion gauges are monitored by the computer. The system is designed to automatically shut down the entire mass separator to avoid possible damage in case of a vacuum leak or power outage.

3.5 Foil Studies

After accumulation of the ^{82}Rb ions in the catcher foil, we must release the implanted ions in form of neutral atoms into the trapping chamber. We are using a resonant LC circuit (shown in Figure [3.10]) to heat the catcher foil to high temperatures. The signal from a 20 MHz frequency generator (a typical drive frequency is ≈ 9 MHz) is fed into a 25 W RF amplifier (EBI Model A 25-25 PA). The RF power inductively couples into the catcher foil which, depending on the foil parameters, can be heated to temperatures of up to 1500 $^{\circ}\text{C}$. The foil temperature is measured with an optical pyrometer (Raytech Thermalert 30,

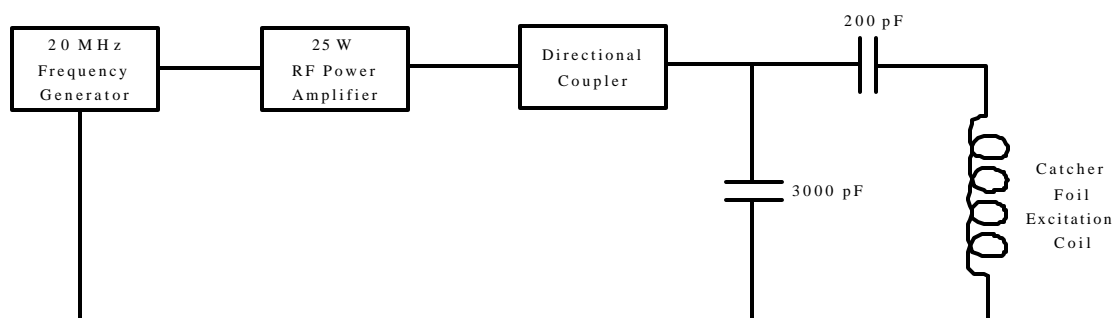


Figure 3.10: The LC resonant circuit for heating of the catcher foil is shown. The directional coupler is used to optimize the drive frequency, thus minimizing the reflected power.

sensor model HTCFI) which has an accuracy of $\pm 1\%$.

Since efficiency considerations are extremely important for the proposed measurements, the release of neutral atoms from the catcher foil into the vacuum chamber of the MOT obviously needs to be optimized as well. One finds only very few publications dealing with the efficient release of neutral particles from a catcher foil. Thus, we decided to use the radioactive ^{82}Rb ion beam from the mass separator to perform a detailed study of the release properties of a variety of possible catcher foil materials. Again, one needs to satisfy a number of constraints. One must

- a) maximize the number of atoms released at low temperature to minimize damage of the dry-film coating nearby;
- b) optimize the inductive heating process by selecting materials with reasonable electrical properties, since the conductance of the material determines the maximal temperature achievable for a given RF power setting;
- c) select a neutralizer material with a work-function below the ionization energy of Rb to release Rb as neutral atoms rather than charged ions;
- d) monitor the outgassing properties of the catcher foil while heated.

We have designed and used a trapping cell (see Figure [3.11]) which is very similar to the trapping cell used in the final setup, but with a modified back-end, to allow quick changes of the different catcher foil materials. A small CsI coated screen could also be inserted in the catcher foil position to verify the ion optical solution of the mass separator. The number of ^{82}Rb ions implanted into the catcher foil is monitored by a collimated NaI

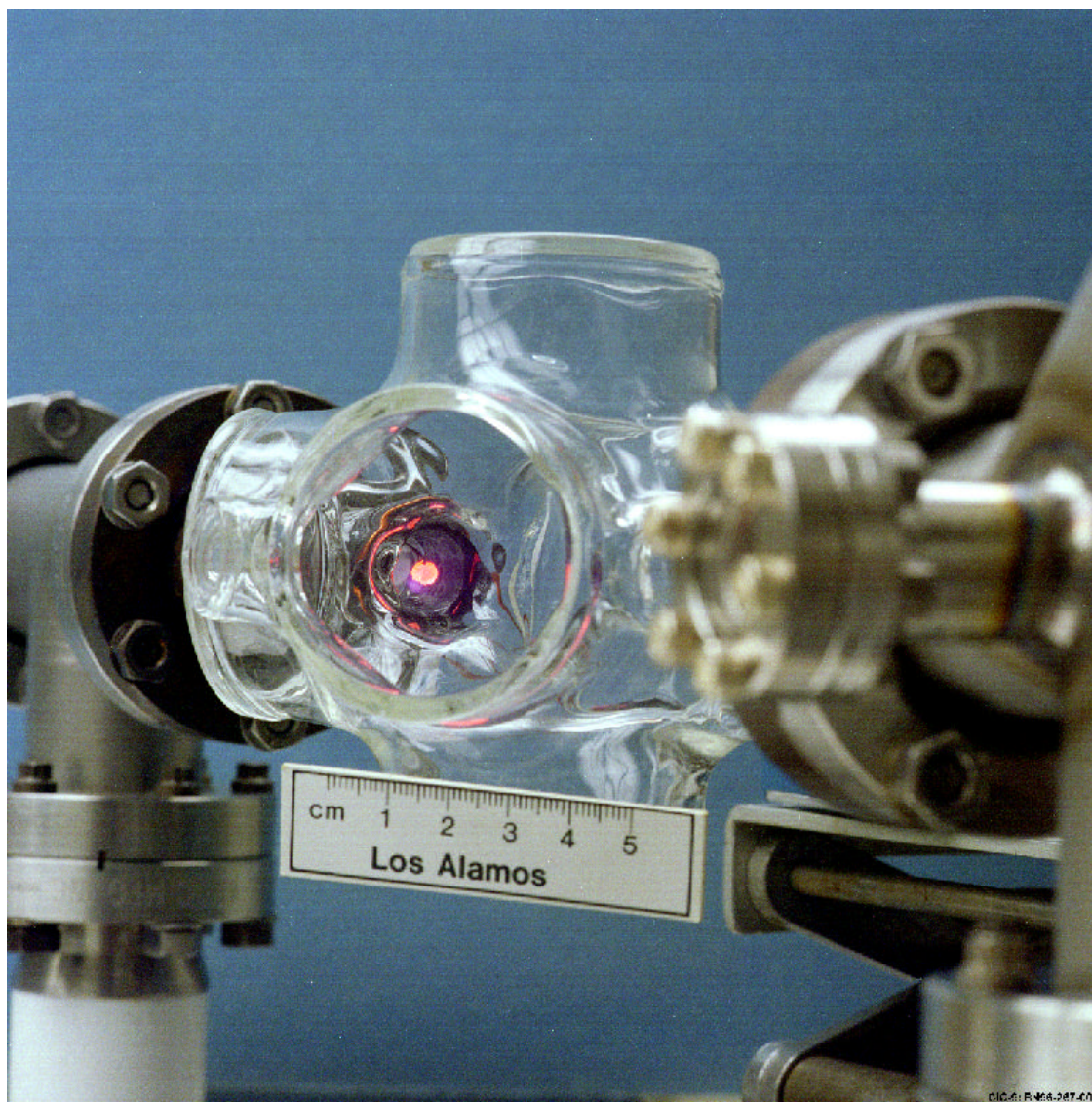


Figure 3.11: The picture shows a glowing Pt catcher foil (6 mm diameter), heated to $\gg 1000$ °C in our test cell. The release from the foil is monitored by a collimated β -counter (not shown) perpendicular to the catcher foil location. This cell features a vacuum port at the back of the cell, thus, various catcher foil materials and thicknesses can be tested without disassembling of the trapping cell.

β -counter. A gate is set around the 776 keV β -line to monitor the number of ^{82}Rb atoms implanted. When heating, some percentage of the activity diffuses off the foil, thus the activity level drops and the release from the foil is measured. In addition, the temperature profile of the foil is recorded with an optical pyrometer, which in combination with the β -decay rate, gives valuable information on the time dependence of the release process. A typical spectrum taken from a multi-channel analyzer (MCA) operated in multi-scaler mode is shown in Figure [3.12].

The different catcher foil materials tested are listed in Table [3.3]². Two candidates require additional explanation. First, we found the best release was obtained with a Mo foil (25 μm thickness), where $\gg 80\%$ of the implanted ions are released at a temperature of $\gg 1500^\circ\text{C}$. Since the work-function (4.2 eV) of Mo is very similar to the ionization energy of Rb (4.1 eV), we needed to measure the fraction of ions released. By applying a negative 300 V suppression voltage to the catcher foil and monitoring the release with and without the suppression voltage, we found that only $\gg 20\%$ of the activity is released with the suppression voltage applied, indicating that most of the activity is released in the form of ions. Secondly, we included Pt in the test series despite its high work-function due to extremely promising release rates published in Reference [101]. Despite several attempts to achieve large release rates at relatively low temperatures (90% at 1200°C) we found only a marginal release at even high temperatures as shown in Table [3.3].

A second feature of the described setup is the possibility to study the time dependence of the release process as a function of catcher foil materials or catcher foil thicknesses.

²A simple model which shows the dependence of the achievable foil temperatures (at a given RF power setting) depending on the foil characteristics can be found in the Appendix.

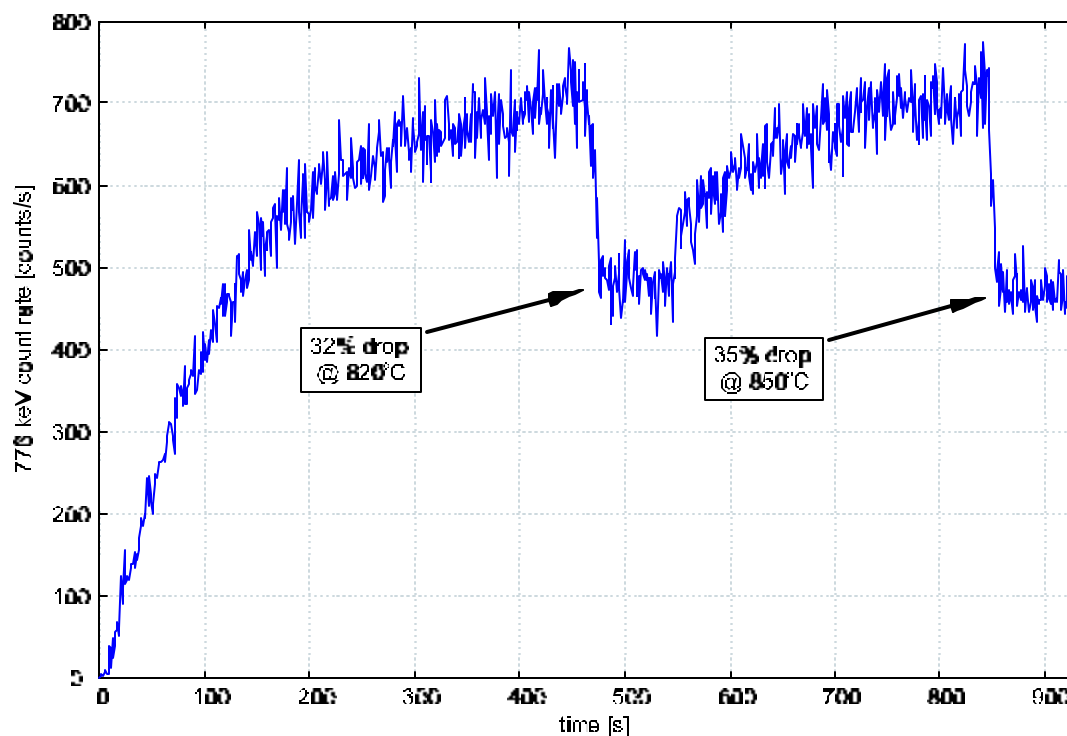


Figure 3.12: The measured release of ^{82}Rb is shown as a function of time. At $t = 0$, the radioactive ion beam is steered onto the catcher foil. The activity accumulates at the catcher foil and the foil is heated to 820°C for about 50s ($t = 475$). The activity level drops and the amount of activity released is determined. The heating of the foil is stopped ($t = 530$ s) and the activity level raises again to its saturation level. A second run at 850°C is started.

We ...nd, e.g. that molybdenum not only has a poor total release rate for neutrals, in addition the diffusion out of the foil takes about 3 times longer than any other foil material studied (and featured measurable release rates) at the same foil thickness.

As a result of our measurements, we decided to use a $25\text{ }\mu\text{m}$ thick yttrium foil with a very reasonable release of $\gg 40\%$ at 1050°C . The work-function of yttrium (3.1 eV) is much lower than the ...rst ionization potential of Rb, thus minimizing the release of significant number of ions. We have measured the release with and without the suppression voltage applied to the catcher foil and ...nd no detectable differences in the release rates

from the yttrium foil.

However, when heating some of the foils, especially with yttrium, we find a large temperature gradient across the foil. Since the diffusion process shows a strong temperature dependence, one likes a uniformly heated foil to minimize the sensitivity where the ions are implanted in the catcher foil. The effect is easily understood when analyzing the inductive heating process. Inductive heating mostly heats the outer area of the catcher foil. Since the thermal conductivity of some of the elements is very poor, the heat is not conducted to the center of the foil. When spot-welding the yttrium foil onto a tungsten backing, however, due to the excellent heat conductance properties of tungsten the large temperature gradient typical for the yttrium foil completely vanishes, leaving a uniformly heated catcher foil. In addition, when heating the "sandwich" catcher foil to temperatures approaching 1000 °C, the yttrium foil suddenly melts onto the tungsten foil, eliminating any gaps between the yttrium and the tungsten foil.

Another advantage when using a Y catcher foil, as mentioned earlier is the very low temperature of the foil required to release significant number of Rb atoms (35% at 850 °C). A low temperature of the catcher foil is desirable, since:

1. A catcher foil at very high temperature carries the potential of damaging the dry film coating nearby; and
2. the vapor pressure and the outgassing rate of the catcher foil will ultimately increase the pressure in the trapping cell, thus limiting the lifetime of the atoms in the trap.

Both effects will lead to a substantially lower trapping efficiency of the MOT and therefore, a smaller number of atoms is trapped.

Characteristics of the Investigated Catcher Foil Materials

Element	Resistivity	Work-Function	Melting Point	Boiling Point	Thermal Conductivity	Thermal Expansion	Temperature required for $1:0 \pm 10^{-6}$ Torr
	[$\Omega \cdot \text{cm}$]	[eV]	[$^{\circ}\text{C}$]	[$^{\circ}\text{C}$]	[W/mK]	[$10^{-6}/\text{K}$]	[$^{\circ}\text{C}$]
Y	53	3.1	1552	3338	17.2	10.8	1100
Hf	32.2	3.9	2227	4602	23	6	1730
Ta	13.5	4.1	2996	5425	57.5	6.5	2220
Mo	5.7	4.2	2617	4612	138	5.1	1850
W	5.4	4.55	3410	5660	173	4.5	2380
Pt	10.58	5.3	1772	3827	71.6	4.8	1465

Foil Material	Foil Thickness	Input Voltage	Reflected Power	Max. Temp.	Uniformity: Dark Spot size / Center Temp.	Total Release	Fraction released as Neutrals
	[μm]	[mV]	[%]	[$^{\circ}\text{C}$]		[%]	[%]
Y	25	700	13	1040	2 mm / 900 $^{\circ}\text{C}$	40	100
Hf	25	700	17	1100	2 mm / 900 $^{\circ}\text{C}$	0	N/A
Ta	25	700	12.4	1231	N/A	33	50
Mo	25	1000	14	1380	N/A	80	20
Pt	12.5	500	14	1520	N/A	17	0

Table 3.3: Important foil properties are listed in the upper table [102, 90]. Note: Tungsten is included since we use a tungsten backing to reduce the temperature gradient characteristic for the yttrium and hafnium foils. The lower table gives measured release rates for different catcher foil materials. Also, the fractional release of neutrals relative to the total release is listed. Note: The maximal input voltage for the RF amplifier is 1200 mV (corresponds to a RF output power of 25 W).

Chapter 4

A Laser Trap for Radioactive Atoms

The daunting task of trapping radioactive atoms for use in a high-precision electroweak interaction measurement requires the optimization of a large variety of parameters in every stage of the experiment. As outlined in the last chapter, the optimization of the ion source and the mass separator for high efficiency are essential for the successful introduction of the radioactive ions into the vacuum chamber of the MOT. In turn, the MOT itself needs to be optimized to trap as many atoms as possible. Here, I will present the work that has been done in our lab to optimize the capture efficiency of the MOT and introduce a “second generation” MOT that is coupled to a mass separator for the efficient trapping of radioactive atoms.

4.1 The MOT

The MOT traps atoms with a velocity smaller than the capture velocity, which only involves a very small fraction of the atoms at the end of the Boltzmann distribution. Typical numbers for the capture velocity v_c and the average velocity of room temperature atoms \bar{v} are $v_c = 20\text{m/s}$ and $\bar{v} = 500\text{m/s}$ for Rb, respectively. There are two possible improvements that can be made when designing a more efficient version of the MOT:

- a) maximize the capture velocity of the MOT, hence maximizing the number of atoms trapped from the Boltzmann distribution in a single wall to wall passage, and
- b) enable each individual atom to have multiple collisions or “bounces” with the walls of the vacuum chamber, so that the atom can re-thermalize on each bounce and has multiple chances to be trapped.

Following the pioneering work of Stephens et al. [103, 104], we addressed the issue of trapping efficiency by carefully investigating the different trapping parameters and their impact on the trapping efficiency. A separate MOT laser setup was put together to investigate these trapping efficiency problems while the upgrade of the mass separator was performed. We found that by optimizing the cell design we were able to reach considerably higher trapping efficiencies. The measurements on the trapping efficiency are done using stable ^{133}Cs atoms. Due to additional losses characteristic for radioactives, the results obtained represent general guidelines but do not describe the trapping of radioactives entirely.

4.2 Trapping Efficiency Considerations

Early experiments with MOT's show that the number of trapped atoms at a constant laser beam intensity follows the relationship $N \propto L^{3/6}$, with L being the laser beam diameter [105]. Large laser beams lead to a larger capture velocity for the MOT, and consequently trap a larger percentage of the atoms in the Boltzmann distribution to increase the efficiency of the trapping process. It is been shown [103] that the steady state number of trapped atoms is given by,

$$N = R_{\text{trap}} = 0.1 \frac{A}{\sigma} \frac{\bar{v}_c}{\bar{v}_{\text{th}}}^4; \quad (4.1)$$

where R is the capture rate and $1/\tau_{\text{trap}} = n_0 \sigma \bar{v}_{\text{rms}}$ is the loss rate due to collisions between trapped atoms and atoms in the room-temperature alkali background gas. The cross section σ for these collisions has been measured to be $\approx 2 \times 10^{-13} \text{ cm}^2$ for Cs, $n_0 = 10^8 / \text{cm}^3$ is a typical density of the background gas at a pressure of $\approx 10^{-8} \text{ torr}$, and $\bar{v}_{\text{rms}} = 236 \text{ m/s}$ is the root-mean-square velocity at room temperature. The capture rate involves the surface area A of the trapping volume, and the ratio between the capture velocity \bar{v}_c and the average velocity of the background gas $\bar{v}_{\text{th}} = 193 \text{ m/s}$ for Cs at room temperature.

Equation [4.1] shows that, to calculate the number of trapped atoms, we need to know the surface area of the trapping volume A and the capture velocity \bar{v}_c . Since a 3-D model of the MOT is yet to be developed, which would predict the capture velocity and the number of trapped atoms, we use the one-dimensional expression of the radiation pressure force to estimate the capture velocity. Using equation (2.19) and taking into account that the force for an atom is proportional to the difference between the number of photons scattered from the two counterpropagating laser beams along the axis, we find the following

Laser properties	Contribution to capture rate R
Beam diameter L	$R \gg L^{3/6}$ constant intensity, large L $R \gg L$ constant power, large L
Beam intensity I	$R \gg I$ constant power, large L (saturates at high I)

Table 4.1: Dependence of capture rate on trap parameter (Taken from [105])

expression for the scattering force

$$F_{\text{scatt}} = \frac{2}{3} k \frac{I}{I + I_s} \frac{1}{1 + 4 \frac{\Delta^2}{\Gamma^2} + \frac{k^2 A^2}{2\Gamma^2}} \quad (4.2)$$

where $\Delta = \omega_{\text{laser}} - \omega_{\text{atom}}$ is the detuning of the laser, Γ is the natural linewidth of the transition, I_s is the saturation intensity of the transition, and I is the laser intensity. The capture velocity is obtained by solving equation (4.2) numerically under the assumption that an atom is trapped when its velocity is less than 10 cm/s when the atom has passed the trapping region.

While this simple model neglects the magnetic field necessary to create the position dependent force that forms the MOT and, in addition, treats the atom only as a simple two-level system, Lindquist et al. [105] showed that the number of trapped atoms predicted by the model is low by a factor of 3, but describes the general trends (Table 4.1) remarkably well.

The situation in a vapor-cell trap for radioactives is somewhat different. When trapping stable atoms, one is not sensitive to losses from the trap due to chemical reactions of the alkali vapor with the wall or the sticking of the alkali atoms to the wall, since the dilute vapor is constantly replenished by the reservoir. In an experiment that involves only a fixed number of atoms suddenly introduced into the vapor-cell all those losses become important. Therefore, we must construct a vapor-cell using a material which minimizes the

interaction with the alkali vapor and is compatible with the ultra-high vacuum environment present in a MOT.

Again, Stephens et al. [103] have simulated the sudden introduction of N_0 atoms into a vapor-cell and trapping as many as possible. They found that this situation can be described by

$$\frac{dN}{dt} = R(t) - \frac{N}{\tau(t)} ; \quad (4.3)$$

where N is the number of trapped atoms. The capture rate R is given by

$$R(t) = \frac{1}{4} \frac{\bar{A}_c^4}{\bar{A}_{th}^3} L^2 n(t) ; \quad (4.4)$$

where \bar{A}_{th} is the thermal velocity and n equals the density of untrapped atoms, while \bar{A}_c is the capture velocity of the MOT and L is the laser beam diameter. The untrapped vapor density now depends on the chemical reaction rate of the alkali atoms and the wall;

$$n(t) = \frac{N_0 - N(t)}{V} \frac{e^{-\frac{rA}{\zeta_s \bar{A}_{th} A=4V} t}}{1 + (\zeta_s \bar{A}_{th} A=4V)} ; \quad (4.5)$$

where A/V are the surface area and the volume, respectively, of the trapping cell, r is the effective pumping speed of the wall per cm^2 caused by permanent chemical reactions between the atoms and the wall, and ζ_s is the average sticking time of an atom on the wall.

The loss rate of the trap depends on the pressure P in the vapor-cell (in torr);

$$\frac{1}{\tau} = 3.3 \times 10^{16} P^{3/4} \bar{A}_b ; \quad (4.6)$$

where σ_b is the cross section for collisions between the non alkali background gas and an atom in the trap, and \bar{A}_b is the thermal velocity of the background gas. By measuring the pressure of the background gas and the loss rate of the trap, one determines $\sigma_b \bar{A}_b \gg 10^{-9} \text{cm}^3 = \text{sec}$,

where the collisional loss due to collision with the alkali background is neglected, since the density of the alkali atoms is a factor of 10-100 lower than the density of the background gas. The non-alkali pressure initially is given by

$$P_0 = \frac{QA}{S} ; \quad (4.7)$$

where S is the pumping speed at the cell and Q is the outgassing rate of the walls. If the vapor-cell is closed off after the sample is introduced, the pressure rises linearly with time;

$$P = P_0 + \frac{QA}{V}t : \quad (4.8)$$

The collection efficiency can be calculated by solving equation (4.3)-(4.6) for the number of trapped atoms as a function of time. The maximum collection efficiency is the maximum number of trapped atoms, divided by the initial number of atoms released into the vapor-cell.

One finds the following requirements for materials that can be used to improve the collection efficiency of the MOT. The sticking time of alkali atoms ζ_s has to be short to allow multiple bounces in the trap (e.g. $\zeta_s \ll 50 \mu\text{s}$). The reaction rate r of the atom with the coating has to be small and the outgassing rate of the coating material needs to be low (e.g. $r \ll 0.1 \text{ cm}^3/\text{s cm}^2$, and $Q \ll 10^{-8} \text{ Torr cm}^3/\text{s cm}^2$). Table [4.2] shows the results found by Stephens et al. [104] for a variety of organic coating materials used for Pyrex or quartz vapor-cells.

4.2.1 A MOT for the Study of Trapping Efficiency

The geometry of the vapor-cell is important for the efficient trapping from a limited supply of atoms. A large laser beam diameter increases the capture velocity of the trap,

Surface	Reaction rate r $\text{cm}^3/\text{s cm}^2$	Outgassing Q $\text{Torr cm}^3/\text{s cm}^2$	Sticking time τ_s (^1s)
Pyrex	0.03	$<10 \cdot 10^{-8}$	1400
SC-77	0.025	$2 \cdot 10^{-7}$	<35
OTS	0.086	$2.2 \cdot 10^{-8}$	<35

Table 4.2: Outgassing and reaction rates for dry...Im coatings. Taken from Ref. [104]

hence tapping a larger fraction of atoms from the Boltzmann distribution. On the other hand, the laser power obtained from available lasers limits the beam size of the trapping laser. The Zeeman splitting caused by the magnetic ...eld necessary to obtain a MOT, eventually shifts the atomic transitions too much, which ultimately leads to “heating” effects due to the excitation of anti-trapping transitions (the shift of the transition due to magnetic ...eld is roughly 1 MHz per Gauss). Nevertheless, careful optimization of the geometry of the trapping cell can lead to a significant gain in the achievable trapping efficiency.

In summary, when optimizing the trapping cell geometry, the goal has to be to maximize the illuminated region of the trapping cell and therefore minimizing the amount of “dead space” in the trap. In an ideal configuration, the laser beams completely illuminate the trapping cell, which eliminates all of the dead space and greatly improves the trapping efficiency. The ...rst geometrical object one could imagine is a glass sphere exactly the size of the laser beams. Unfortunately the curved glass surfaces would cause focussing effects of the laser beams, thus destroying the trap. One ...nds the second best geometry in a cube, completely illuminated by the laser beams.

We have built a MOT using a 5 cm Pyrex cube mounted directly to a Varian StarCell 20 l/s ion pump (see Figure [4.1]) which maximizes the pump-out speed of the system. The goal was to carefully investigate the impact of laser intensity, detuning, and

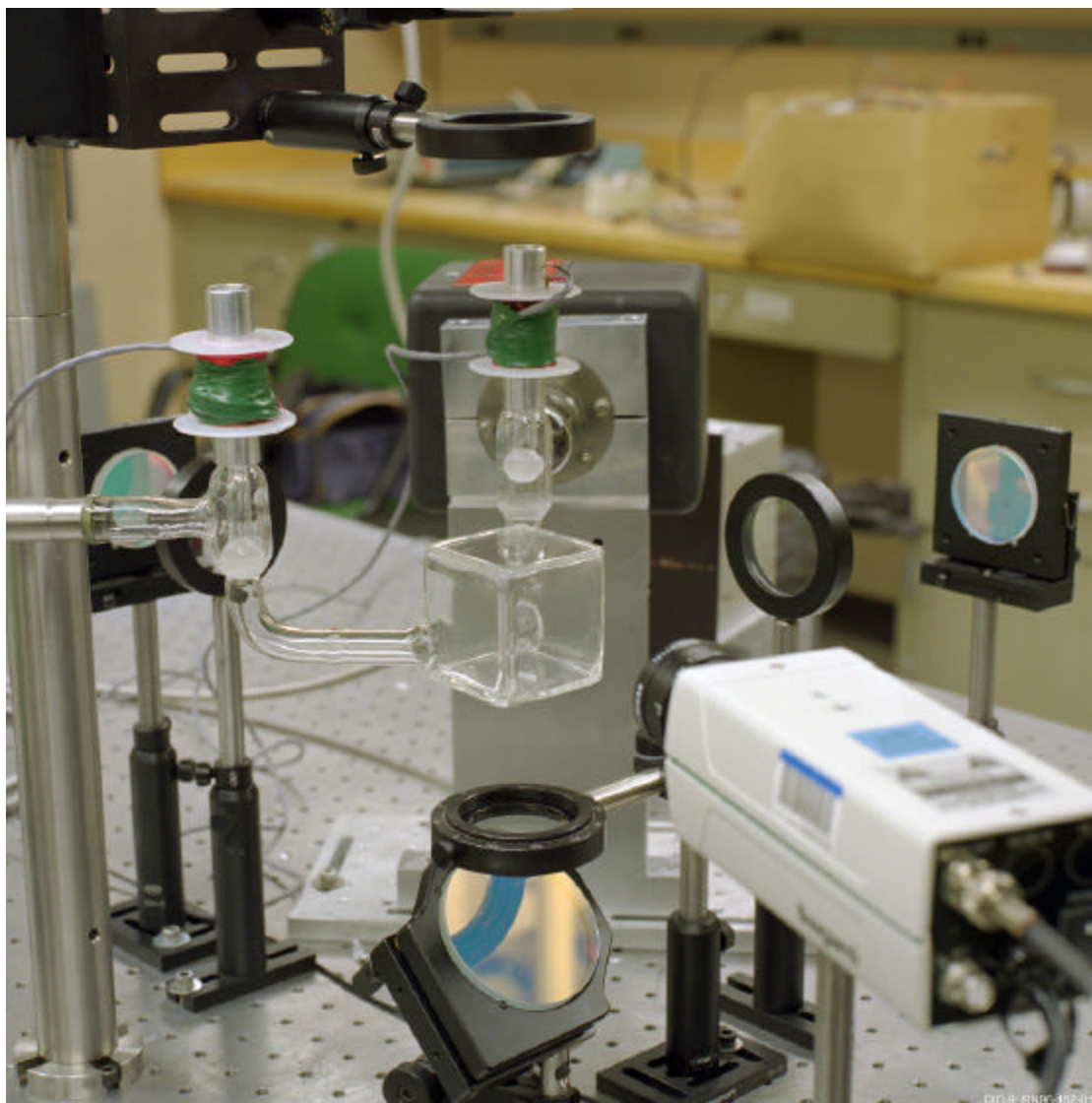


Figure 4.1: The vapor cell used in the efficiency measurement is shown. Clearly visible are the two glass valves attached to the trapping cell. The valve is made of ground glass providing a reasonably small leak rate. All the glass surfaces, including the valves, are coated with OTS. The glass valve to the left leads to the Cs reservoir while the one on the right is mounted directly onto a Varian StarCell ion pump with a pumping speed of 20 l/s. This configuration minimizes the pump out time of the trapping cell since only a small portion of the surface area is left uncoated. The quadrupole coils of the MOT are normally mounted above and below the Pyrex cube but are removed in this picture.

magnetic field gradient on the number of atoms trapped. These measurements also led to a robust system which allows the careful investigation of the efficiency of the trapping process. In our setup, due to the size of the optics (50 mm dia.) available, we chose not to shrink the cell any further, hence leaving some of the volume of the cube dark.

The MOT described here utilizes laser light from a Coherent 899-21 Ti:Sapphire (Ti:Sa) ring laser, pumped by a Coherent Innova 200 argon ion laser. The Ti:Sa produced up to 1.5 Watts of single frequency laser light at 850 nm to be used for trapping purposes (I will refer to this laser arrangement as “high-intensity setup”). The laser beam from the Ti:Sa is combined with a second laser beam extracted from a SDL-5101 100mW diode laser. The home-made external cavity system, first described in Reference [106], uses feedback from a diffraction grating to provide a narrow-band, continuously tunable light source with a usable output power of $\gg 35$ mW.

While the Ti:Sa laser beam is tuned to the $6S_{1/2}; F = 4 \rightarrow 6P_{3/2}; F^0 = 5$ trapping transition in Cs, the light from the laser diode is tuned to the $6S_{1/2}; F = 3 \rightarrow 6P_{3/2}; F^0 = 4$ state in order to repump atoms that accidentally fall into the $6S_{1/2}; F = 3$ “dark” state (see Figure [4.2]). The combined laser beam is split into three laser beams with equal intensities and expanded to the desired beam size. This setup has become the “standard” configuration for MOT’s and has the potential to trap as many as $\gg 4 \times 10^{10}$ atoms from the vapor. The number of trapped atoms in this setup is limited since the optically thick cloud of atoms causes intensity imbalance in the incoming and retroreflected laser beams, thus disturbing the MOT configuration. Since the scope of this work was to determine the capture efficiency of the trap rather than trapping as many atoms as possible, this limitation

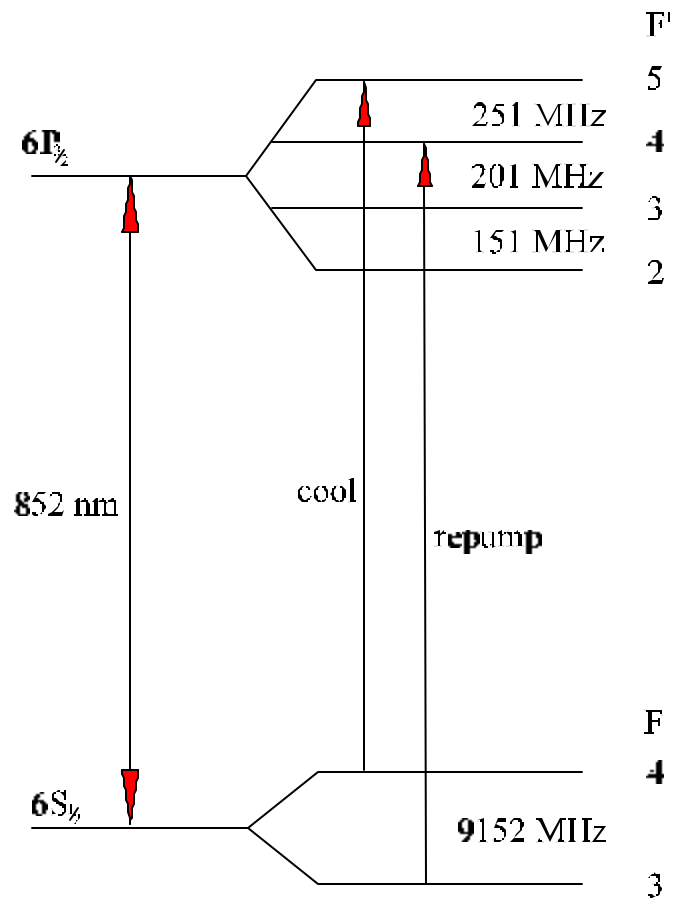


Figure 4.2: The relevant transitions for cooling and trapping in ^{133}Cs are shown. The trapping laser is tuned to the $6S_{1/2}; F = 4 \rightarrow 6P_{3/2}; F' = 5$ transition. The repump laser is tuned to the $6S_{1/2}; F = 3 \rightarrow 6P_{3/2}; F' = 4$ transition to optically pump atoms back into the $6S_{1/2}; F = 4$ state.

of the described setup can be neglected. A beautiful color infrared picture of a large cloud of Cs atoms ($\gg 4 \times 10^{10}$) with a size of 1.5 cm (horizontally) and 1 cm (vertically) is shown in Figure [4.3]. Results using the “high-intensity” setup are shown in Figure [4.4] and are in very good agreement with similar measurements reported in Reference [107].

Following our basic measurements on the number of trapped atoms, we started the investigation of the trapping efficiency of the MOT using the described trap geometry.

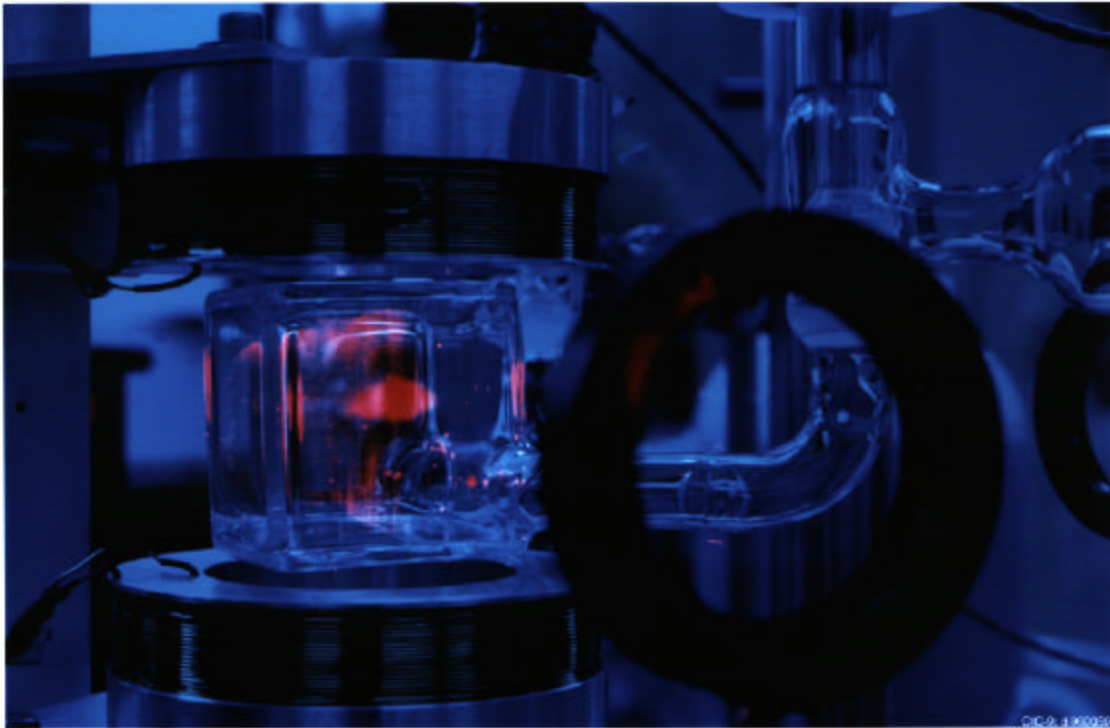


Figure 4.3: A color infrared picture of the Cs trap is shown. The cloud is compressed vertically, since the axial magnetic field gradient is twice as strong compared to the radial direction, resulting in a “pancake” shaped cloud.

When using a constant density of alkali atoms in the background gas the number of trapped atoms does not depend on the chosen geometry. However, in case of a limited number of atoms available in the vacuum chamber, the overall trapping efficiency depends on the ratio of surface area of the trapping cell, the volume of the trapping cell, and the laser beam diameter as described by equation (4.4). As a result of the chosen trapping cell geometry and the available laser power, we were able to improve the trapping efficiency from 6% reported in [103] to $\gg 20\%$ in our trapping cell. A description of the trapping efficiency measurement is given below.

The experimental setup for the efficiency measurement is shown in Figure [4.1]. A

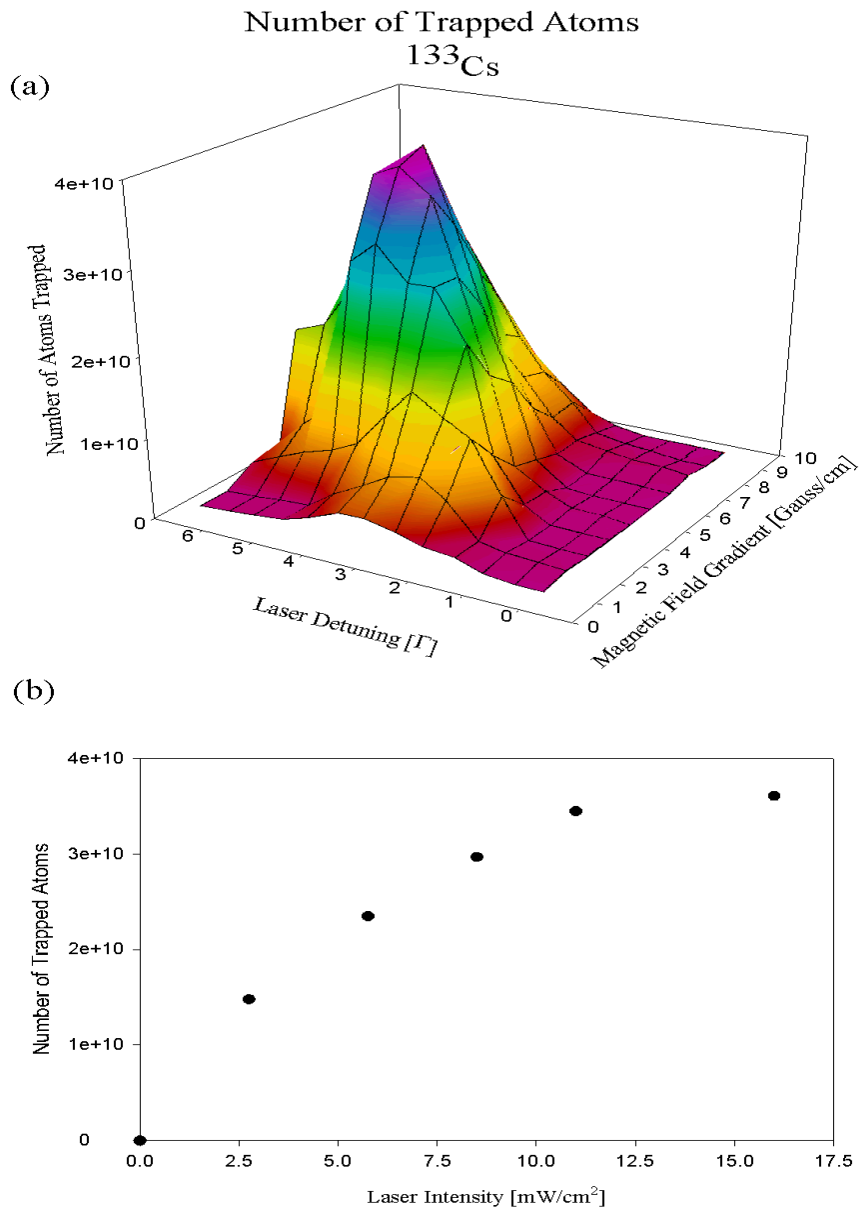


Figure 4.4: Results obtained with the “high-intensity” MOT. Detailed studies of the number of trapped atoms as a function of laser detuning and magnetic field gradient (a) and the intensity (b) are shown for a fixed laser beam diameter ($1/e^2 = 6$ cm). The maximum is found at a detuning of 4Γ ; and a magnetic field gradient of 6 Gauss/cm. We investigated three different laser beam diameters and the results, $\approx 3.6 \times 10^{10}$ trapped atoms, with a laser beam diameter of $1/e^2 = 6$ cm proved to be the best.

5 cm Pyrex cube with two ground glass valves, which allows the sudden introduction of Cs vapor into the trapping cell, is coated with octadecyltrichlorosilane (OTS) dry...lm following a recipe described in Reference [104]. After careful cleaning (a typical cleaning procedure has been published in [104]), the cell is coated and baked under high vacuum conditions to remove any remaining contaminants at 200 °C for 24 hours. After the bake-out, the cell is installed and laser beams with a usable diameter of 5 cm and a $1/e^2$ diameter of 6 cm form the MOT. The MOT itself is used to trap a known number of atoms (by monitoring the fluorescence of the trapped atom cloud) which are introduced when the measurement is started.

To measure the trapping efficiency we first close the glass valve to the Cs reservoir and open the valve to the ion pump while monitoring the fluorescence signal. After the remaining Cs vapor in the trapping cell has been pumped away, we open the valve to the Cs reservoir for 5 s. The trap fills and reaches saturation. After the valve to the Cs reservoir is closed, the number of trapped atoms decreases due to constant loss from the trap caused by collisions with the background gas. The pump-out time for untrapped Cs atoms is determined to be $\gg 300$ ms, thus opening the valve to the ion pump for 2 s removes most of the untrapped Cs atoms left in the vapor. Approximately two seconds later, the valve to the ion pump closes, the laser beams are blocked and the atoms fall under gravity and rethermalize when they hit the trapping cell surface. After re-thermalization (500 ms later), the shutter is opened and the atoms are re-trapped. The number of trapped atoms is recorded as a function of time using a calibrated photodiode.

We determine the background signal, caused by untrapped Cs vapor, by repeat-

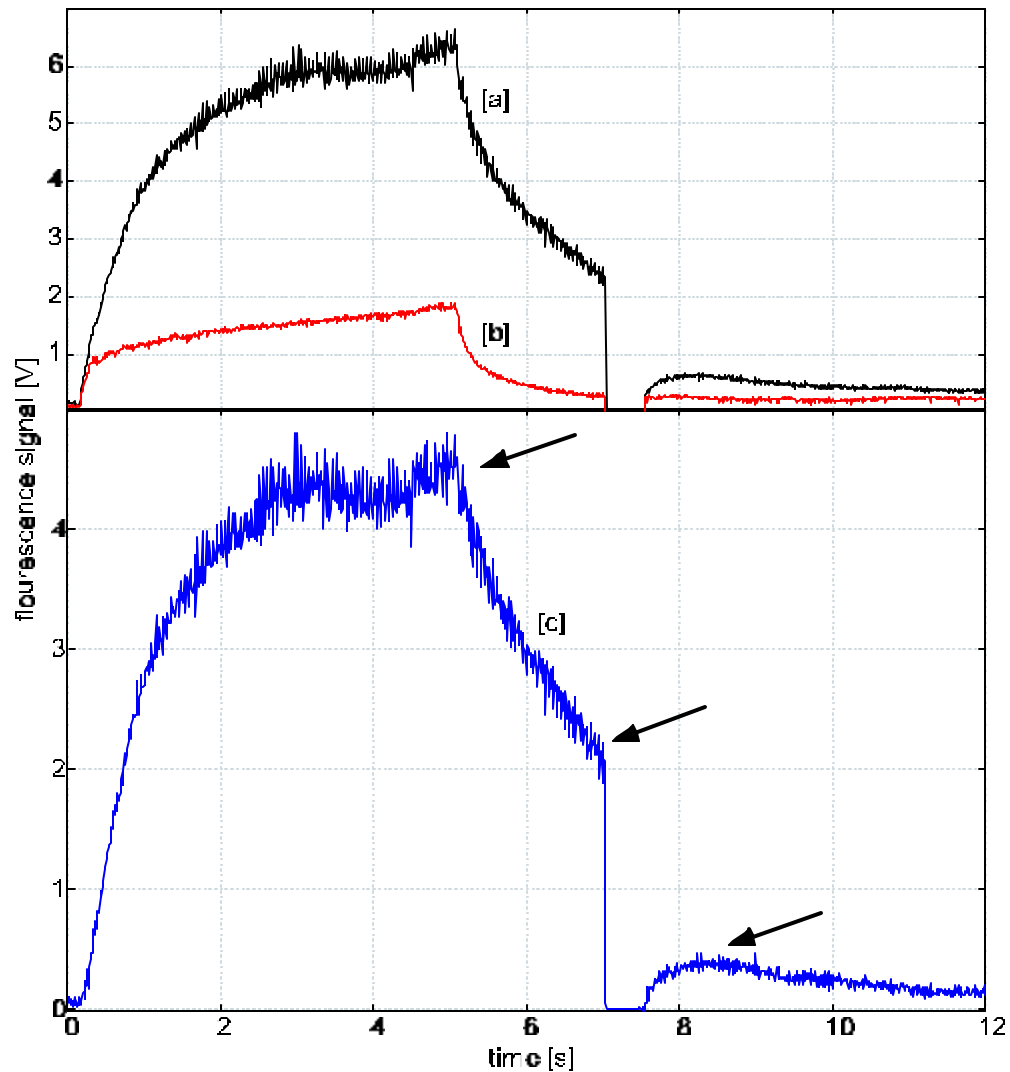


Figure 4.5: The trapping signal is shown as a function of time. [a] Trapping configuration (fluorescence from trapped atoms plus untrapped atoms in the vapor); [b] Anti-trapping configuration (fluorescence only from untrapped Cs atoms in the vapor); [c] Net trapping signal background ([b] is subtracted from [a]). Note the different time constants in [a] and [b]. Untrapped atoms are pumped away quickly, a strong indication for a high quality dry-film coating. At $t = 0$, the glass valve to the Cs reservoir is opened, Cs atoms start to fill the trap. At $t = 5$ s the valve to the Cs reservoir is closed, atoms are lost from the trap and leave the trapping cell since the valve to the ion pump is still open. The valve to the ion pump is closed ($t = 7$ s) and the laser is shuttered off for 500 ms to allow the atoms to hit the surface of the vapor cell and rethermalize. Atoms are then retrapped ($t \approx 7.5$ s).

ing the measurement but reversing the magnetic field up to the point where the lasers are blocked ($t = 7$ s), which measures the fluorescence of the Cs vapor in the trapping cell. The background measurement shows that the pump-out time for the Cs vapor is short ($\tau = 300$ ms) compared to the lifetime of the trap ($\gg 2.5$ s). The time sequence of the measurement is appropriately adjusted to remove as much of the untrapped vapor as possible. As a second check, the magnetic field is switched back into “trapping configuration” when the laser beams are blocked, to determine the trap signal due to Cs atoms being trapped from the remaining vapor in the cell after the lasers are unblocked. The background measurements show that the fraction of the trapping signal caused by Cs background gas is sufficiently small. To eliminate the background from the trapping signal, the background measurement is subtracted from the trapping measurement and the ratio between the number of trapped atoms (at $t = 7.5$ s) and the number of re-trapped atoms determines the trapping efficiency.

A typical measurement is shown in Figure [4.5], with a re-trapping efficiency of $\gg 20\%$. We notice, that the number of re-trapped atoms peaks after $\gg 800$ ms and decreases afterwards. This behavior is in perfect agreement with the model (equation 4.8), and explained by a linearly increasing pressure in the vapor cell after the valve to the ion pump is closed. The loss rate from the trap is pressure dependent and causes the number of atoms in the trap to decrease with time.

Encouraged by the high trapping efficiency measured in the described setup, we used this knowledge to design a new trapping cell to be coupled to the mass separator. Two basic configurations seemed feasible.

1. Radioactive ions are neutralized before they enter the trapping cell, which requires a hot neutralizer surface close to the entrance of the trapping cell. After neutralized, the atoms spray into the dry...lm coated trapping cell, where a MOT captures the atoms. This con...guration has been used successfully at TRINAT to trap ^{38m}K and ^{37}K [21] and at Stony Brook for ^{79}Rb and ^{210}Fr [20].
2. The ion beam is implanted into a catcher foil mounted inside the MOT vacuum chamber. Atoms are released upon heating of the catcher foil and trapped by the MOT.

The advantage of the second con...guration is the more e¢cient introduction process of the radioactive species into the vacuum chamber of the MOT, while the presence of the hot catcher foil itself mounted internal to the trapping cell seems disadvantageous. Nevertheless, the realization of such a con...guration has proven to dramatically improve the overall e¢ciency and is described in the next section of this thesis.

4.3 The Coupling of a MOT and a Mass Separator

The mass separator design used in the experiment is described in detail in Chapter 3. Briefly, a thermal ion source provides the radioactive ion beam, while the separator delivers the ions e¢ciently to the catcher foil. While the α -line setup described earlier featured glass valves to contain the atoms within the cell, a trapping cell coupled to the mass separator obviously needs an entrance hole for the ion beam, thus leaving an opening for the atoms to escape after released from the catcher foil. Hence, the ratio between the surface area of the trapping cell and the surface area of the entrance/exit hole and

the catcher foil sets a limit on the number of bounces the atom takes before being lost. Therefore, a large trapping cell with small openings is preferable.

In the case of an external neutralizer configuration, the use of a small entrance opening would lead to a very small number of atoms entering the cell, resulting in a very low overall trapping efficiency. In the case of an internal catcher foil, the ion beam can easily be focussed, thus minimizing the number of ions being lost when the ion beam enters the cell. The main task in an internal neutralizer setup is to efficiently release neutral atoms without damaging the non-stick dry-film coating of the trapping cell. Secondly, due to the necessity of an entrance and an exit opening, a larger trapping cell is desirable. Fortunately, the conversion efficiency of the Ti:Sa crystal peaks at 780 nm, thus more output power from the Ti:Sa is available at this frequency. We routinely achieve output powers of $\gg 2.5$ W at 780 nm. As a result the use of a 80 mm trapping cell with 5 mm entrance and exit holes was constructed.

As mentioned before, the geometry of the trapping cell sets a limit on the average number of wall bounces. The cell used in our setup features an average of 600 collisions of the atoms with the surfaces of the trapping cell in the case of an ideal coating and it also has a large single pass trapping efficiency due to the large diameter of the laser beams. A schematic of the trapping cell used in our setup is shown in Figure [4.6].

4.4 The Laser Setup

The laser setup of the efficiency measurement was very similar to the setup used to trap radioactive atoms. A schematic of the laser setup is shown in Figure [4.7]. We will

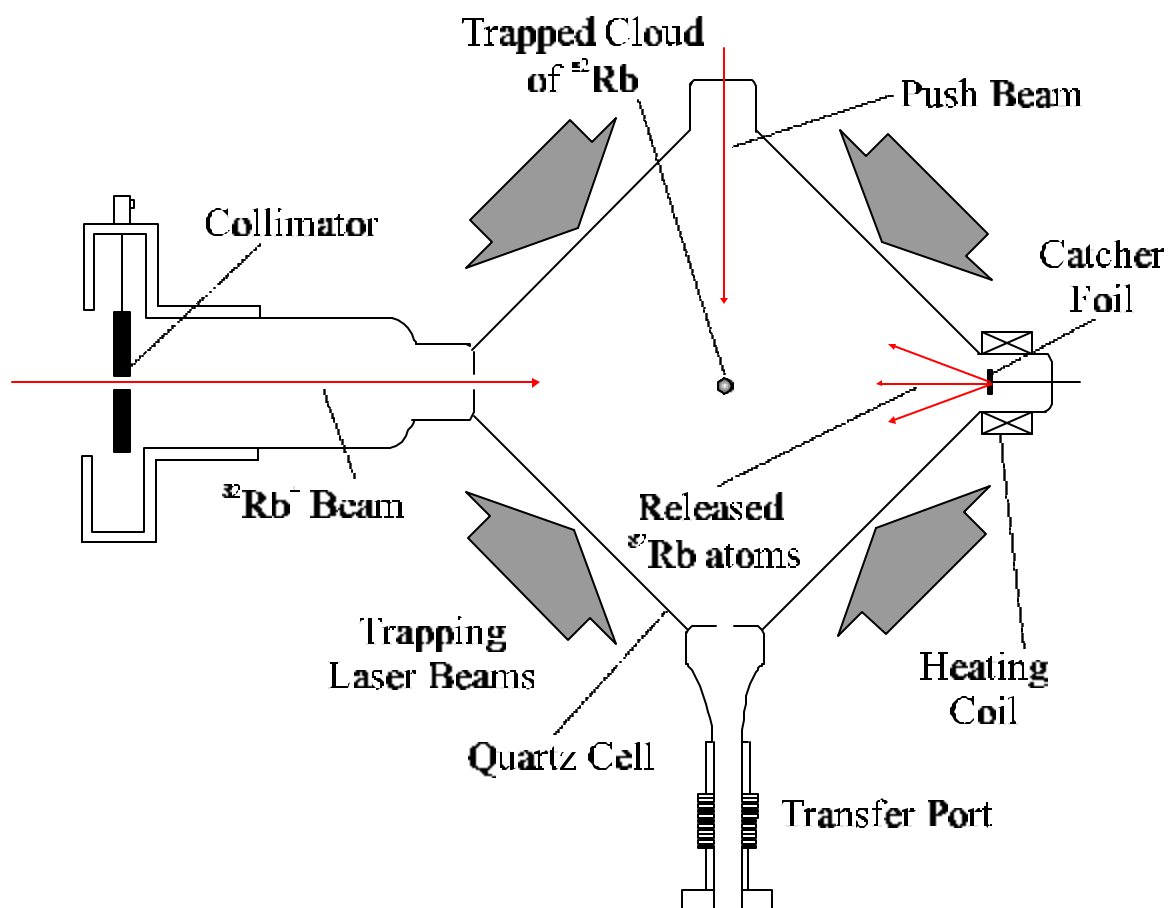


Figure 4.6: A schematic view of the trapping cell is shown. The ion beam enters through the collimator and the 5 mm entrance opening, passes through the trapping cell and hits the 5 mm catcher foil. Upon heating, the atoms are released into the cell and captured by the trapping laser beams. A push beam kicks the atoms through the transfer port into a second MOT where the π -asymmetry measurement is performed.

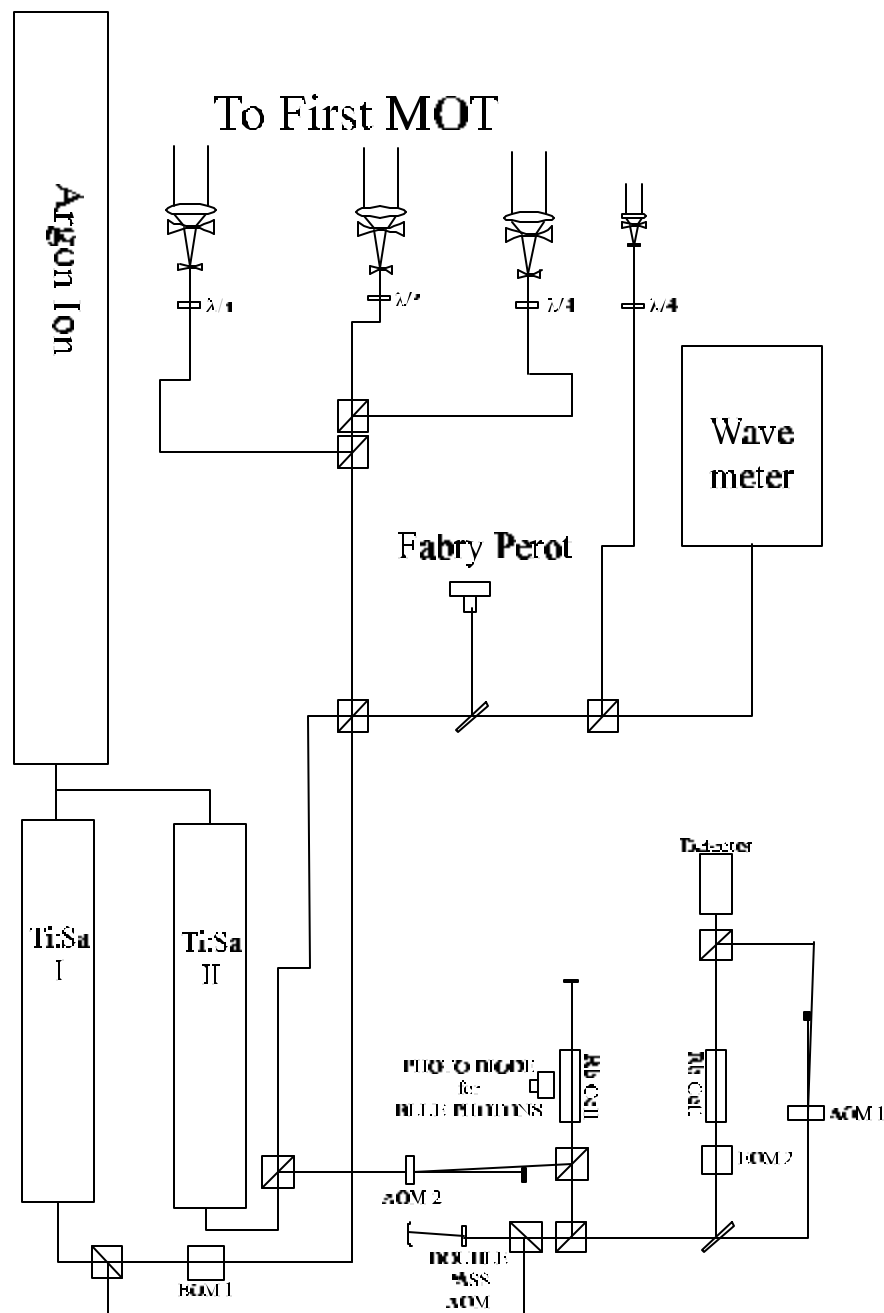


Figure 4.7: The layout of the laser table is shown. An argon-ion laser pumps two Ti:Sa lasers, one used for trapping, while the other is used for ultra-sensitive detection purposes. Both lasers are frequency stabilized by locking them to the relevant atomic transitions in ^{85}Rb using saturated absorption.

focus now on the changes necessary to trap radioactives. A argon ion laser (Coherent Sabre) is used to pump two Ti:Sa lasers, the first one delivering the intense, single frequency laser beam that is used to perform the trapping experiment, while the second Ti:Sa, operated in low power configuration, provides an independent probe beam for ultra-sensitive detection purposes.

It has proven to be very advantageous to have a second Ti:Sa available, especially when searching for the trapping signal of the ^{82}Rb atoms. Uncertain about the size of the expected trapping signal, we tried a setup of different detection schemes, ranging from simple fluorescence detection to the more sensitive phase-sensitive detection scheme, and finally photon counting.

The trapping laser is tuned to the D_2 line of Rb at 780 nm and locked to the peak of the $5S_{1/2}; F = 3 \rightarrow 5P_{3/2}; F^0 = 3; 4$ cross-over transition of ^{85}Rb using a saturated absorption method [106]. In detail, we compensate for the isotope shift between ^{82}Rb and ^{85}Rb (see Figure [5.1]) with a double-pass acoustic optical modulator (AOM) driven at 268 MHz that provides the 536 MHz frequency shift needed to excite the $5S_{1/2}; F = 3 \rightarrow 5P_{3/2}; F^0 = 3; 4$ cross-over transition of ^{85}Rb in the vapor cell. This setup, first published by Hall [108], is shown in Figure [4.8]. With little optimization of the intensity and alignment of the probe beams we achieve a tight lock. As a result the main laser beam is easily tuned to the $5S_{1/2}; F = 3 \rightarrow 5P_{3/2}; F^0 = 5/2$ in ^{82}Rb and we have measured only small frequency drifts that corresponded to an uncertainty in the laser frequency of $\gg 500$ kHz, well below the required stability that we need for trapping.

Instead of using a laser diode system, which is commonly used to repump atoms

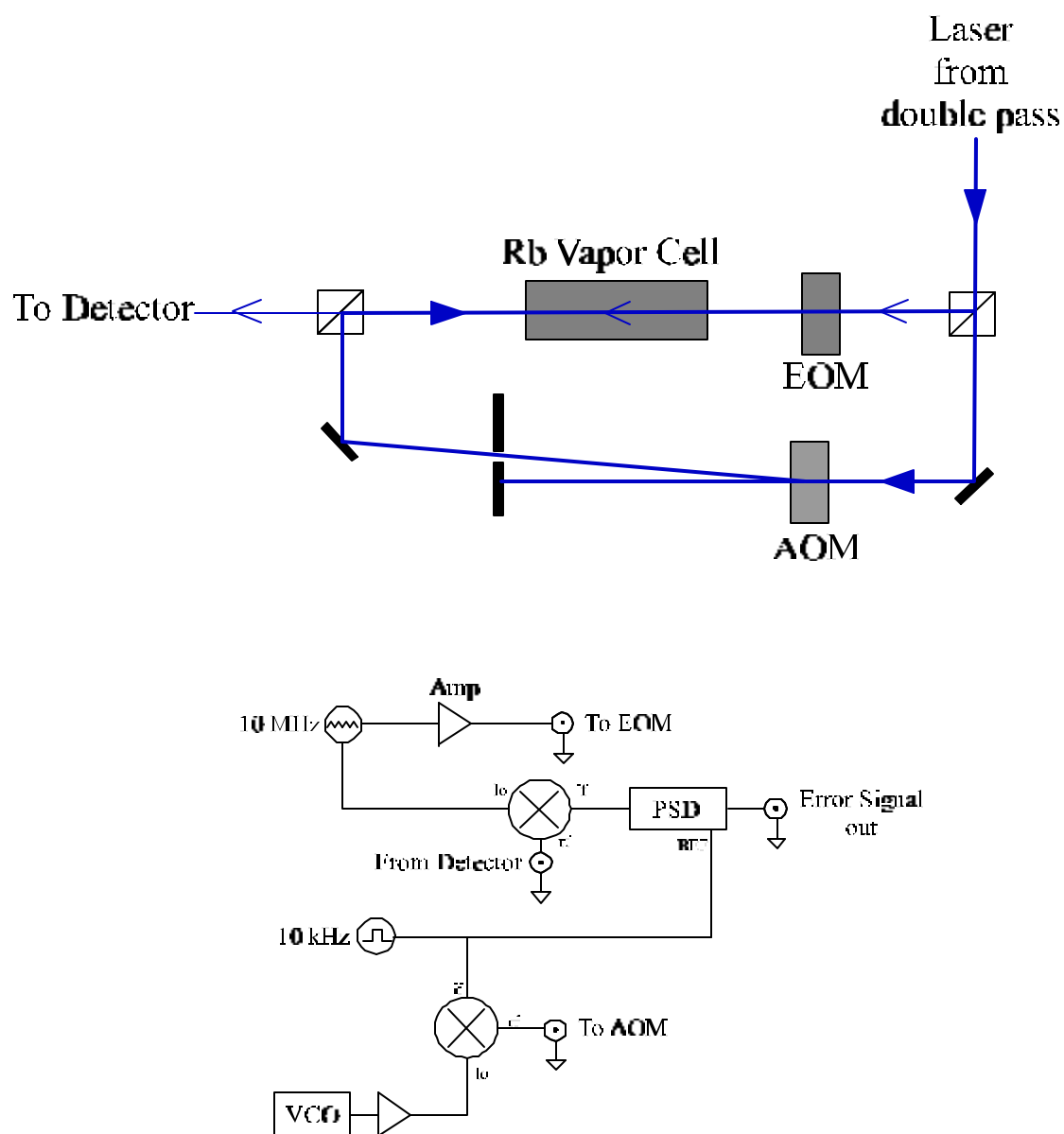


Figure 4.8: The saturated absorption setup and the corresponding electronics.

from the $5S_{1/2}; F = 1 \rightarrow 2$ ground state, we use an electro-optical modulator (EOM) to add sidebands at 1.470 GHz to excite the $5S_{1/2}; F = 1 \rightarrow 2 \rightarrow 5P_{3/2}; F^0 = 3 \rightarrow 2$ transition. This sideband method has two very desirable features:

1. The use of the EOM eliminates the need for a additional laser diode and corresponding locking electronics, thus simplifying the setup. Especially when searching for poorly known frequencies of the trapping and repump transition in ^{82}Rb . The presence of only a single laser (the Ti:Sa trapping laser) simplifies this search dramatically.
2. The EOM allows us to switch from trapping ^{82}Rb to ^{85}Rb very quickly. It turns out, that the repump transition frequency in ^{85}Rb can easily be excited by changing the EOM frequency to 1.463 GHz and the use of the second harmonic generated by the EOM. The EOM is driven with $\gg 4$ W of RF power which adds enough laser power into the second harmonic sideband at 2×1.463 GHz to trap ^{85}Rb . This very fortunate situation allows us to switch from trapping ^{82}Rb to ^{85}Rb in a few seconds while using only a single EOM.

The laser beam is split into three separate laser beams, expanded with a three lens telescope, and steered into the MOT. The MOT is formed by six circularly-polarized laser beams with a usable diameter of 5 cm and a $1/e^2$ width of 10 cm, which enter the cubic trapping cell through each surface. We use the retroreflected beam approach, rather than the six-beam configuration, since the attenuation of the laser light caused by the relatively small number of trapped radioactive atoms can be neglected. The power in each beam is measured to be 200 mW, and a set of large anti-Helmholtz coils generates the required quadrupole field gradient of 7 Gauss/cm in the axial direction.

It should be mentioned that for the transfer of the atoms into the second MOT outlined in detail in Chapter 5, part of the main laser beam is split off and steered to the second MOT. It is important to use the six-beam setup in the second MOT since the efficiency of the transfer process shows a strong dependence on the alignment of the second MOT relative to the push beam.

4.5 Light Detection Devices

A variety of detection devices are used to observe the fluorescence from the trapped atom cloud. On the following pages I will outline the use of different detectors and electronic setups required by the different detectors configurations.

4.5.1 The CCD-Camera

By far the simplest, cheapest, and most convenient detector used in both experiments is an ordinary CCD surveillance camera connected to a black and white monitor. However, the use of large laser beams in the trapping cell causes a huge amount of scattered light that can limit the use of the CCD camera. Nevertheless, when optimizing the MOT parameters (e.g. detuning, alignment, and magnetic field gradient), the camera proves to be extremely convenient. We were fortunate that, even when trapping radioactive ^{82}Rb , the camera is capable of detecting the trapped atom cloud using an optimized viewing position to minimize the amount of the scattered light (see Figure [4.9]). We can detect $\gg 100,000$ trapped atoms with the CCD camera.

It is known that the density of atoms in a MOT remains constant as a result of

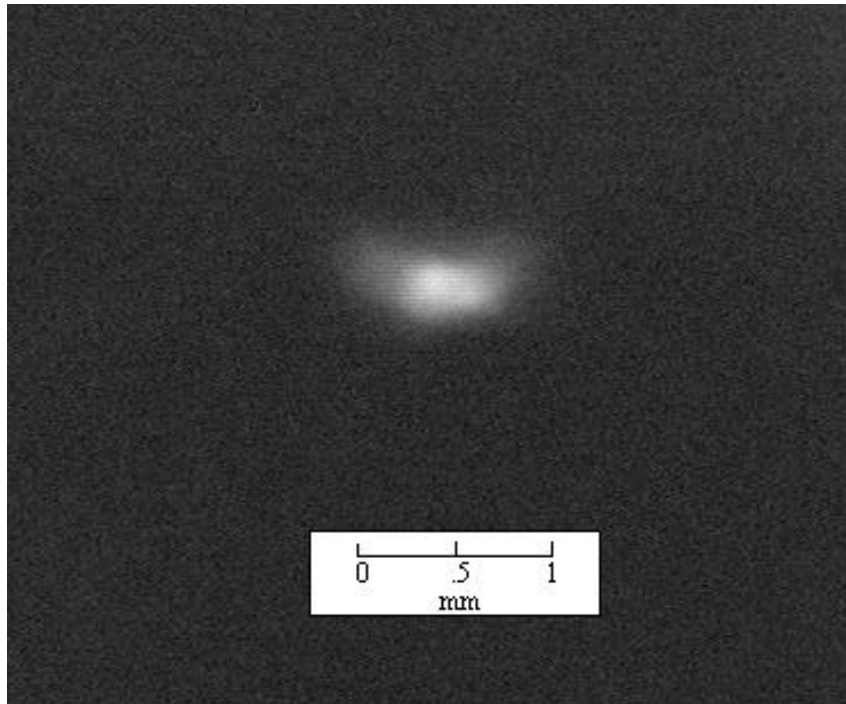


Figure 4.9: A picture taken with the CCD camera is shown. The fluorescing cloud corresponds to $\gg 1 \times 10^6$ ^{82}Rb atoms.

radiation pressure [55]. Therefore, the CCD camera can be used to determine the number of atoms in the trap by simply measuring the size of the cloud. While this method lacks accuracy for small numbers of atoms, it is useful as a cross-check to the more sophisticated fluorescence detection techniques. We found good agreement of the number of trapped atoms determined with the CCD camera and the results obtained from a PMT or photodiode, if we assume a density of $\gg 10^{10}$ atoms/cm³ in the trap. This number has been published in the literature [55] as a typical density obtained in MOTs and adds confidence to the results we obtain with the other detectors.

4.5.2 Calibrated Photodiode

The determination of the number of trapped atoms in the MOT requires a calibrated detector system. Reasonable accuracy, on the order 20-30%, is achieved by imaging the fluorescence of the cloud onto a calibrated photodiode. We are using a large area (1 cm²) photodiode with a quantum efficiency of $\gg 55\%$ at 780 nm and $\gg 60\%$ at 850 nm, respectively. The photodiode (PIN-10DP) is manufactured by UDT Sensors INC. The photodiode was connected to a home built I-V converter. The calibration is done with a NIST traceable light source (BNC Light Pulse Generator, Model 6020) featuring a precision of $\gg 10\%$ over a range of 10-70 μ W (see Figure [4.10]).

The main purpose of the photodiode combined with the simple I-V converter was to perform the retrapping efficiency measurement. Here, the large number of atoms trapped does not require any special means to suppress background. However, more sophisticated detection devices and schemes are necessary in case of the trapping of much smaller number of atoms.

4.5.3 Photomultiplier Tube

Detecting small numbers in the trap requires a more sophisticated approach. First, the use of a more sensitive detector proved to be important. We used a broadband Hamamatsu photomultiplier tube (Model R636-10) which peaks in the UV but has a relatively high quantum efficiency of $\gg 10\%$ at 780 nm. The active area of the tube is 3 mm wide and 12 mm tall which simplifies the alignment of the detector with respect to the trapped atoms.

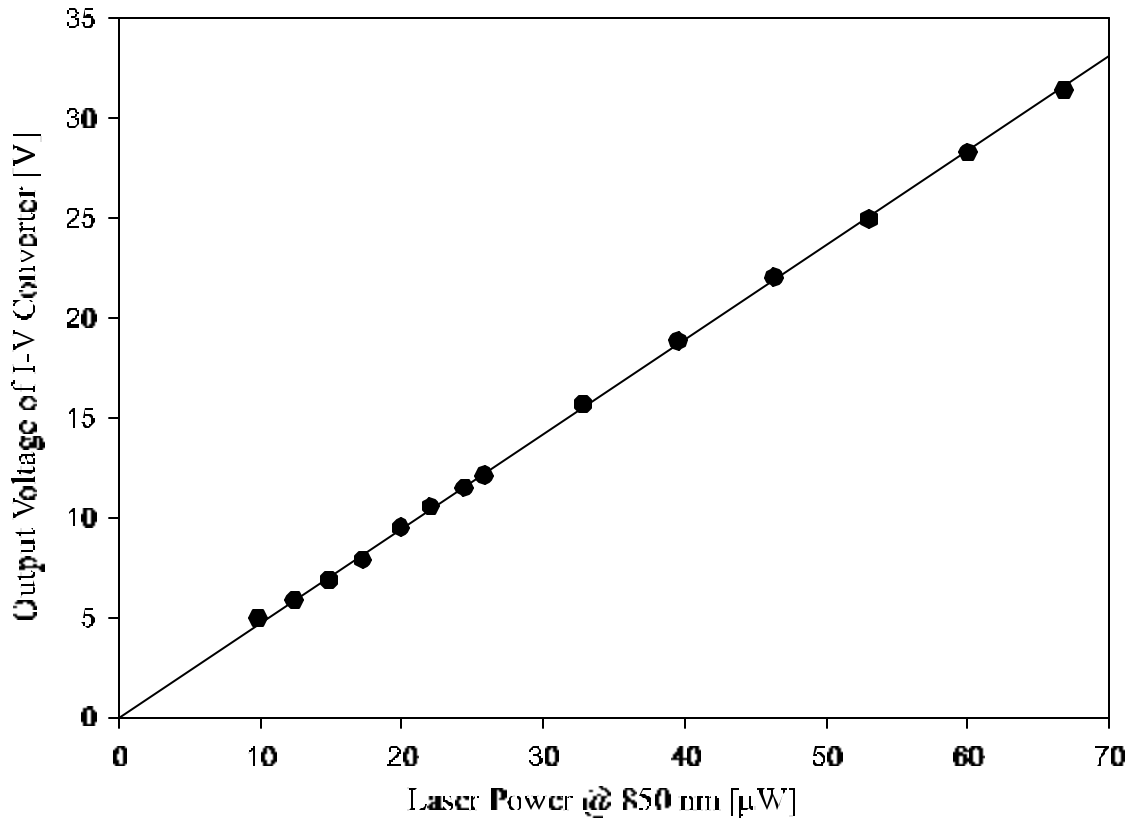


Figure 4.10: The calibration data of the PIN photodiode / I-V converter is shown. We use a BNC light source with an absolute accuracy of $\gg 10\%$. The line is a linear regression ...t which shows very good agreement with the data set.

We are using the photomultiplier tube exclusively in combination with a lock-in amplifier to perform phase-sensitive detection of the trapping signal. The details of this detection method are described on the following pages.

4.6 Detection Schemes

A variety of detection schemes are commonly used to determine the number of trapped atoms. The most accurate method was developed by Gibble et al. in the “monster trap” setup [107]. In the case of Cs, atoms are optically pumped from the $F = 4$ to the

$F = 3$ ground state by using a short laser pulse and recording the fluorescence during the pumping process. With known spontaneous emission branching ratios, one determines the average number of photons emitted per atom, thus the integral of the fluorescence is proportional to the number of atoms trapped. The advantage of this method is that it is independent of laser power and laser frequency. This allows an accurate determination of the number of atoms trapped.

A much simpler approach is to image the fluorescence from the trapped atom cloud onto a calibrated detector and calculate the scattering rate. The scattering rate is the number of emitted photons per second per atom and is given by

$$R_{\text{scat}} = \frac{\frac{I}{I_{\text{sat}}} \frac{\Gamma}{4}}{1 + \frac{I}{I_{\text{sat}}} + 4\left(\frac{\Phi}{\Gamma}\right)^2} ; \quad (4.9)$$

where I is the sum of the intensity of the six laser beams, I_{sat} is the saturation intensity, Γ is the assumed 6 MHz natural linewidth of the transition, and Φ is the laser detuning. Thus, one only needs to measure the detuning and the intensity of the trapping laser beams to calculate the scattering rate.

With the scattering rate in hand, one needs to measure the fluorescence F_{atoms} originating from the trapped atom to determine the number of trapped atoms. The number of trapped atoms is given by

$$N_{\text{atoms}} = \frac{F_{\text{atoms}}}{R_{\text{scat}}} ; \quad (4.10)$$

where the units for F_{atoms} is photons/sec which includes the specifics of the detector geometry and the detection method, as well as any losses in the detector arrangement. Once the calibration is done, this method provides a rather simple way of calculating the number of trapped atoms.

4.6.1 Phase-Sensitive Detection

Phase-sensitive detection is a method to suppress the background by modulating the trapping signal using an oscillating reference signal. The reference signal is fed into a lock-in amplifier (Stanford Research Systems Model SR830) which eliminates almost the entire background due to scattered light. Here, we take advantage of the large difference in intensity of the trapping and repumping laser beam. Modulation of the trap fluorescence is easily achieved by turning the repump laser beam on and off. This is achieved by turning the EOM, that creates the sidebands, on and off at a conveniently chosen rate of $\gg 4$ kHz. Without the repump, the atoms are pumped into the dark state and the trap fluorescence vanishes, thus modulating the trapping signal.

In addition, the trap fluorescence is detected using an imaging lens (focal length = 58mm; $f=1:4$) and a pinhole (0.1-3 mm diameter) arrangement, which reduces the scattered light background signal even further. The entire setup is carefully calibrated, taking into account losses due to uncoated surfaces, the solid angle, and modulation effects caused by the phase sensitive detection technique to allow the determination of the number of trapped atoms by detecting the fluorescence from the trapped atom cloud. As a lower limit, we can detect $\gg 4000$ atoms in the trap with the PMT in phase-sensitive detection mode. The uncertainty in the number of atoms trapped using this technique is estimated to be $\gg 30\%$ (limited by the uncertainty in the laser detuning).

4.6.2 Photon Counting

The most sensitive detection scheme that we investigated uses photon counting. The scheme is shown in Figure [4.11] for the case of ^{85}Rb . The atoms in the trap are

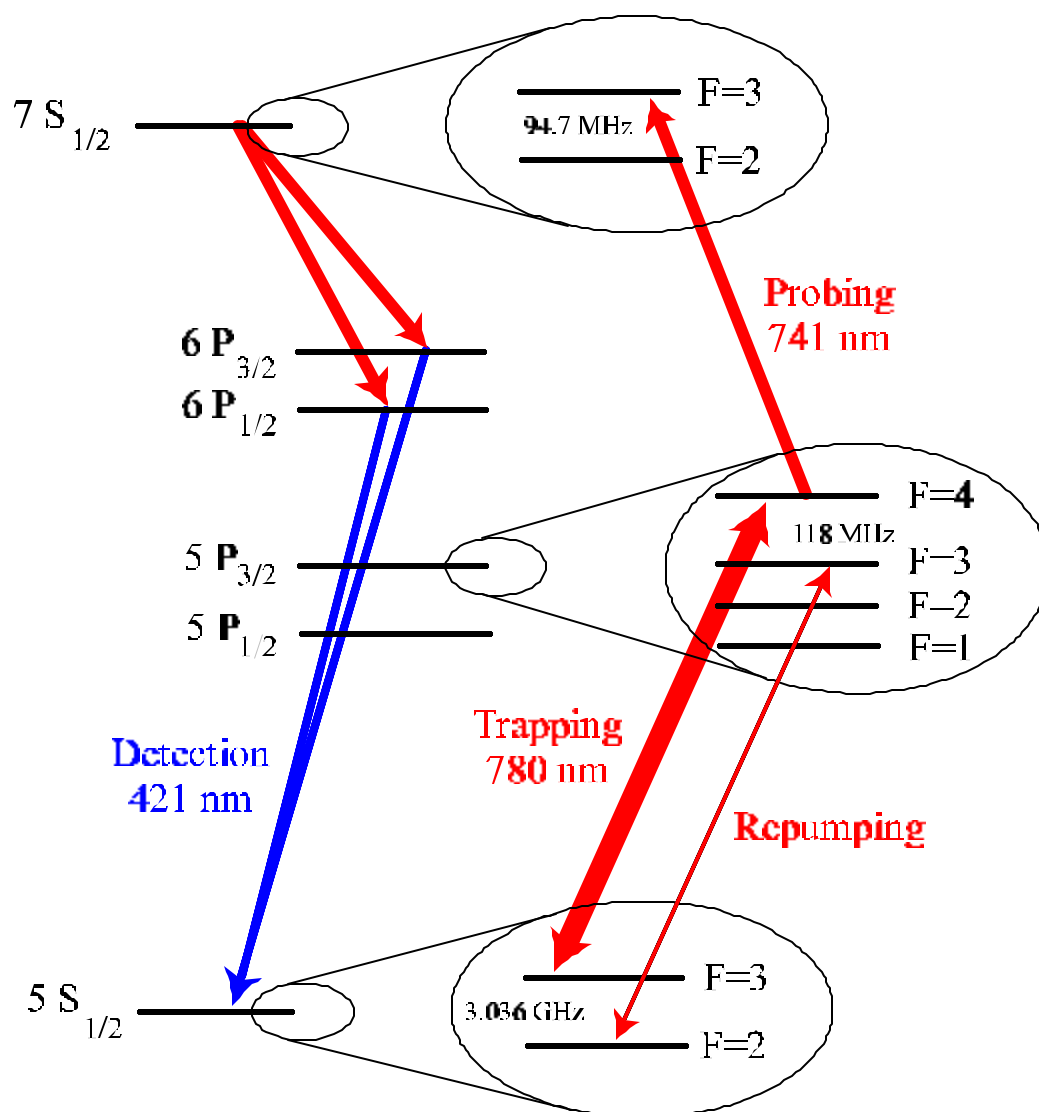


Figure 4.11: The energy levels in ^{85}Rb for the detection of blue photons are shown.

further excited out of the $5P_{3/2}$ state to the $7S_{1/2}$ state using a probe laser tuned to 741

nm. From the $7S_{1=2}$ state, the atom can decay to the $6P_{1=2}$ or the $6P_{3=2}$ states and then decay further to the $5S_{1=2}$ ground state by emitting a blue photon (421 nm). With the help of an interference filter centered at 421 nm the scattered light from the trapping cell can be suppressed dramatically.

The PMT signal is amplified and the pulse height is analyzed using standard NIM electronics. Since the pulse height is proportional to the energy of the detected particle, it is possible to distinguish between the "blue photons" originating from the trap and the background which we attribute to the γ radiation originating from the ^{82}Rb atoms accumulated in the catcher foil. Those γ -rays are much more energetic than the blue photons, which is reflected in the pulse height of the PMT signal. By setting a gate around the energy region of interest, the background signal can be strongly suppressed. The resulting signal is converted into a TTL pulse and counted with an ORTEC 776 scalar.

Typical noise levels using this method are on the order of $\gg 0.1$ counts/sec. While the trapped atoms typically cause very large count rates ($\gg 0.01$ count/sec/atom). Consequently, we were able to detect as few as 10 trapped atoms. However, the theoretical limit of this technique is a single trapped atom.

Chapter 5

Trapped Radioactive Rubidium Atoms

In this chapter, we will focus on the trapping experiment and atomic structure measurements performed with trapped ^{82}Rb in the MOT. The very cold atoms in a MOT represent a well suited ensemble which allows for a variety of atomic structure measurements. The systematic perturbations, namely the small Zeeman and Stark shift caused by the electric and magnetic fields present in the MOT (on the order of ≈ 1 MHz) can relatively easily be corrected or in some cases neglected all together. A variety of examples for atomic structure measurements performed in MOTs can be found in the literature [109, 110], with Reference [111] representing the most precise measurements performed with trapped radioactive atoms despite the very small number of ^{210}Fr atoms trapped.

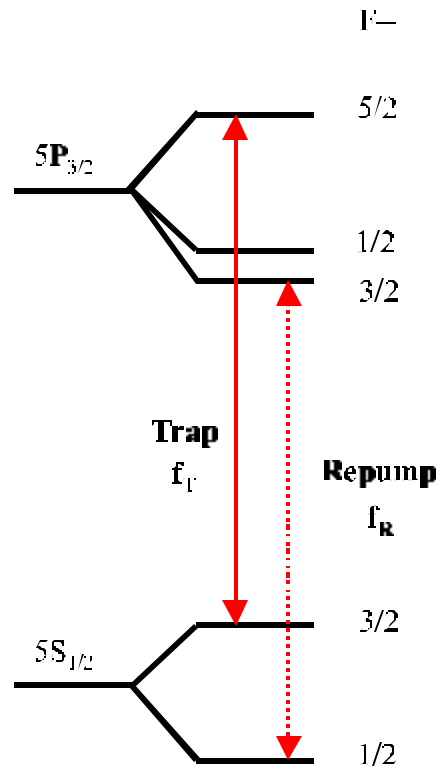
5.1 Laser Setup for ^{82}Rb

The laser setup for trapping atoms from the mass separator is described in detail in Chapter 4. Briefly, the output beam from a commercial Ti:Sa laser (Coherent 899-21) is used to trap radioactive ^{82}Rb atoms released from the yttrium catcher foil that is located inside the trapping cell. The Ti:Sa laser is tuned to the D_2 line of Rb at 780 nm and locked to the $5S_{1/2}; F = 3 \rightarrow 5P_{3/2}; F^0 = 3; 4$ cross-over transition of ^{85}Rb using a FM sideband technique [108]. A double-pass acoustic-optical modulator (AOM) driven at 268 MHz provides the 536 MHz frequency shift needed to excite the $5S_{1/2}; F = 3 \rightarrow 5P_{3/2}; F^0 = 5; 2$ trapping transition in ^{82}Rb [112]. In order to repump atoms which accidentally fall into the $5S_{1/2}; F = 1 \rightarrow 2$ ground state, sidebands are added to the trapping beam by using an electro-optical modulator (EOM) tuned to 1.470 GHz which excited the $5S_{1/2}; F = 1 \rightarrow 5P_{3/2}; F^0 = 3; 2$ transition. For trapping ^{85}Rb , however, the EOM is tuned to 1.463 GHz and the second harmonic generates the repump light. Trapped atoms are detected by chopping the EOM at 4 kHz, which modulates the trap fluorescence signal. The relevant transitions of ^{82}Rb and ^{85}Rb are shown in the level diagram of Figure [5.1].

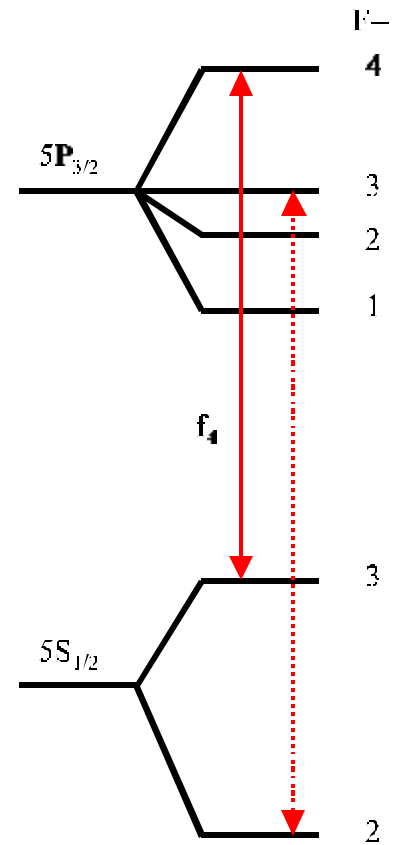
5.2 Modes for Trapping from the Mass Separator

The dry...lm coated trapping cell is connected to the mass separator using standard vacuum hardware. Differential pumping throughout the mass separator in addition to a Varian StarCell ion pump mounted immediately before the trapping cell enables us to reach very low pressures ($\gg 1 \times 10^{-10}$ torr). The resulting lifetime for the atoms in the trap are 30 s with the catcher foil continuously heated to 750 $^{\circ}\text{C}$, and 90 s with the foil heating turned

^{82}Rb ($I=1$, $t_{1/2} = 75$ s)



^{85}Rb ($I=5/2$, stable)



$$f_T - f_4 = 536 \text{ MHz}$$

$$f_T - f_R = 1470 \text{ MHz}$$

Figure 5.1: The energy level diagram for ^{82}Rb and ^{85}Rb is shown. The trapping transitions $5S_{1/2}; F=3 \rightarrow 5P_{3/2}; F=4$ in ^{82}Rb and $5S_{1/2}; F=3 \rightarrow 5P_{3/2}; F=4$ in ^{85}Rb and the corresponding frequency differences are highlighted.

or. Thus, ^{82}Rb can be accumulated either in the foil (pulsed mode) or in the trap while continuously heating the foil (continuous mode).

5.2.1 Trapped Radioactive ^{82}Rb Atoms

Figure [5.2] shows the pulsed release from the catcher foil and the corresponding trapping signal for ^{82}Rb after implanting $\gg 3$ mCi of ^{82}Rb into the catcher foil.

In the upper half, the temperature of the catcher foil is shown as measured with an optical pyrometer upon excitation of the heating coil. The second recorded parameter is the count rate of the 776 keV γ -rays emitted from the accumulated ^{82}Rb atoms in the catcher foil as monitored with a collimated NaI γ -detector as a function of time. The drop in count rate indicates that $\gg 35\%$ of the ^{82}Rb atoms are released from the foil and leave the region viewed by the collimated γ -counter. Measurements with and without a negative 300 V suppression voltage applied to the catcher foil indicate that essentially all of the activity is released in the form of neutral atoms. The 1/e release time of the ^{82}Rb activity from the catcher foil is measured to be $\gg 5$ seconds.

The bottom half shows the corresponding lock-in trapping signal as a function of time. A strong trapping signal is evident with a risetime consistent with the release profile recorded with the collimated γ -counter. Additional measurements with shorter foil heating times indicate that the trapping signal decays with a 1/e lifetime of 50 s, corresponding to a 90 s trap lifetime and the 75 s half-life of ^{82}Rb when operating in pulsed mode.

We find, that no trapping signal is observed if:

1. The foil is not heated, but ^{82}Rb ions are accumulated onto the foil;

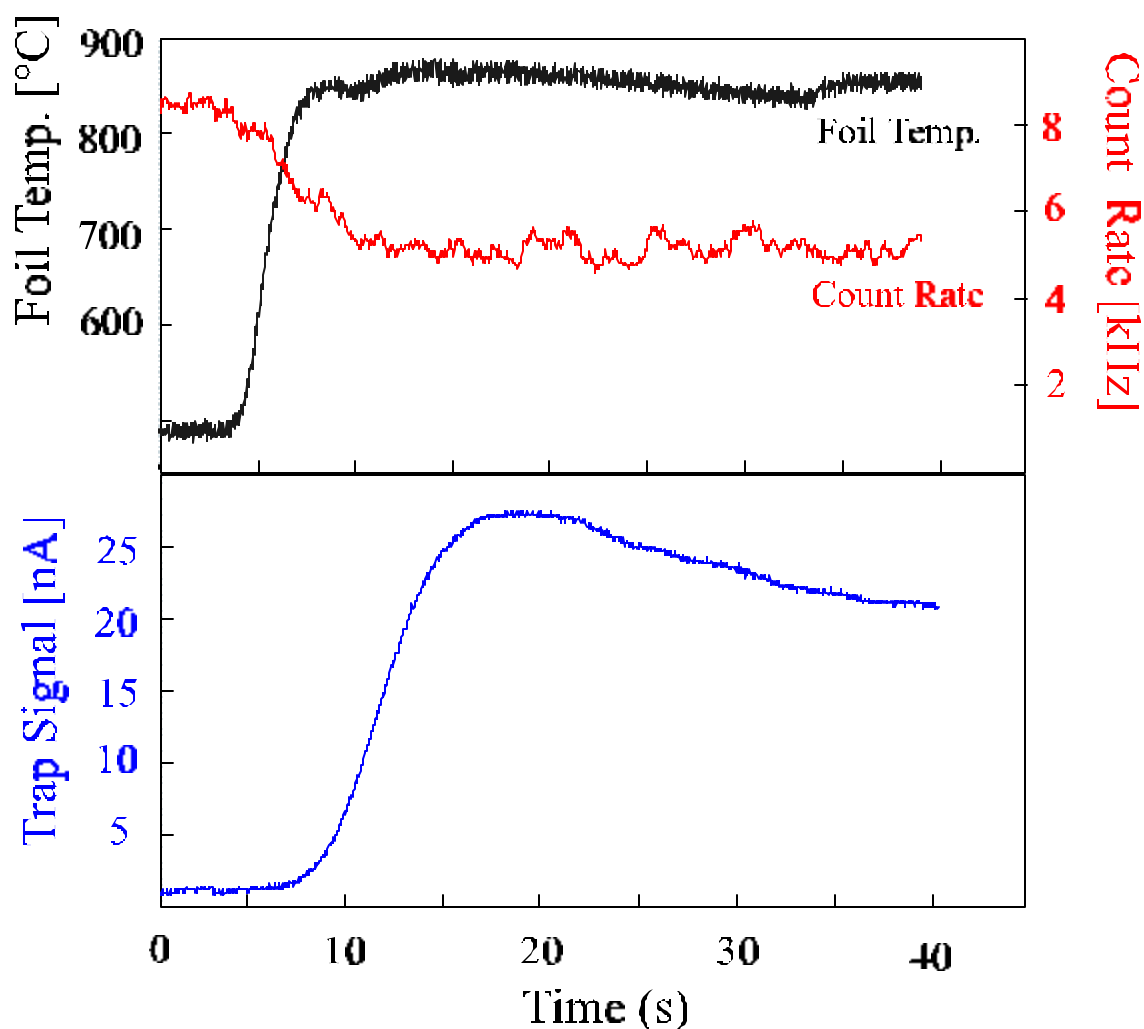


Figure 5.2: The upper half of the figure shows the temperature of the catcher foil as measured with an optical pyrometer and the release of ^{82}Rb from the catcher foil upon heating, by monitoring the 776 keV γ -rays with a collimated NaI detector. The drop in count rate indicates that $\gg 35\%$ of the ^{82}Rb atoms are released and leave the viewing region. The bottom half of the figure shows the lock-in trapping signal as a function of time.

2. The foil is heated, but no ^{82}Rb is implanted into the catcher foil;
3. The foil is heated and ^{82}Rb is implanted into the foil, but the magnetic field of the MOT is reversed.

All of the above cross-checks attribute the fluorescence signal to trapped ^{82}Rb . The number of trapped atoms is deduced from the trapping signal using a calibrated photodiode, yielding $(6 \pm 2) \times 10^6$ and $(3 \pm 1) \times 10^6$ trapped ^{82}Rb atoms for the pulsed and continuous operation, respectively. The difference in the number of trapped atoms in continuous and pulsed mode is understandable when one analyzes the trapping process. With lifetimes in the trap in excess of 30 s (when operating in continuous mode) the situation is best described by accumulation of the atoms occurring in the MOT itself, compared to accumulation in the catcher foil. Indeed, when we empty the trap and record the trapping signal as a function of time, we see the trapping signal slowly growing. Also, when operating in continuous mode, we carefully optimize the trapping signal and hence the number of trapped atoms by adjusting the catcher foil temperature. The hot catcher foil itself is causing a small gas load, which at most increases the pressure in the trapping cell by a factor of 3, thus affecting the lifetime of the atoms in the trap. Equally important, residual gas particles slowly accumulate on the cold catcher foil, thus the “history” of the catcher foil temperature has an effect on the trap lifetime. This is easily understood, since at such low pressures, it takes time to cover a cold catcher foil with a monolayer of residual gas molecules which are released upon heating. Therefore, we strongly believe that the difference in the number of trapped atoms is strictly due to changing vacuum conditions in the MOT trapping chamber when heating the catcher foil.

Since the double MOT system is an essential part of the proposed β -asymmetry measurement and continuous operation of the first MOT is favorable, we decided to optimize the number of atoms trapped in continuous mode rather than carefully investigating the pulsed mode. Nevertheless, the measured numbers are orders of magnitude larger than any previous work reported with radioactive atoms [6] and, for the first time ever, are large enough to allow a high-precision β -asymmetry measurement using trapped atoms to be attempted.

5.2.2 Efficiency Considerations

Large numbers of trapped atoms are essential to the future of measurements using a sample of trapped atoms and their achievement now for ^{82}Rb allows the realization of a first generation β -decay experiment of this type. However, improvements in the efficiency of the described system are possible.

A true measure of the quality of the described system is its overall efficiency. The efficiency of the system can be calculated as

$$\epsilon_{\text{total}} = \frac{N_{\text{trap}}}{\tau_{\text{trap}} A_{\text{Rb}}} \quad (5.1)$$

where $N_{\text{trap}} = 3 \times 10^6$ is the number of trapped atoms, $\tau_{\text{trap}} = 30\text{s}$ is the lifetime in the trap, and $A_{\text{Rb}} = 3 \times 10^8$ disintegrations per second is the ^{82}Rb activity in the ion source, we obtain an overall efficiency of $\gg 0.03\%$. Breaking this down stepwise, we obtain an ionization and overall separation efficiency of $\gg 35\%$, a catcher foil release efficiency of $\gg 30\%$ at 750°C , and a trapping efficiency of $\gg 0.3\%$.

Large numbers of implanted radioactive ^{82}Rb ions proves that the ionization and

release efficiency of the ion source as well as the transfer efficiency of the mass separator are sufficiently high and therefore further improvements promise only marginal gains in the amount of activity accumulated on the catcher foil. The release efficiency of the catcher foil also is relatively high and can hardly be improved without sacrificing the vacuum conditions in the trapping cell. However, the trapping efficiency of the MOT, being only 0.3%, promises the biggest possible gain. As outlined in Chapter 4, the trapping efficiency can only be improved by:

- (a) using a larger laser beam diameter L - increasing the number of trapped atoms by $N \propto L^{3/2}$ at constant laser intensity; and
- (b) allowing the atoms to bounce off the surface of the trapping cell more often by using a better non-stick dry-film coating.

In our current setup we use quarterwave plates with a usable diameter of only 4.6 cm. Larger waveplates (8 cm diameter) will likely improve the trapping efficiency by a factor of $\gg 4$, but they are hard to manufacture and consequently very expensive.

A simple calculation of the capture velocity of our MOT system yields a lower limit for the single-pass trapping efficiency of $\gg 1 \times 10^{-4}$. Thus, we estimate that a maximum of 30 "bounces" on average occur, despite a theoretical maximum of 600 bounces given by the ratio of surface area of the trapping cell and the sum of the surface areas of entrance and exit holes as well as the catcher foil. This lack of agreement between the theoretical predictions and the experimental results can only be explained by introducing an additional loss mechanism that affects the trapping efficiency. The leading candidate obviously is the dry-film coating of the trapping cell which could have an increased chemical reaction rate

with the Rb atoms. Thus, we decided to try to find a definitive method of evaluating the quality of the dry-film coating.

A careful investigation of the quality of several dry-film coatings is presented in Reference [113]. Here, an electron microscope scan is used to investigate the quality of the coating, especially any spots on the glass surface that have not been coated. This work has also led to a new technique called “afterwash”, which removes additional layers of the dry-film that is not chemically bonded to the glass surface, drastically improving the outgassing rate and sticking time of SC-77 (see Chapter 4). Unfortunately, the described method can not be applied to the complex geometry of typical trapping cells, and thus only represents a possible check of the coating procedure rather than a way of evaluating the coating of our cell. In addition, one would like a measurement which determines the quality of the coating as a function of time, implying a measurement on the trapping cell in situ.

We have thus proposed a new technique for in situ testing of the dry-film coating in more complicated geometries typical for trapping cells. The use of the γ -rays from the decay of the radioactive sample allows for the measurement of sticking time and uniformity of the radioactive atoms on the surface. When using an additional collimated NaI γ -counter we found that a large portion of the activity sticks to the cell walls. The measured sticking time equals the natural half-life of ^{82}Rb which implies that the atoms stick to the wall permanently. This could be explained by a damaged coating with an increased chemical reaction rate. Further investigation is necessary to determine if the coating slowly degrades with time or if the chosen coating procedure is less than optimal. To this end we are using the γ -ray monitoring technique to select the best type of dry-film coating to be used in the

future.

5.3 Measurements on the Trapped Atoms

The trapped atoms in the MOT might be used to perform a variety of atomic physics measurements. Lifetime measurements as well as measurements of the atomic structure in ^{82}Rb are foreseeable or have been started. Here we will discuss early measurements which determine the optimal detuning of the trapping laser and measure the exact location of the $5S_{1/2}; F = 3 \rightarrow 2$! $5P_{3/2}; F^0 = 5 \rightarrow 2$ trapping transition in ^{82}Rb .

The experimental setup for these measurements is very simple. A separate probe beam with a power of 80 μW and a diameter of 5 mm is split off from the main trapping beam and its frequency is shifted using two AOMs arranged in series. The first AOM shifts the frequency by a fixed amount of - 80 MHz, the second allows a variable frequency shift of 55-105 MHz. The AOMs are arranged to give a net shift of ± 25 MHz with respect to the trapping laser. The second AOM is chopped on and off to modulate the probe beam at a rate of 7 kHz.

When the circularly-polarized, counter propagating probe beam is overlapped with the trapped atom cloud the result is a partially modulated trapping fluorescence signal. Maximum modulation occurs when the probe beam is on resonance with the atomic transition. The resulting signal is shown in Figure [5.3] and determines the exact position of the $5S_{1/2}; F = 3 \rightarrow 2$! $5P_{3/2}; F^0 = 5 \rightarrow 2$ trapping transition in ^{82}Rb . This simple measurement also represents a crude measurement of the linewidth of the transition. One expects a natural linewidth similar to the precisely measured linewidth of the trapping transition in ^{85}Rb

($\Gamma = 6$ MHz). Our measurement sets an upper limit on the linewidth of 8 MHz, which is not far off the predicted value, especially if one keeps in mind that this simple measurement is aimed to measure the location of the transition but not the linewidth precisely.

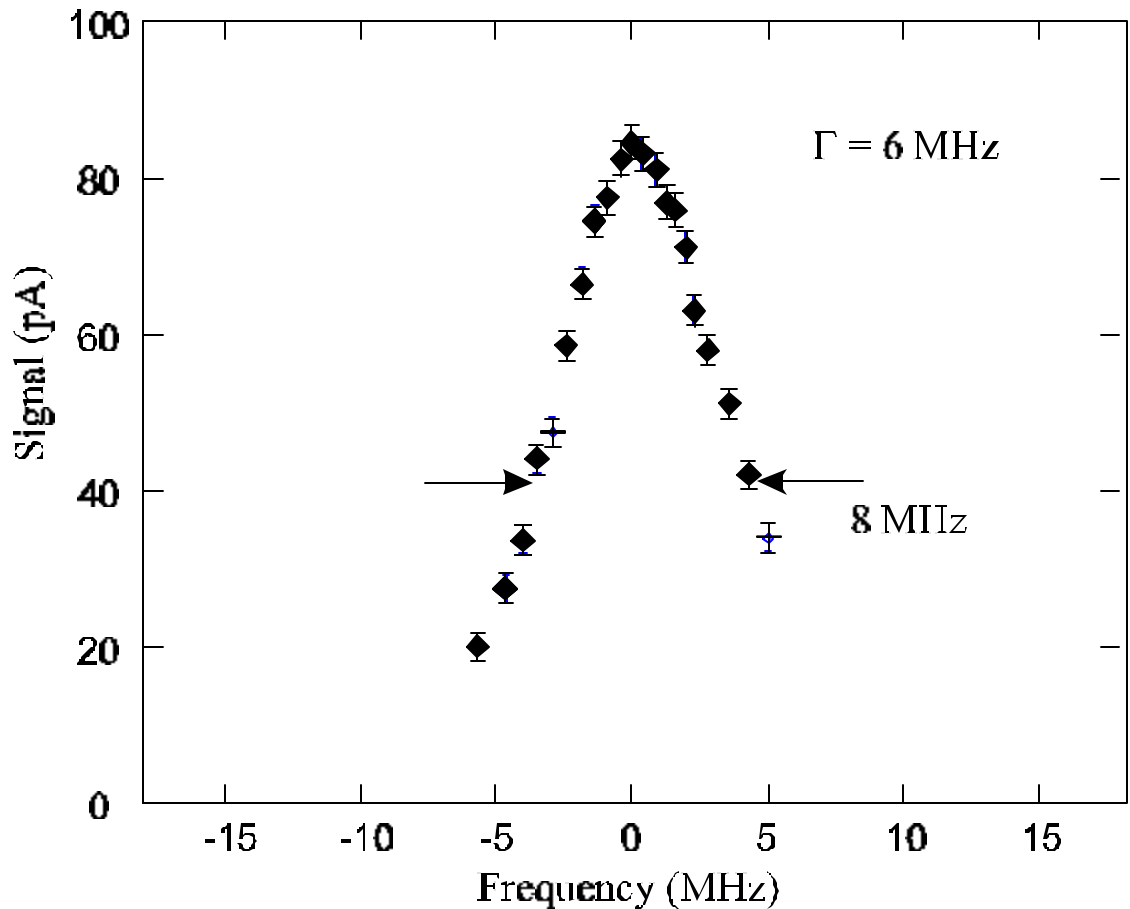


Figure 5.3: The measurement of the linewidth of the trapping transition $5S_{1/2}; F = 3 \rightarrow 2 \rightarrow 1 \rightarrow 5P_{3/2}; F^0 = 5 \rightarrow 2$ using a pair of AOMs to provide the frequency shift of 25 MHz is shown. The second AOM is chopped at 7 kHz to modulate the trapping fluorescence signal.

The resulting frequency difference between the $5S_{1/2}; F = 3 \rightarrow 2 \rightarrow 1 \rightarrow 5P_{3/2}; F^0 = 5 \rightarrow 2$ transition in ^{82}Rb and the $5S_{1/2}; F = 3 \rightarrow 2 \rightarrow 1 \rightarrow 5P_{3/2}; F^0 = 4$ transition in ^{85}Rb has thus been measured to be 536 ± 5 MHz, which is in good agreement with the previous measurement of 540 ± 7 MHz done at ISOLDE [112].

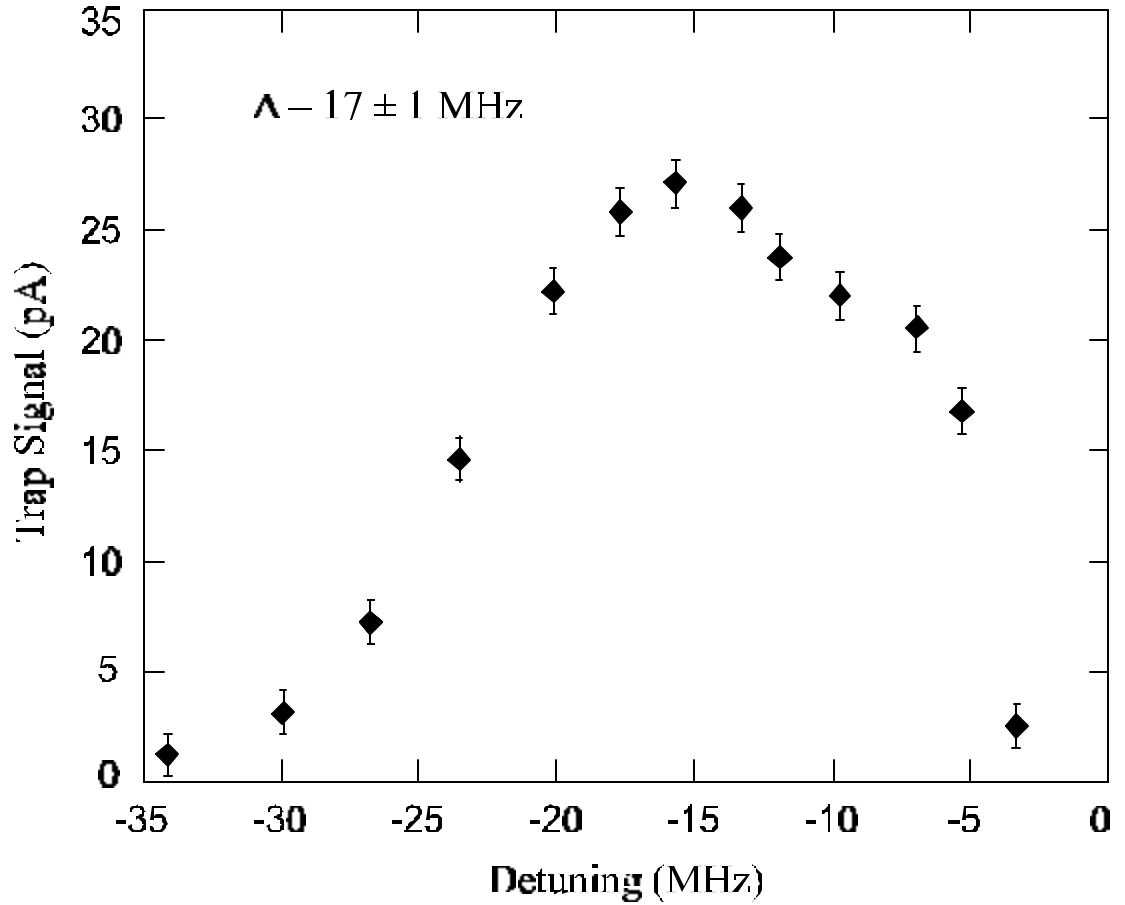


Figure 5.4: The fluorescence signal from the trap as a function of a probe laser frequency is shown. We use this technique to determine the optimal detuning of the trapping laser.

With knowledge of the exact location of the $5S_{1/2}; F = 3 \rightarrow 2$! $5P_{3/2}; F^0 = 5 \rightarrow 2$ trapping transition in ^{82}Rb , we can determine the optimal detuning of the trapping laser by simply changing the laser frequency and recording the fluorescence signal of the trapped atom cloud as a function of laser frequency. We found the maximum fluorescence signal at a trapping laser detuning of -17 ± 1 MHz (Figure 5.4) and, when calculating the number of trapped atoms by including the scattering rate and the measured detuning values, we found the maximum number of trapped atoms at a trapping laser detuning of -20 ± 1 MHz.

However, the difference in the number of trapped atoms between a laser detuning of 17 and 20 MHz is only 10-15%.

Following the same approach, we are currently working on a scheme to measure the hyperfine splitting of the $5S_{1/2}$, $5P_{1/2}$, and $5P_{3/2}$ states, the isotope shift of ^{82}Rb , and possibly some of the lifetimes of the atomic states using a technique described in Reference [111]. The results of the atomic structure measurements will be published at a later time.

Chapter 6

High-Precision Measurements using Trapped Atoms

A variety of possible experiments to probe the Standard Model of electroweak interactions are foreseeable with an intense point-like source of trapped atoms. Each of the experiments will have a need for a specially designed and optimized detector chamber, but the general layout of the experiments are very much alike. In this chapter, I will outline the “next step” that needs to be taken, after the successful trapping of a large number of radioactive atoms as demonstrated herein.

6.1 The Layout of the τ -Asymmetry Experiment

Currently under construction, the τ -asymmetry setup will serve as an example to outline the general layout of the proposed high-precision experiments. While the trapping vessel, coupled to the mass separator, requires large and intense laser beams and the use

of a dry...lm coating, the requirements for the detector chamber are somewhat different. In reality, it is extremely difficult, if not impossible, to design an efficient trapping cell that can double as a detector chamber. For this reason, the trapped atoms will need to be transferred to a second chamber that is optimized for the desired detector arrangement. The general layout of the proposed beta-asymmetry measurement in ^{82}Rb is shown in Figure [6.1]. Atoms

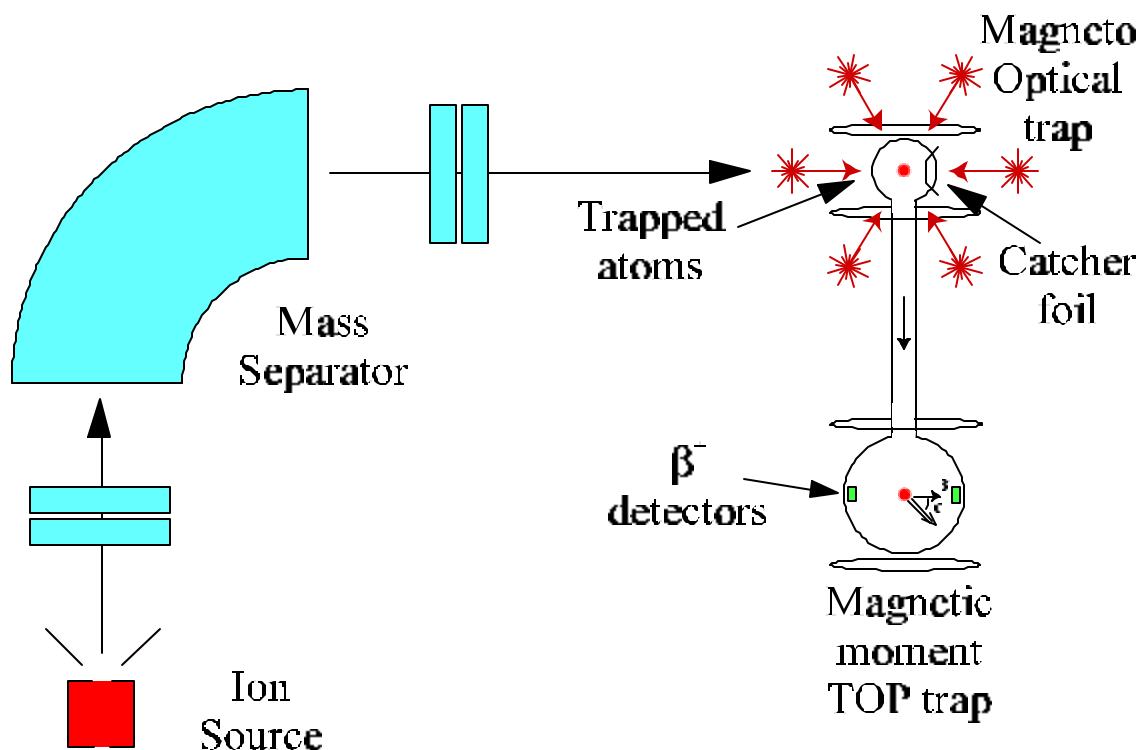


Figure 6.1: A overview of the ^{82}Rb β^- -asymmetry measurement is shown. ^{82}Rb atoms are ionized in a thermal ion source and mass separated. The ions are implanted into a catcher foil within the trapping cell. Upon heating, ^{82}Rb atoms are released and trapped by the MOT beams. The trapped atoms are pushed into a second MOT, spin-polarized and loaded into a magnetic moment trap where the β^- -asymmetry measurement is performed.

are produced in the ion source, mass separated and implanted into the catcher foil within the trapping cell. Upon heating, the atoms are released and trapped in the MOT. After being trapped, the atoms are pushed into a second MOT, spin polarized using optical pumping

techniques and loaded into a magnetic moment trap to achieve high spin-polarization with a well defined orientation of the nuclear spin in space. In addition, a γ -detector is mounted in the vacuum chamber of the second MOT / magnetic moment trap.

6.2 Transferring Atoms

Developed for the production of large Bose-Einstein condensates [114], the two MOT systems present a simple way of overcoming fundamental limitations in a single MOT system. In particular, the product of the number of trapped atoms times the confinement time, $N\tau$ is largely enhanced. The loading rate into a MOT increases with the density of the alkali vapor, but the confinement time is inversely proportional to the pressure in the chamber due to collisions between the trapped atoms and the relatively hot atoms in the background gas. For most applications, including the γ -asymmetry measurement which we are interested in here, a long confinement time in addition to a large number of trapped atoms is desirable. In particular, the very large gamma-count rate caused by ^{82}Rb atoms that remain within the catcher foil and the necessity of an all-glass surface causes the first MOT to be unsuited for a high-precision experiment.

A system with two MOTs, the first one being optimized for the efficient trapping from the mass separator while the second one is optimized for the measurement of the asymmetry function, overcomes the limitations of a single MOT. It has been shown that the product $N\tau$ can be increased by a factor of more than 1000 in a double MOT system [115, 114]. More importantly for the γ -asymmetry experiment, the density of the untrapped background gas that would increase the decay rate can be lowered dramatically due to

achievable transfer efficiencies from the first MOT into the second MOT of $\gg 90\%$. Also, the much lower pressure achievable in the second MOT will allow storage times of several hundreds of seconds in the magnetic trap, equally important for the proposed π -asymmetry measurement.

6.2.1 The Double MOT System

The apparatus for loading the trapped atoms into the second MOT is shown in Figure [6.2]. A quartz adapter with a stainless steel bellows is attached to the 5 mm diameter exit port of the trapping cell. The bellows is included to compensate for thermal expansion during the vacuum bake out of the system, thus minimizing the possibility of cracking the quartz cell.

We achieved remarkably low pressures in the first MOT and the confinement time τ_c of the trapped atoms has been measured to be $\gg 100$ s, which corresponds to a pressure of $\gg 3 \times 10^{-10}$ torr. Since the conductance of the 40 cm transfer tube (1.1 cm diameter) is very small ($\gg 0.4$ l/s in the molecular transport regime and under the assumption of no sticking to the surface walls) it will allow us to differentially pump the second chamber to even lower pressures. Ultimately, it is desirable to achieve a storage time of the polarized sample within the magnetic moment trap of $\gg 250$ s, thus a pressure of $\gg 1 \times 10^{-10}$ torr is needed.

These ultra-high vacuums can be achieved by using the combination of an ion pump and a large titanium sublimation pump. We are using two 20 l/s Varian StarCell ion pumps to remove the noble gases and a Varian titanium sublimation pump which features a much larger pumping speed for active gases, especially hydrogen. The titanium sublimation

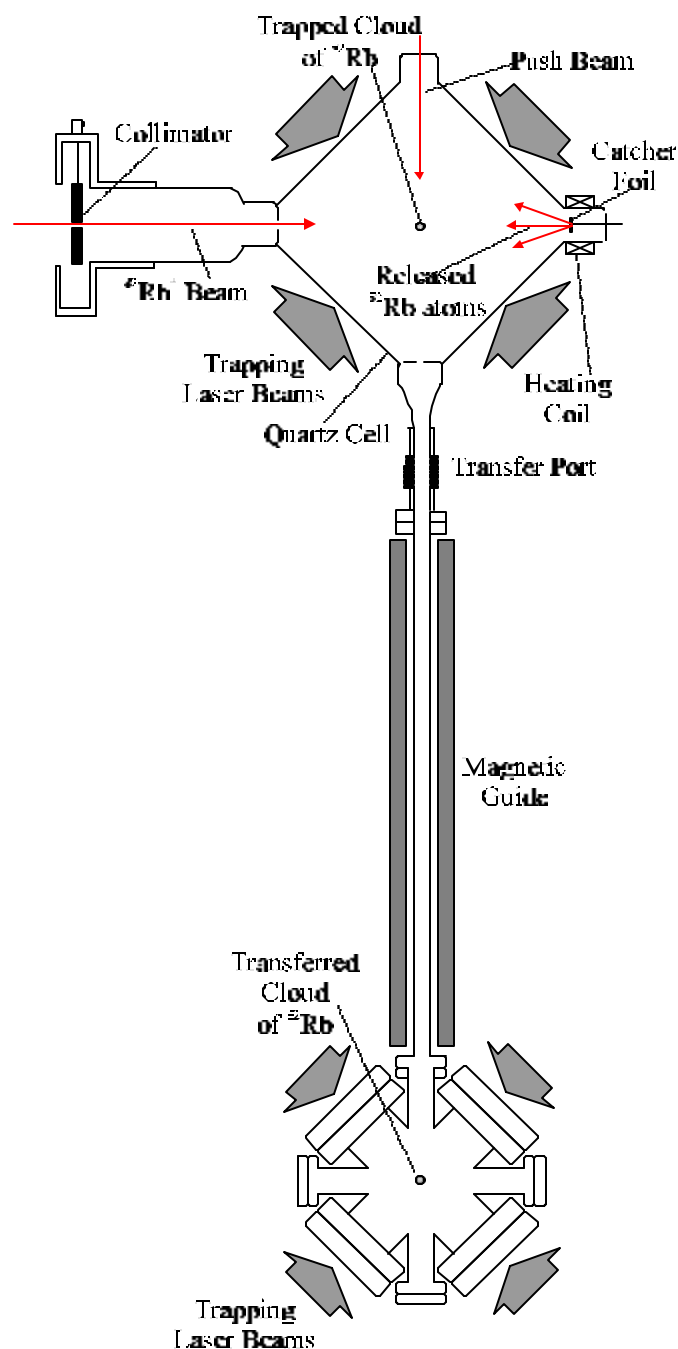


Figure 6.2: The double MOT apparatus we use to develop the source transfer technique is shown. Atoms are efficiently trapped in the first MOT. A push beam is used to polarize and accelerate the trapped atoms towards the second MOT. The hexapole magnetic guide helps to confine the atoms near the axis of the transport line. Smaller diameter laser beams (but with the same light intensity) can be used to retrap the atoms in the second MOT.

pump is mounted within a tube of 3.7 cm diameter, the filament has a length of $\gg 10$ cm, thus $\gg 100 \text{ cm}^2$ can be coated with titanium. As a result, one expects the pumping speed for the titanium sublimation pump to be $\gg 300 \text{ l/s}$ for hydrogen at room temperature, in which case our pumping speed would be limited by the conductance of the tube that connects the pump to the MOT chamber ($\gg 150 \text{ l/s}$). It should be mentioned that one expects a differential pumping factor of $\gg 100$ for mobile species such as hydrogen or helium whereas the sticking time of Rb on stainless steel is very long and therefore the conductance for Rb is negligibly small.

6.2.2 Magnetic Guidance

It is well known since the early 1950s that inhomogeneous magnetic fields may be used to guide or focus neutral particles with a permanent or induced magnetic dipole moment [116, 117]. In fact, at ILL a magnetic storage ring was built to confine slow neutrons in an attempt to measure the natural beta decay lifetime of the free neutron [118].

Similarly, magnetic fields can be used to guide atoms through a transfer tube to prevent collisions with the surface of the vacuum vessel. This was first demonstrated at JILA [115, 114] where transfer efficiencies of up to 90% were achieved. Recently, we have achieved transfer efficiencies of $75 \pm 15\%$ for stable ^{85}Rb atoms. We are currently working on the efficient transfer of ^{82}Rb into the second MOT.

In the magnetic guide we use a hexapole field to provide a two-dimensional harmonic potential for the transfer of spin-polarized atoms. Surprisingly simple, the original work used an arrangement of small kitchen magnets, but rather successful can the atoms be transferred. However, since the magnetic stray field of the permanent magnets could

Magnetic Guide and Transfer Tube

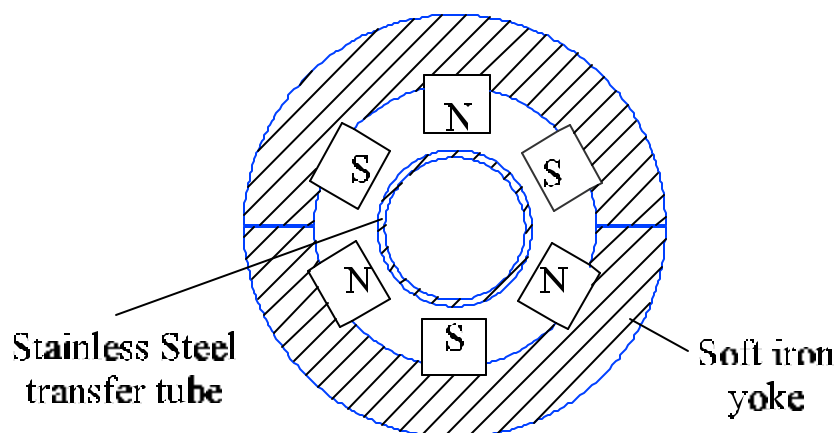


Figure 6.3: A cross sectional view of the magnetic guide is shown. Permanent magnets are arranged in a hexapole configuration. A soft iron return yoke around the outside minimizes stray fields. The inner diameter of the stainless steel transfer tube is 1.1 cm.

effect the polarization of the sample in the magnetic trap, we have designed a somewhat more sophisticated magnetic guide. The guide is machined of soft iron to minimize stray fields, especially at the ends of the transfer tube, to minimize depolarization effects of the magnetic stray field on the atoms in the magnetic moment trap. The use of extremely inexpensive permanent magnets, with a remarkably strong surface field of 2000 Gauss, provides a relatively strong guiding potential along the tube axis. A cross sectional view of the magnetic guide is shown in Figure [6.3].

6.2.3 Pushing the Atoms

The trapped atoms are pushed with a laser pulse derived from one of the trapping beams. Since the frequency of the trapping laser is shifted toward the red of the transition,

the push beam is passed through a double AOM arrangement which shifts the laser frequency back onto resonance. The AOM is also used as a fast shutter quickly turning the push beam on and off. A $\lambda/2$ wave plate is necessary to adjust the polarization with respect to the magnetic field.

The push beam is ≈ 3 mm in diameter and the intensity is ≈ 1 mW/cm² when the light hits the atoms in the MOT. Two possible transfer procedures have been investigated to move the ^{82}Rb atoms from the first MOT to the second MOT:

1. In the first scheme, the ion beam is steered onto the catcher foil and the ^{82}Rb accumulates for ≈ 3 minutes. Upon heating, the atoms are released into the first MOT and captured by the laser beams. After loading the MOT for ≈ 10 seconds, the magnetic field of the MOT is quickly turned off, the atoms are cooled using optical molasses cooling for 5 ms, after which the push beam is turned on (≈ 1 ms) and the atoms are pushed through the magnetic guide and recaptured by the second MOT. Here, the ^{82}Rb atoms are accumulated in the catcher foil rather than in the second MOT.
2. In the second method, the ion beam is steered onto the continuously heated catcher foil, atoms are continuously released and captured in the first MOT. The magnetic field of the first MOT is quickly turned off every 3 seconds, the atoms are molasses cooled and the push beam accelerates the atoms through the transfer tube into the second MOT where they are accumulated.

This second scheme seems advantageous since, in the current setup, we find only a factor of two difference in the number of trapped atoms in the pulsed and continuous mode. With a realistic repetition rate (≈ 20 loads within the 75 s half-life) and an assumed

transfer efficiency of $\gg 50\%$, which we have already demonstrated, we should be able to load $\gg 20$ million atoms into the second MOT.

6.3 Magnetic Trapping

The MOT is a simple, inexpensive, and convenient way to trap and store atoms for relatively long times. Unfortunately, it also suffers from a variety of limitations. Generally, high-precision experiments are in need of a cold, point-like, relatively dense, and polarized sample to perform the desired experiment. The presence of laser light in the MOT limits the achievable temperature, lifetime, density, and degree of polarization that can be achieved.

When trapping large numbers of atoms, the cloud becomes optically thick. As a result, a photon can scatter multiple times before it leaves the cloud. The resulting re-radiation trapping leads to a repulsive force between the atoms which limits the achievable densities to values on the order of $n_c \gg 10^{11}$ atoms/cm³. Secondly, the cooling process of the atom is based on the absorption and re-emission of photons. As a result, the temperature of the atoms in the cloud is limited by the momentum transfer of the photons. Typical temperatures achievable in MOTs are a few times the single photon recoil temperature, where the recoil temperature is

$$T_r = \frac{\hbar^2 k^2}{mk_B} :$$

More importantly, the “global” polarization of the atomic cloud that is absolutely essential for the π -asymmetry experiment can only be achieved by misaligning the laser beams giving achievable polarization of $\gg 70\%$ [54].

Finally, the lifetime of the atoms in the trap is limited by inelastic intra-trap colli-

sions. Two different collision processes occur, namely light assisted collisions and hyperfine changing collisions. The hyperfine changing collision involves two ground state atoms that collide and release one or more units of ground state hyperfine energy. For strong MOTs this process becomes unimportant since the relatively small hyperfine energy can only eject atoms out of weak traps. The second process, however, leads to the limited lifetime of the atom in a strong trap. The light assisted collision losses are rooted in the low temperature of the atoms in the MOT, where a collision time may be comparable or longer than the spontaneous emission time. As a result, the absorption and emission of photons make important contributions to the collision dynamics. Two atoms that are widely separated absorb a photon and, as a result of the strong dipole force, accelerate towards each other. Because of the low temperature of the atoms in the trap the pair of atoms have a long time to undergo spontaneous emission during this collision. After spontaneous emission, however, the atoms have a much higher kinetic energy. Thus, the atoms may be ejected from the trap if the resulting kinetic energy of the atom is larger than the trap depth [114]. This effect imposes a trade-off since both the capture velocity and the light assisted collisions increase with laser intensity.

These severe limitations of MOTs lead us to the use of magnetic traps to achieve high densities, high global polarizations, and extremely long storage times in the trap.

6.3.1 The Magnetic Trapping Principle

The Stern-Gerlach experiment in 1924 first demonstrated the mechanical action of inhomogeneous magnetic fields on neutral atoms having magnetic moments, and the basic phenomenon was subsequently developed and refined. For instance, magnetic hexapole

lenses for focussing of neutral atoms were used in the 1980s [116, 117]. The interaction of the magnetic moment μ of the atom and the inhomogeneous magnetic field produces a force which is given by

$$\mathbf{F} = \nabla (\mu \cdot \mathbf{B}) = \mu \nabla B \cos(\theta; \mathbf{B}) : \quad (6.1)$$

6.3.2 Field Geometries

W. Paul originally suggested a quadrupole trap consisting of two identical coils that carry opposite currents [51]. This trap has a single center, where the field is zero, and represents the simplest of all possible trap configurations. The trap features equal depth in the radial plane (x-y plane) and the longitudinal (z-axis) directions when the coils are separated by $\gg 1.25$ times their radius. Its simplicity and the tight confinement of the atoms in the trap makes the quadrupole trap very attractive.

The field is zero at the origin and increases in all directions as $B = A \sqrt{\frac{1}{2}r^2 + 4z^2}$ where $\frac{1}{2}r^2 = x^2 + y^2$ and the field gradient $A = \text{const.}$ The field gradient is constant along any line through the origin, but has different values in different polar directions. Thus, the force $\mathbf{F} = \mu \nabla B$ that confines the atoms is not harmonic. Such a trap has been used in the first neutral atom trapping experiments at NIST on laser cooled Na atoms with storage times of about one second as limited by background pressure [49].

Longer storage times could not be achieved, however, by simply lowering the pressure in the vacuum chamber. When reaching storage times of a few seconds, the total loss rate is no longer dominated by collisions with the hot background gas since a second term is introduced that is caused by the magnetic field geometry of the trap itself. When an atom passes through the trap center where the magnetic field is zero the force abruptly changes

sign and the atom experiences a change in the orientation of the magnetic moment relative to the local field direction. This situation allows Majorana spin-flip transitions to occur [51]. As a result of Majorana transitions, the atom no longer is in a “weak field seeking” state and is ejected from the trap.

Since this additional loss-rate can be completely avoided when designing a magnetic trap with $\mathbf{jBj} \neq 0$ at the center, a variety of new trapping configurations were developed and successfully used to confine atoms. A detailed investigation of the most popular trapping configurations, for instance the baseball trap and the Ioffe trap, can be found in Reference [51]. Recently, a new type of trap has become a celebrity due to the successful achievement of BEC in such a trap. The Time-Orbiting Potential (TOP) trap is a simple quadrupole trap which overcomes the additional loss rate due to Majorana transitions by adding an orbiting bias field that rotates the origin of the quadrupole potential in the equatorial plane at a typical rate of a few kHz. This frequency is large enough to make it impossible for the atom to follow and “see” the zero magnetic field, but much slower than the Larmor frequency which would drive the atoms out of the trap. As a result, the time-averaged potential is a non-zero field configuration which features a much tighter confinement than typical Ioffe traps [60].

6.4 The Detector Chamber

We have designed and built a detector chamber that will be used in the prototype τ -decay experiment. The chamber allows for the transfer of atoms from the first MOT into a second MOT using the technique described at the beginning of this chapter. Also, all the

necessary components for a TOP trap as well as a number of diagnostics ports are included. In addition, up to two γ -detectors can be mounted simultaneously to perform systematic checks of the detector system and to explore any acceptance perturbations caused by the rotating bias field.

The γ -decay experiment will be performed in the following manner. First, the ^{82}Rb atoms are trapped in the first MOT as described in this thesis. After accumulation in the MOT, a push beam is turned on that polarizes and efficiently transfers the atoms into the second MOT. Since the velocity of the transferred atoms is less than the capture velocity of the second MOT, the majority of the atoms are retrapped and held in the second MOT. The γ -decay measurement requires the knowledge of the nuclear spin-state of the atom, thus the atoms need to be in the $|F = 3/2; m_F = 3/2\rangle$ fully-stretched state. To achieve a high loading efficiency into any magnetic moment trap, one needs to optically pump the atoms into the stretched state prior to loading into the TOP trap. As demonstrated in the literature, a short circular-polarized laser pulse tuned to the $5S_{1/2}; F = 3/2 \rightarrow 5P_{3/2}; F^0 = 3/2$ transition, in combination with a magnetic field will pump the atoms quickly into the desired $|F = 3/2; m_F = 3/2\rangle$ state. Following the optical pumping, the magnetic quadrupole field is ramped up and the rotating bias field is turned on. The efficiency of the described loading procedure into the magnetic trap is reported to be $\gg 90\%$ [114]. Since the trapped atoms are in the stretched state, the orientation of the nuclear spin of the atom can be reconstructed at any particular instant of time, by recording the current in the bias coils as a function of time. This information will be recorded on an event-by-event basis as triggered by positron events recorded in the scintillation detector.

6.4.1 Vacuum Considerations

The 75 s half-life of ^{82}Rb determines the required storage time of the atoms in the magnetic trap. It is desirable to store the atoms within the trap as long as possible but a storage time of three times the half-life of the trapping species is sufficient. Since the storage time of the atoms in the magnetic trap scales directly with the pressure of the hot background gas, the required pressure P (in torr) in the detector chamber is given by

$$P = \frac{1}{3.3 \times 10^{16} \frac{3}{4} \bar{A}_b \bar{\tau}} ; \quad (6.2)$$

where $\bar{\tau}$ is the desired storage time in the trap and $\frac{3}{4} \bar{A}_b \gg 10^{19} \text{cm}^3 = \text{sec}$. Hence, to reach a storage time of the atoms in the trap of $\gg 250$ seconds we need to achieve a pressure in the detector chamber of $\gg 1 \times 10^{-10}$ torr.

We have chosen a pair of 20 l/s Varian StarCell ion pumps in combination with a Varian Ti-ball sublimation pump, which yields a pumping speed of $\gg 1500$ l/s (for H_2), to achieve the desired pressure in the trapping chamber. Due to the high vapor pressure of the plastic π^- -detectors, the trapping chamber needs to be separated from the “rough” vacuum of the detector chamber. A thin Ti foil (50 μm thickness) effectively separates the detector chamber from the trapping chamber without significantly hindering the π^+ -particles that reach the detector.

6.4.2 The Time-Orbiting Potential Trap

The invention of the Time-Orbiting Potential (TOP) trap was an important milestone in achieving Bose-Einstein Condensation (BEC) in a dilute gas [61]. In BEC work, it is essential to create a very tight trapping potential since one of the goals is to increase the

density of the trapped atom cloud. However, the density of the atom cloud is less important in our particular case. Nevertheless, the TOP trap has some additional features which are extremely desirable for a $\bar{\nu}$ -decay experiment. This becomes clear when analyzing the working principle of such a TOP trap (see Figure [6.4]).

The trapping potential for the neutral atoms is formed by a pair of anti-Helmholtz coils, that create a strong quadrupole potential. However, as outlined earlier, a simple quadrupole potential does not allow long storage times of the atoms in the trap, since a non-zero magnetic field at the origin is required to prevent Majorana spin-flip transitions. In addition, the bias field is needed to provide a “net” polarization of the trapped atom cloud. The TOP trap overcomes this problem by adding two pairs of bias coils that carry an oscillating current with a phase shift of $\frac{\pi}{2}$ between each pair. To understand the effect of such an oscillating field let us consider a single pair of bias coils that carries a constant current first. A constant bias field simply shifts the location of the origin of the magnetic field. As a result, the atoms react to the change in the potential and accumulate at the new field center. Nevertheless, with a second pair of bias coils and an oscillating current in such a configuration, we can rotate the minimum of the magnetic field faster than the atoms can follow. As a result, the atoms “see” a time-averaged potential that does not contain a zero field minimum.

In addition to the long storage times achievable in such a TOP trap, the rotating magnetic bias field causes the spin of the atoms to precess in the equatorial plane. Since we have optically pumped the atoms into the $jF = 3/2; m_F = 3/2$ stretched state, we also know the orientation of the nuclear spin relative to the magnetic bias field. Consequently,

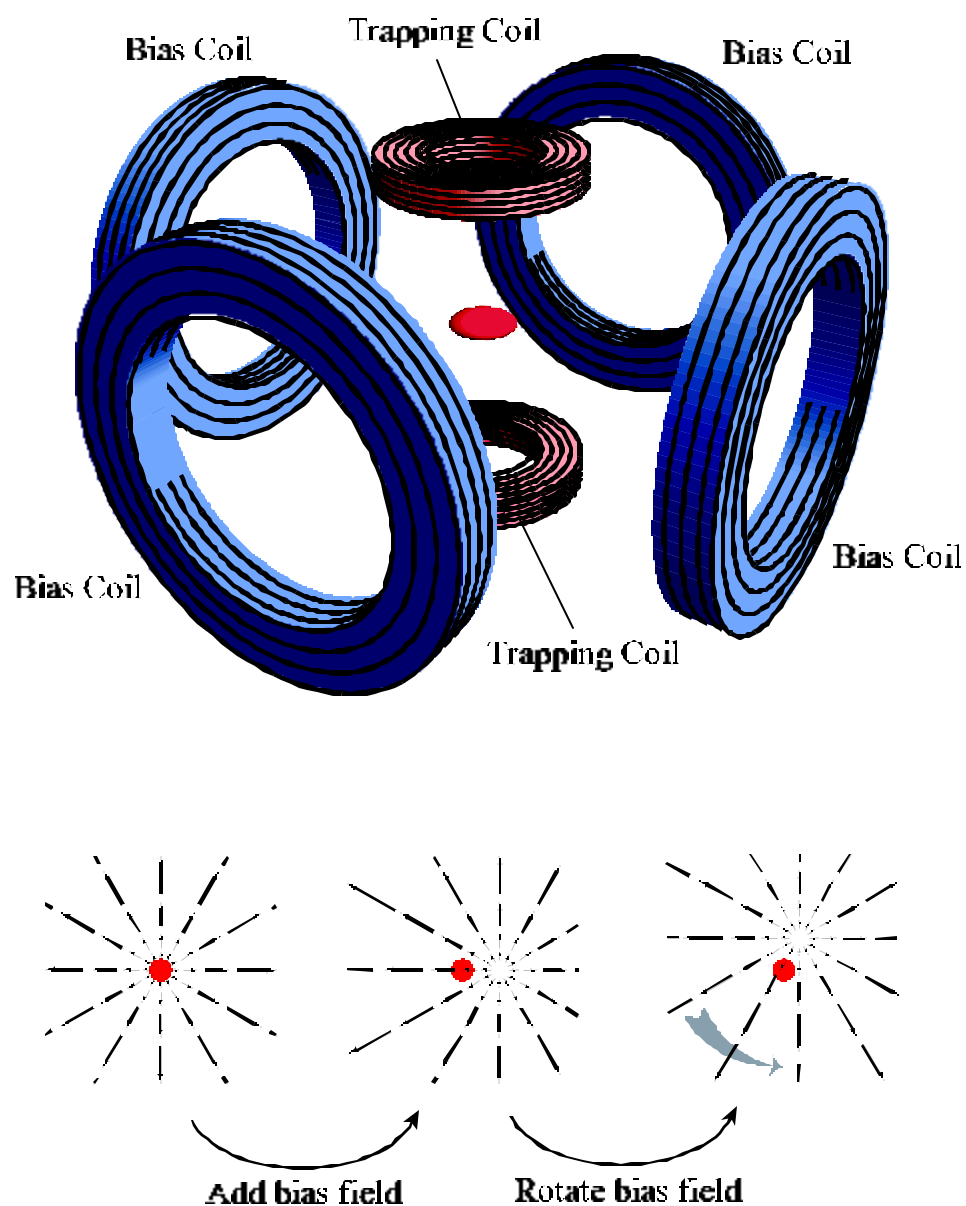


Figure 6.4: The Time-Orbiting Potential (TOP) trap. The trapping potential for the neutral atoms is formed by the pair of trapping coils (orange). In addition, two opposing pairs of bias coils (blue) create a rotating bias field. Thus, the time-averaged potential experienced by the atoms features a non-zero magnetic field at the trap minimum.

we can exploit the point-like geometry of the trapped atom cloud, and due to the continuous precession of the nuclear spin, a single γ -detector is sufficient to measure the electron-spin correlation as a continuous function of positron energy and angle relative to the nuclear spin orientation of the atoms.

Chapter 7

Summary

This thesis reports the successful trapping of 6×10^6 ^{82}Rb ($t_{1/2} = 75$ s) atoms in a Magneto-Optical Trap (MOT) with storage times of up to 90 seconds. This represents a two order of magnitude improvement over previous work. For the first time ever, the number of radioactive trapped atoms is sufficient to perform a nuclear β -decay measurement to measure the electron-spin correlation A with a precision of 1%, with the potential to improve its accuracy to the 0.1% level.

The trapping experiment uses 10 mCi of ^{82}Sr loaded into a thermal ion source of the hot cavity type. ^{82}Rb is produced following the electron-capture of the parent ^{82}Sr . Once the ^{82}Rb is produced it is efficiently vaporized and ionized in the ion source. The ^{82}Rb ions are extracted from the source, mass separated in a single-stage mass separator and implanted into a yttrium catcher foil mounted internal to the trapping cell. The trapping chamber features large laser beams (5 cm usable, 10 cm $1/e^2$ diameter) and a dry...lm coating to improve the efficiency of the magneto-optical trap. After accumulation of ^{82}Rb in the

catcher foil, the yttrium catcher foil is inductively heated to 750 °C to release the activity in the form of neutral atoms into the trapping cell. The ion implantation and subsequent heated release from the catcher foil minimizes the gas loading of the MOT and enhances the trapping efficiency.

The efficiency of the trapping experiment (from the ion source into the first MOT) is measured to be 3×10^{-4} . When breaking this down stepwise, we measure an ionization-transfer efficiency of $\gg 40\%$ onto the catcher foil, a $\gg 30\%$ release from the catcher foil and a $\gg 0.3\%$ trapping efficiency. We have demonstrated much higher trapping efficiencies with stable Cs atoms ($\gg 20\%$) in an independent setup which, in combination with the sticking time α -ray measurements performed on the dry-film coating leads to the conclusion that the dry-film coating works less than optimal. We are currently using an α -ray technique to select a better dry-film coating.

After trapping of the ^{82}Rb atoms, a laser beam tuned to the $5S_{1/2}; F = 3 \rightarrow 2$ to $5P_{3/2}; F^0 = 5 \rightarrow 2$ transition pushed the atoms into a second MOT through a 40 cm transfer tube. The atoms are efficiently retrapped in the second MOT since the capture velocity of the second MOT is larger than the average velocity of the pushed atoms. We have transferred stable ^{85}Rb atoms from the first to the second MOT with a measured efficiency of $75 \pm 15\%$ and are currently working on transferring the radioactive ^{82}Rb atoms with comparable efficiencies. The Time-Orbiting Potential (TOP) trap has been constructed and the π -detector arrangement has been tested successfully. We are thus well positioned to implement the magnetic TOP trap for a first generation π -spin correlation experiment in ^{82}Rb .

Bibliography

- [1] T. Lee and C. Yang. Question of Parity Conservation in Weak Interactions. *Phys. Review*, 104(1):254–258, 1956.
- [2] C. Wu, E. Ambler, R. W. Hayward, D. D. Hoppes, and R. P. Hudson. Experimental Test of Parity Conservation in Beta Decay. *Phys. Review*, 105:1413–1415, 1957.
- [3] L. M. Chirovsky, W. P. Lee, A. M. Sabbas, J. L. Groves, and C. S. Wu. Directional Distributions of Beta-Rays Emitted from Polarized ^{60}Co Nuclei. *Phys. Lett.*, 94, 1980.
- [4] K. Schreckenbach, P. Liaud, R. Kossakowski, H. Nastoll, A. Bussiere, and J. P. Guillaud. A New Measurement of the Beta Emission Asymmetry in the Free Decay of Polarized Neutrons. *Phys. Lett. B*, 349:427–432, 1995.
- [5] Z-T. Lu, C. J. Bowers, S. J. Freedman, B. K. Fujikawa, J. L. Mortara, S-Q. Shang, K. P. Coulter, and L. Young. Laser Trapping of Short-Lived Radioactive Isotopes. *Phys. Rev. Lett.*, 72(24):3791–3794, 1994.
- [6] M. Rowe. Recent Work with Laser Trapped Radioactive ^{21}Na Atoms. *Bull. Am. Phys. Soc.*, 42:1627–1628, 1997.

- [7] R. Guckert. Coupling an Optical Trap to a Mass Separator. Nucl. Instr. and Meth. in Phys. Res. B, 126:383–385, 1997.
- [8] R. Guckert. Magneto-Optical Trapping of Radioactive ^{82}Rb Atoms. Los Alamos National Laboratory Report LA-UR-97-4941 (submitted to Phys. Rev. Lett.), 1997.
- [9] E. L. Raab, M. Prentiss, A. Cable, S. Chu, and D. E. Pritchard. Trapping of Neutral Sodium Atoms with Radiation Pressure. Phys. Rev. Lett., 59(23):2631–2634, 1987.
- [10] J. V. Prodan, W. D. Phillips, I. So, H. Metcalf, and J. Dalibard. Stopping Atoms with Laser Light. Phys. Rev. Lett., 54(10):992–995, 1985.
- [11] W. Ertmer, R. Blatt, and J. L. Hall. Laser Manipulation of Atomic Beam Velocities: Demonstration of Stopped Atoms and Velocity Reversal. Phys. Rev. Lett., 54(10):996–999, 1985.
- [12] J. Nellesen, J. H. Müller, K. Sengstock, and W. Ertmer. Large-Angle Beam Deflection of a Laser-Cooled Sodium Beam. J. Opt. Soc. Am. B, 5(11):2149–2154, 1989.
- [13] J. Nellesen, J. Werner, and W. Ertmer. Magneto-Optical Compression of a Monoenergetic Sodium Atomic Beam. Opt. Commun., 78(3):300–308, 1990.
- [14] G. Taubes. Physicists Create New State of Matter. Science, 269:152–153, 1995.
- [15] M. H. Anderson, L. R. Ensher, M. R. Matthews, C. E. Wieman, E. A. Cornell. Observation of Bose-Einstein Condensation in a Dilute Atomic Vapor. Science, 269:198–201, 1995.

- [16] K. B. Davis, M.-O. Mewes, M. R. Andrews, N. J. van Druten, D. S. Durfee, D. M. Kurn, and W. Ketterle. Bose-Einstein Condensation in a Gas of Sodium Atoms. *Phys. Rev. Lett.*, 75(22):3969–3973, 1995.
- [17] B. P. Masterson and C. E. Wieman. Atomic Parity Non-Conservation Experiments. in: *Precision Tests of the Standard Electroweak Model* by P. Langacker, *Advanced Series on Directions in High Energy Physics*, 14:545–576, 1995.
- [18] R. D. Bolton, J. D. Bowman, E. P. Chamberlin, B. L. Fearey, H. A. Gould, H. Oona, V. D. Sandberg, M. Stephens, D. R. Swenson, W. L. Talbert, D. Tupa, D. J. Vieira, D. H. White, C. E. Wieman, and J. M. Wouters. Parity Non-Conservation Measurements of Trapped Radioactive Isotopes - A Precise Test of the Standard Model. *Research Proposal*, Los Alamos Meson Physics Facility, 1992.
- [19] G. Gwinner, J. A. Behr, S. B. Cahn, A. Ghosh, L. A. Orozco, G. D. Sprouse, and F. Xu. Magneto-Optic Trapping of Radioactive ^{79}Rb . *Phys. Rev. Lett.*, 72(24):3795–3798, 1994.
- [20] J. E. Simsarian, A. Ghosh, G. Gwinner, L. A. Orozco, G. D. Sprouse, and P. A. Voytas. Magneto-Optic Trapping of ^{210}Fr . *Phys. Rev. Lett.*, 76(19):3522–3525, 1996.
- [21] J. A. Behr et al. Magneto-Optic Trapping of β^- -Decaying $^{38}\text{K}^m$, ^{37}K from an On-Line Isotope Separator. *Phys. Rev. Lett.*, 79(3):375–378, 1996.
- [22] S. Chu, L. Hollberg, J. Bjorkholm, A. Cable, and A. Ashkin. Three-Dimensional Viscous Confinement and Colling of Atoms by Resonance Radiation Pressure. *Phys. Rev. Lett.*, 55(1):48–51, 1985.

- [23] A. Einstein. Zur Quantentheorie der Strahlung. *Phys. Z.*, pages 121–128, 1917.
- [24] R. Frisch. Experimenteller Nachweis des Einsteinschen Strahlungsrückstosses. *Z. Phys.*, 86:42–48, 1933.
- [25] R. Schieder, H. Walter, and L. Wöste. Atomic Beam Deflection by the Light of a Tunable Dye Laser. *Opt. Commun.*, 5(5):337–340, 1972.
- [26] T. W. Hänsch and A. L. Schawlow. Cooling of Gases by Laser Radiation. *Opt. Commun.*, 13(1):68–69, 1975.
- [27] J. Dalibard and W. D. Phillips. Stability and Damping of Radiation Pressure Traps. *Bull. Am. Phys. Soc.*, 30:748, 1985.
- [28] J. P. Gordon and A. Ashkin. Motion of Atoms in a Radiation Trap. *Phys. Rev. A*, 21(5):1606–1617, 1980.
- [29] R. J. Cook. Theory of Resonance-Radiation Pressure. *Phys. Rev. A*, 22(3):1078–1098, 1980.
- [30] G. V. Minogin, V. S. Letokhov, and T. V. Zueva. Hydrodynamical Equations for Atomic Motion in a Resonant Light Wave. *Opt. Commun.*, 38(3):225–229, 1981.
- [31] P. D. Lett, R. N. Watts, C. I. Westbrook, W. D. Phillips, P. L. Gould, and H. J. Metcalf. Observation of Atoms Laser Cooled below the Doppler Limit. *Phys. Rev. Lett.*, 61(2):169–172, 1988.
- [32] J. Dalibard and C. Cohen-Tannoudji. Laser Cooling below the Doppler Limit by

- Polarization Gradients: Simple Theoretical Models. *J. Opt. Soc. Am. B*, 6(11):2023–2045, 1989.
- [33] A. Aspect, E. Arimondo, R. Kaiser, N. Vansteenkiste, and C. Cohen-Tannoudji. Laser Cooling below the One-Photon Recoil Energy by Velocity-Selective Coherent Population Trapping: Theoretical Analysis. *J. Opt. Soc. Am. B*, 6(11):2112–2124, 1989.
- [34] M. Kasevich and S. Chu. Laser Cooling below a Photon Recoil with Three-Level Atoms. *Phys. Rev. Lett.*, 69(12):1741–1744, 1992.
- [35] C. Cohen-Tannoudji. New Laser Cooling Mechanisms. *Proc. Int. Sch. Phys. "Enrico Fermi"*, 118:99–169, 1992.
- [36] S. Chu. Laser Cooling and Manipulation of Atoms, and Selected Applications. *Proc. Int. Sch. Phys. "Enrico Fermi"*, 118:239–287, 1992.
- [37] W. D. Phillips. Laser Cooling and Trapping of Neutral Atoms. *Proc. Int. Sch. Phys. "Enrico Fermi"*, 118:289–343, 1992.
- [38] C. Cohen-Tannoudji: in *Les Houche, Session LIII. Fundamental Systems in Quantum Optics*. edited by J. Dalibard, J. M. Raimond, and J. Zinn-Justin (Elsevier Science Publishers B. V.), pages 1–183, 1992.
- [39] C. S. Adams, M. Sigel, and J. Mlynek. Atom Optics. *Phys. Rep.*, 240:143–210, 1994.
- [40] V. I. Balykin, V. S. Letokhov, and V. I. Mishin, and V. A. Semchishen. Laser Detection of Single Atom Fluorescence. *Sov. Phys. – JETP (Engl. Trans.)*, 26(6):357–359, 1977.

- [41] V. I. Balykin, V. S. Letokhov, and A. I. Sidorov. Radiative Collimation of an Atomic Beam by Two-Dimensional Cooling by a Laser Beam. *Sov. Phys. – JETP (Engl. Trans.)*, 40(6):1026–1029, 1984.
- [42] S. V. Andreev, V. L. Balykin, V. S. Letokhov, and V. G. Minogin. Radiative Slowing and Reduction of the Energy Spread of a Beam of Sodium Atoms to 1.5 K in an Oppositely Directed Laser Beam. *Sov. Phys. – JETP (Engl. Trans.)*, 34(8):442–445, 1982.
- [43] B. Sheehy, S.-Q. Shang, R. Watts, S. Hatamian, and H. Metcalf. Diode-Laser Deceleration and Collimation of a Rubidium Beam. *J. Opt. Soc. Am. B*, 6(11):2165–2170, 1989.
- [44] B. Sheehy, S.-Q. Shang, P. van der Straten, and H. Metcalf. Collimation of a Rubidium Beam Below the Doppler Limit. *Chem. Phys.*, 145:317–325, 1990.
- [45] C. Monroe, W. Swann, H. Robinson, and C. Wieman. Very Cold Trapped Atoms in a Vapor Cell. *Phys. Rev. Lett.*, 65(13):1571–1574, 1990.
- [46] W. Paul, H. O. Osberghaus, and E. Fisher. *Forschungsber. Wirtsch. - Verkehrsminist. Nordrhein-Westfalen*, 1958.
- [47] K.-J. Kügler, W. Paul, and U. Trinks. A Magnetic Storage Ring for Neutrons. *Phys. Lett.*, 72B(3):422–424, 1978.
- [48] C. V. Heer. Feasibility of Containment of Quantum Magnetic Dipoles. *Rev. Sci. Instr.*, 34(5):532–537, 1963.

- [49] A. Migdall, J. Prodan, W. E. Phillips, T. Bergeman, and H. Metcalf. First Observation of Magnetically Trapped Neutral Atoms. *Phys. Rev. Lett.*, 54(24):2596–2599, 1985.
- [50] E. A. Cornell, C. R. Monroe, and C. E. Wieman. Multiply Loaded, ac Magnetic Trap for Neutral Atoms. *Phys. Rev. Lett.*, 67(18):2439–2442, 1991.
- [51] T. Bergeman, G. Erez, and H. J. Metcalf. Magnetostatic Trapping Fields for Neutral Atoms. *Phys. Rev. A*, 35(4):1535–1546, 1987.
- [52] H. Metcalf and P. van der Straten. Cooling and Trapping of Neutral Atoms. *Physics Reports*, 244:203–286, 1994.
- [53] D. E. Pritchard, E. L. Raab, V. S. Bagnato, C. E. Wieman, and R. N. Watts. Light Traps Using Spontaneous Forces. *Phys. Rev. Lett.*, 57(3):310–313, 1986.
- [54] P. Feng and T. Walker. Spin-Polarized Optical Atom Traps. *Bull. Am. Phys. Soc.*, 41(3):1111, 1996.
- [55] T. Walker, D. SESCO, and C. Wieman. Collective Behavior of Optically Trapped Neutral Atoms. *Phys. Rev. Lett.*, 64(4):408–411, 1990.
- [56] C. D. Wallace, T. P. Dinneen, K. Y. N. Tan, A. Kumarakrishnan, P. L. Gould, and J. Javanainen. Measurements of Temperature and Spring Constant in a Magneto-Optical Trap. *J. Opt. Soc. Am. B*, 11(5):703–711, 1994.
- [57] W. Petrich, M. H. Anderson, J. R. Ensher, and E. A. Cornell. Behavior of Atoms in a Compressed Magneto-Optical Trap. *J. Opt. Soc. Am. B*, 11(8):1332–1335, 1994.
- [58] A. Einstein. *Sitzungsber. Kgl. Preuss. Akad. Wiss.*, page 261, 1924.

- [59] S. N. Bose. Plancks Gesetz und Lichtquantenhypothese. *Z. Phys.*, 26:178–181, 1924.
- [60] W. Petrich, M. H. Anderson, J. R. Ensher, and E. A. Cornell. Stable, Tightly Confining Magnetic Trap for Evaporative Cooling of Neutral Atoms. *Phys. Rev. Lett.*, 74(17):3352–3355, 1995.
- [61] E. A. Cornell. Very Cold Indeed: The Nanokelvin Physics of Bose-Einstein Condensation. *J. Res. Natl. Inst. Stand. Technol.*, 101:419–434, 1996.
- [62] F. Halzen and A. D. Martin. *Quarks and Leptons: An Intruductory Course in Modern Particle Physics*. John Wiley & Sons, Inc., 1984.
- [63] S. A. Blundell, W. R. Johnson, and J. Sapirstein. The Theory of Atomic Parity Violation. in: *Precision Tests of the Standard Electroweak Model* by P. Langacker, *Advanced Series on Directions in High Energy Physics*, 14:577–598, 1995.
- [64] E. N. Fortson and L. L. Lewis. Atomic Parity Non-Conservation Experiments. *Physics Reports (Review section of Physics Letters)*, 113(5):289–344, 1984.
- [65] C. E. Tanner and E. D. Commins. Measurement of Stark Amplitudes σ^{\pm} in the $6^2P_{1=2} \rightarrow 7^2P_{1=2}$ Transition in Atomic Thallium. *Phys. Rev. Lett.*, 56(4):332–335, 1986.
- [66] S. L. Gilbert. *Parity Violation in Atomic Cesium and Associated Experiments*. PhD thesis, University of Michigan, 1986.
- [67] M. C. Noecker, B. P. Masterson, and C. E. Wieman. Precision Measurement of Parity

- Nonconservation in Atomic Cesium: A Low-Energy Test of the Electroweak Theory. *Phys. Rev. Lett.*, 61(3):310–313, 1988.
- [68] C. S. Wood. High Precision Atomic Parity Non-Conservation Measurement using a Spin-Polarized Cesium Beam and the Nuclear Anapole Moment of ^{133}Cs . PhD thesis, University of Colorado, 1996.
- [69] Richard. B. Firestone. *Table of Isotopes*. John Wiley and Sons, Inc., 8th edition, 1996.
- [70] J. Deutsch and P. Quin. Symmetry-Tests in Semileptonic Weak Interactions: A Search for New Physics. in: *Precision Tests of the Standard Electroweak Model* by P. Langacker, *Advanced Series on Directions in High Energy Physics*, 14:706–765, 1995.
- [71] M. N. Saha. Ionization in the Solar Chromosphere. *Phil. Mag.*, 40:472–488, 1920.
- [72] I. Langmuir and K. H. Kingdon. *Proc. Roy. Soc. London*, 107:61, 1925.
- [73] P. G. Johnson, A. Bolson, and C. M. Henderson. A High Temperature Ion Source for Isotope Separators. *Nucl. Instr. and Meth.*, 106:83–87, 1973.
- [74] G. J. Beyer, E. Herrmann, A. Piotrowski, V. J. Raiko, and H. Tyrro α . A New Method for Rare-Earth Isotope Separation. *Nucl. Instr. and Meth.*, 96:437–439, 1971.
- [75] A. Latuszynski and V. I. Raiko. Studies of the Ion Source with Surface-Volume Ionization. *Nucl. Instr. and Meth.*, 125:61–66, 1975.
- [76] R. Kirchner and A. Piotrowski. Thermal Ionization in a Hot Cavity. *Nucl. Instr. and Meth.*, 153:291–292, 1978.

- [77] I. Amarel, R. Bernas, J. Chaumont, R. Foucher, J. Jastrezbski, A. Johnson, R. Klapisch, and J. Teillac. On-Line Mass-Spectrometric Method for the Study of Short-Lived Rb, Cs, and Na Isotopes. *Ark. Fys.*, 36(10):77–89, 1967.
- [78] L. C. Carraz, S. Sundell, H. L. Ravn, M. Skarestad, and L. Westgaard. High-Temperature Carbide Targets for Fast On-Line Mass Separation of Alkali and Noble Gas Elements. *Nucl. Instr. and Meth.*, 158:69–80, 1979.
- [79] B. Vosicki, T. Björnstad, L. C. Carraz, J. Heinemeier, and H. L. Ravn. Intense Beams of Radioactive Halogens Produced by Means of Surface. *Nucl. Inst. and Meth.*, 186:307–313, 1981.
- [80] M. Shmid, G. Engler, I. Yoresh, and E. Skurnik. A Negative Surface Ionization Integrated Target-Ion Source for an On-Line Isotope Separator. *Nucl. Inst. and Meth.*, 186:349–351, 1981.
- [81] V. Rabbel, U. Stroehlker, J. Muenzel, H. Wollnik, F. Bloennigen, K. Kobras, and W. Lippert. A Negative Surface-Ionization Ion Source for the On-Line Mass Separator OSTIS. *Nucl. Instr. and Meth. in Phys. Res. B*, 26:246–248, 1987.
- [82] K. D. Wunsch. An On-Line Mass-Separator for Thermically Ionisable Fission Products: OSTIS. *Nucl. Instr. and Meth.*, 155:347–351, 1978.
- [83] G. Rudstam. The On-Line Mass-Separator OSIRIS and the Study of Short-Lived Fission Products. *Nucl. Instr. and Meth.*, 139:239–249, 1976.
- [84] L. von Reisky, J. Bonn, S. L. Kaufman, L. Kugler, E.-W. Otten, J.-M. Rodriguez-

- Giles, K. P. C. Spath, and D. Weskott. An On-Line Mass Separator for Fission-Produced Alkali Isotopes. *Nucl. Instr. and Meth.*, 172:423–430, 1980.
- [85] A. Piotrowski, R. L. Gill, D. C. McDonald. A New High-Temperature Plasma Ion Source for the TRISTAN ISOL Facility. *Nucl. Instr. and Meth. in Phys. Res. B*, 26:249–252, 1987.
- [86] R. Kirchner. Progress in Ion Source Development for On-Line Separators. *Nucl. Instr. and Meth.*, 186:275–293, 1981.
- [87] V. P. Afanas'ev, V. A. Obukhov, and V. I. Raiko. Thermoionization Efficiency in the Ion Source Cavity. *Nucl. Instr. and Meth.*, 145:533–536, 1977.
- [88] R. Kirchner. On the Thermoinization in Hot Cavities. *Nucl. Instr. and Meth.*, (292):203–208, 1990.
- [89] R. Kirchner. Ion Sources for Radioactive Beams and Related Problems. *Rev. Sci. Instrum.*, 67(3):928–933, 1996.
- [90] David R. Lide. *Handbook of Chemistry and Physics*. CRC Press, Inc., 77th edition, 1995.
- [91] W. R. Smythe, L. H. Rumbaugh, and S. S. West. A High Intensity Mass-Separator. *Phys. Review*, 45:724–727, 1934.
- [92] L. P. Smith, W. E. Parkins, and A. T. Forrester. On the Separation of Isotopes in Quantity by Electrostatic Means. *Phys. Review*, 72:989–, 1947.

- [93] S. Taya, K. Tokiguchi, I. Kanomata, and H. Matsuda. A Triple Focusing Mass Separator. Nucl. Instr. and Meth., 150:165–171, 1978.
- [94] H. Wollnik and K. Becker. Ion Optical Design for an On-Line Mass Separator with Low Cross Contamination and the Capability of Good Mass Resolution. Nucl. Instr. and Meth. in Phys. Res. A, 238:206–214, 1985.
- [95] S. B. Karmohapatro. A Simple Mass Separator for Radioactive Isotopes. Nucl. Instr. and Meth. in Phys. Res. B, 26:34–36, 1987.
- [96] W. L. Talbert Jr., H. Wollnik, and C. Geisse. Ion-Optical Design for an On-Line Mass Separator at LAMPF. Nucl. Instr. and Meth. in Phys. Res. B, 26:351–353, 1987.
- [97] C. Geisse, H. Wollnik, B. Allardyce, E. Kugler, and K. Schloesser. The Optics of ISOLDE 3 - The New On-Line Mass Separator at CERN. Nucl. Instr. and Meth. in Phys. Res. B, 26:120–124, 1987.
- [98] H. Wollnik. Mass Separators. Nucl. Instr. and Meth. in Phys. Res. A, 258:289–296, 1987.
- [99] S. J. Balestrini. The Optics of Mass Separator I. Technical report, Los Alamos National Laboratory, LA-8893-MS, 1981.
- [100] H. Wollnik, J. Brezina, M. Berz, and W. Wendel. GIOS-BEAMTRACE, a Program for the Design of High Resolution Mass Spectrometers. Proc. AMCO-7, GSI-Report, Vol. THD-26, pages 679–683, 1984.
- [101] W. Weibler, T. Schneider, R. Wallenstein, D. Dubbers, K. Wandelt, A. Hanser, and C.

Ekström. The Clean Deposition of Radioactive Isotopes on a Single Crystal Surface. Nucl. Instr. and Meth., 206:299–301, 1983.

- [102] Bernhard Wolf. Handbook of Ion Sources. CRC Press, Inc., 1995.
- [103] M. Stephens and C. Wieman. High Collection Efficiency in a Laser Trap. Phys. Rev. Lett., 72(24):3787–3790, 1994.
- [104] M. Stephens, R. Rhodes, and C. Wieman. Study of Wall Coatings for Vapor-Cell Laser Traps. J. Appl. Phys., 76(6):3479–3488, 1994.
- [105] K. Lindquist, M. Stephens, and C. Wieman. Experimental and Theoretical Study of the Vapor-Cell Zeeman Optical Trap. Phys. Rev. A, 46(7):4082–4090, 1992.
- [106] K. B. MacAdam, A. Steinbach, and C. E. Wieman. A Narrow-Band Tunable Diode Laser System with Grating Feedback, and a Saturated Absorption Spectrometer for Cs and Rb. Am. J. Phys., 60(12):1098–1110, 1992.
- [107] K. E. Gibble, S. Kasapi, and S. Chu. Improved Magneto-Optical Trapping in a Vapor Cell. Opt. Lett., 17(7):526–528, 1992.
- [108] J. L. Hall, L. Hollberg, T. Baer, and H. G. Robinson. Optical Heterodyne Saturated Spectroscopy. Appl. Phys. Lett., 39(9):680–682, 1981.
- [109] F. Riehle, A. Witte, T. Kisters, and L. Helmcke. Interferometry with Ca Atoms. Appl. Phys. Part B, pages 333–340, 1992.
- [110] K. Sengstock, U. Sterr, G. Hennig, D. Bettermann, J. H. Müller, and W. Ertmer. Op-

- tical Ramsey Interferences on Laser Cooled and Trapped Atoms, Detected by Electron Shelving. *Opt. Commun.*, 103:73–78, 1993.
- [111] W. Z. Zhao, J. E. Simsarian, L. A. Orozco, W. Shi, and G. D. Sprouse. Measurement of the $7p^2P_{3=2}$ Level Lifetime in Atomic Francium. *Phys. Rev. Lett.*, 78(22):4169–4172, 1997.
- [112] C. Thibault et al. Hyperfine Structure and Isotope Shift of the D_2 Line of $^{76i} 98Rb$ and some of their Isomers. *Phys. Rev. C*, 23(6):2720–2729, 1981.
- [113] J. A. Fedchak, P. Cabauy, W. J. Cummings, C. E. Jones, and R. S. Kowalczyk. Silane Coatings for Laser-Driven Polarized Hydrogen Sources and Targets. Technical report, Argonne National Laboratory, PHY-8403-ME-96, 1996.
- [114] C. J. Myatt. Bose-Einstein Condensation Experiments in a Dilute Vapor of Rubidium. PhD thesis, University of Colorado, 1997.
- [115] C. J. Myatt, N. R. Newbury, R. W. Ghrist, S. Loutzenhiser, and C. E. Wieman. Multiply Loaded Magneto-Optical Trap. *Opt. Lett.*, 21(4):290–292, 1996.
- [116] H. Friedburg and W. Paul. Optische Abbildung mit Neutralen Atomen. *Naturwiss.*, 38:159–160, 1951.
- [117] H. Friedburg. Optische Abbildung mit Neutralen Atomen. *Z. Phys.*, 130:493–512, 1951.
- [118] K.-J. Kügler, K. Mortiz, W. Paul, U. Trinks. NESTOR - A Magnetic Storage Ring for Slow Neutrons. *Nucl. Instr. and Meth. in Phys. Res. B*, 228:240–258, 1985.

- [119] R. Kirchner and E. Roeckl. Investigation of Gaseous Discharge Ion Sources for Isotope Separation On-Line. Nucl. Instr. and Meth., 133:187–204, 1976.

Appendix A

Symbols

In Chapter 3, a number of symbols and constants are used to express the ionization efficiency of a hot surface and a hot cavity ionizer, respectively. The following list (and the theoretical part of Chapter 3) is aimed to guide the reader, but can not serve as a substitute for more detailed publications related to the topic. For the interested reader, I would like to recommend the following review paper and the references found therein [119].

A_0	Richardson's constant ($= 4\pi mek^2/h^3 = 120.4 \text{ A/K}^2 \text{ cm}^2$).
α_i	Ionization degree n_i/n_0 and ionization efficiency $n_i/(n_i + n_0)$, respectively, for surface ionization.
α	Ionization efficiency $n_i/(n_i + n_0)$ of thermal equilibrium plasma (Saha-equation).
e	Electron charge ($= 1.60 \times 10^{-19} \text{ A s}$).
g_0, g_i	Statistical weight of atomic or ionic ground state ($= 2J_{0,i} + 1$, where $J_{0,i}$ is the total angular momentum of the atomic or ionic electron shell).
h	Planck's constant ($= 4.14 \times 10^{-15} \text{ eV s}$).
j_0, j_i	Current density of atoms or ions at the emission orifice of the ionizer.
j_{e0}	Thermionic electron current density [$= A_0 T^2 \exp(-e/kT)$].
k	Boltzmann's constant ($= 8.62 \times 10^{-5} \text{ eV/K}$ $= 1.38 \times 10^{-19} \text{ mbar cm}^3/\text{K}$).
\bar{z}	Mean number of collisions of atoms with the walls of the cavity.
λ_D	Debye-length [$= (kT_e/4\pi n_e e^2)^{1/2}$].
m	Electron mass ($= 9.11 \times 10^{-28} \text{ g}$).
n_0, n_i, n_e	Density of atoms, ions or electrons, respectively. Additional subscript 0 refers to the density at the wall of the cavity, subscript p to the density inside the plasma.
P	Plasma pressure [$= kT (n_0 + n_i + n_e)$].

Appendix B

Ion Optical Calculations

The ion optics of the mass separator is calculated with GIOS, a software package developed to simulate complex ion optical systems [100]. GIOS uses the method of transfer matrices to perform its calculations and features precise predictions of the characteristics of the simulated ion beam. We found good agreement with the predicted values of the quadrupole and magnetic dipole settings when optimizing the transmission of the mass separator experimentally.

The GIOS input file is shown which illustrates the simplicity of the single stage mass separator. We calculate the ion optics up to third order to recognize aberrations. A typical run calls for a minimization of the sum of the matrix elements $\sum_{h,i} (X; A) + \frac{(X; AAA)}{5000}$ which maximizes the transmission through the separator.

```

\onecolumn
MS-1 Separator at Los Alamos
; Date 03/28/97
R P 0.02 85 1 ;
PHASE_SPACE X .0005 .005 ;
PHASE_SPACE Y .0005 .005 ;
C O 3 3 ;
D P 1.5E-03 0 ;
FIT SIMPLEX ;
; *** Define Variables for
; Quad I and Quad II **;
A = -1.7612500E-01 ;
B = 3.66098800E-01 ;
E = -2.625823627E-01 ;
G = -3.9812500E-01 ;
H = 7.803120711E-01 ;
I = -4.553766823E-01 ;
;
; ***** Entrance Slit *****
;
; L = (X,A) + (X,AAA) * 0.0002 ;
; F A L 0 9999999 ;
; F (X,AAA) 0 9999999 ;
; F (X,X) -1 9999999 ;
; F E Y 2E-3 9999999 ;
; P Q .1 .3 .5 .7 .9 ;
; P P (X,Y) 20000 1E-3 10E-3 ;
; P Q .1 .3 .5 .7 .9 ;
; P P (X,A) 20000 1E-3 5E-2 ;
; P Q .1 .3 .5 .7 .9 ;
; P P (X,Y) 20000 1E-3 10E-3 ;
; P Q .1 .3 .5 .7 .9 ;
; P P (X,A) 20000 1E-3 5E-2 ;
; P Q .1 .3 .5 .7 .9 ;
; P P (Y,B) 20000 10E-3 7E-3 ;
; P Q .1 .3 .5 .7 .9 ;
; P P (X,Y) 5000 20E-3 20E-3 ;
;
; ***** Definition of Magnetic Dipol
BLOCK UNIT EINS ;
S = 0 ;
T = 0 ;
F F 1 =S ;
M S 1.606 45 .05 ;
F F 1 =S =T ;
BLOCK END ;
; ***** Magnet *****
C B ;
I B EINS ;
;
; M = (Y,B) + (Y,BBB) * 0.0001 ;
; F A M 0 9999999 ;
; F (Y,B) 0 9999999 ;
D L .0254 ;
F F 1 ;
E Q .153 =B .030 ;
F F 1 ;
D L .0254 ;
F F 1 ;
E Q .153 =E .030 ;
F F 1 ;
; E M 0.12 0 0 1.0V 0.030 ;
D L 0.356 ;
; *****
; L = (X,A) + (X,AAA) * 0.0002 ;
; F A L 0 9999999 ;
; F (X,AAA) 0 9999999 ;
; F (X,X) -1 9999999 ;
; F E Y 2E-3 9999999 ;
; P Q .1 .3 .5 .7 .9 ;
; P P (X,Y) 20000 1E-3 10E-3 ;
; P Q .1 .3 .5 .7 .9 ;
; P P (X,A) 20000 1E-3 5E-2 ;
; P Q .1 .3 .5 .7 .9 ;
; P P (X,Y) 20000 1E-3 10E-3 ;
; P Q .1 .3 .5 .7 .9 ;
; P P (X,A) 20000 1E-3 5E-2 ;
; P Q .1 .3 .5 .7 .9 ;
; P P (Y,B) 20000 10E-3 7E-3 ;
; P Q .1 .3 .5 .7 .9 ;
; P P (X,Y) 5000 20E-3 20E-3 ;
;
; ***** Definition of Magnetic Dipol
BLOCK UNIT EINS ;
S = 0 ;
T = 0 ;
F F 1 =S ;
M S 1.606 45 .05 ;
F F 1 =S =T ;
BLOCK END ;
; ***** Magnet *****
C B ;
I B EINS ;
;
; M = (Y,B) + (Y,BBB) * 0.0001 ;
; F A M 0 9999999 ;
; F (Y,B) 0 9999999 ;

```

```

; F (Y, Y) -6 9999999 ;
; F E Y 2E-3 9999999 ;
; P M ;
; P N ;
;
I B -EINS ;
C B ;
; F (Y, B) 0 9999999 ;
D L 1.73 ;
; ***** Exit Slit *****
P M ;
; P N ;
; L = (X, A) + (X, AAA) * 0.0015 ;
; F A L 0 9999999 ;
F (X, A) 0.0 99999999 ;
F E Y 2E-3 9999999 ;
; F (X, BB) 2E-1 99999999 ;
; F (X, XXX) 0 99999999 ;
; F (Y, B) 0.0 99999999 ;
; P Q .1 .3 .5 .7 .9 ;
; P P (X, Y) 20000 5E-3 5E-3 ;
; P Q .1 .3 .5 .7 .9 ;
; P P (X, Y) 20000 5E-3 5E-3 3 ;
; P Q .1 .3 .5 .7 .9 ;
; P P (X, A) 10000 1E-3 50E-3 ;
A S S 1 1 ;
; P Q .1 .3 .5 .7 .9 ;
; P P (X, Y) 20000 5E-3 5E-3 ;
;
; ***** Second Quadtriplet *
D L 0.4064 ;
F F 1 ;
E Q .153 =G .030 ;
F F 1 ;
D L .0254 ;
F F 1 ;
E Q .153 =H .030 ;
F F 1 ;
D L .0254 ;
F F 1 ;
E Q .153 =I .030 ;
F F 1 ;
D L 0.4064 ;
; ***** Catcher Foi I *****
; P M ;
; P N ;
; L = (X, A) + (X, AAA) * 0.00015 ;
; F A L 0 9999999 ;
; F E X 2E-03 9999999 ;
; F E Y 2E-03 9999999 ;
; F (X, A) 0.0 99999999 ;
; F (X, BB) 2E-1 99999999 ;
; F (X, AAA) 30 99999999 ;
; F (Y, B) 0.0 99999999 ;
; P Q .1 .3 .5 .7 .9 ;
; P P (X, Y) 20000 5E-3 5E-3 ;
; P Q .1 .3 .5 .7 .9 ;
; P P (X, Y) 20000 5E-3 5E-3 ;
; P Q .1 .3 .5 .7 .9 ;
; P P (X, A) 10000 1E-3 50E-3 ;
A S S 4E-3 1 ;
P B 50 .03 .03 2. 2 .5 2 5 1 1 5 5 ;
END ;
END

```

Appendix C

Foil Heating

The following simple model relates the resistance of the catcher foil to the maximal temperature achievable for a given foil material.

Starting from basic principles, in this case Faraday's law of induction, we can express the induced electromotive force E ,

$$\begin{aligned} E &= i \frac{d}{dt} \odot_m ; \\ &= i \frac{\pm B}{\pm t} \frac{1}{2} r^2 \end{aligned}$$

where r is the foil thickness. Now consider the differential current due to E

$$\begin{aligned} dl &= \frac{E}{\text{Resistance}} ; \\ &= i \frac{\frac{\pm B}{\pm t} \frac{1}{2} r^2}{\frac{1}{2} \frac{2\pi r}{t} dr} ; \\ &= i \frac{\pm B}{\pm t} \frac{rt}{2\pi} dr \end{aligned}$$

The differential induced power

$$dP = E dl ;$$

$$= \frac{\mu_{\pm B}}{\pm t} \pi_2 \frac{1}{2} r^3 t dr :$$

The total instantaneous induced power on the foil is

$$\begin{aligned} P &= \int_0^R dP dr ; \\ &= \frac{\mu_{\pm B}^0}{\pm t} \pi_2 \frac{R^4}{8} t : \end{aligned}$$

Average over a sinusoidal excitation the average power is

$$\langle P \rangle = P_{ind} = \frac{\omega^2 B_0^2 t R^4}{16} ;$$

where ω is the drive frequency, B_0 is the B field amplitude inside of the solenoid, and $\frac{1}{2}$ is the foil resistivity.

Now assume that this thermal energy is distributed evenly throughout the foil, so that we achieve an equilibrium temperature. We can calculate this temperature if

$$\begin{aligned} P_{ind} &= P_{radiated} ; \\ \frac{\omega^2 B_0^2 t R^4}{16} &= T^4 \frac{1}{2} R^2 ; \\ \Rightarrow T^4 &= \frac{\omega^2 B_0^2 t R^2}{64} : \end{aligned} \quad (C.1)$$

Equation (C.1) can be used to compare the different foil materials and estimate the achievable temperatures at a given RF power setting. The following example illustrates the good agreement of recorded heating data and predictions made by the model. We find the following resistivity data for yttrium and platinum:

$$\rho_{Pt} = 10.42 \times 10^{-8} \text{ } \Omega \cdot \text{cm} ;$$

$$\rho_Y = 58.5 \times 10^{-8} \text{ } \Omega \cdot \text{cm} ;$$

Therefore, we expect that at the same conditions (same foil thickness, applied RF power, foil size, and drive frequency) the temperature of the yttrium foil would be lower by a factor of $\sqrt{\frac{P_{Pt}}{P_Y}} = 1:54$. This gives us a theoretical temperature for the yttrium foil of

$$T_Y = \frac{T_{Pt}}{\sqrt{\frac{P_{Pt}}{P_Y}}} = \frac{1350\text{ }^{\circ}\text{C}}{1:54} = 876\text{ }^{\circ}\text{C} :$$

Experimentally, we obtained a temperature ($V_{pp} = 1:06\text{ V}$; $P_{\text{reflected}} = 18\%$) of

$$T_Y = 822\text{ }^{\circ}\text{C} :$$

This temperature agrees well with the predicted data. The small discrepancy can easily be explained by the uncertainties in

- ² the temperature measurement with the optical pyrometer (the yttrium foil is not uniformly heated);
- ² the losses in the heating circuit (we measure a slight change in the reflected power).

We estimate that these experimental uncertainties lead to a total uncertainty of $\pm 10\%$ in the measured foil temperatures.